TESTING AND DEVELOPMENT OF A SOLAR-DISH CAVITY RECEIVER FOR THE MELTING OF ZINC METAL

by

P.J.A. Bezuidenhout

Supervisor: Prof W.G. le Roux

Submitted in partial fulfilment of the requirements for the degree:

Master of Engineering (Mechanical Engineering)

in the

Department of Mechanical and Aeronautical Engineering

Faculty of Engineering, Built Environment and Information Technology

UNIVERSITY OF PRETORIA

SOUTH AFRICA

2024

UNIVERSITEIT VAN PRETORIA
UNIVERSITY OF PRETORIA
YUNIBESITHI YA PRETORIA
Denkleiers • Leading Minds • Dikgopolo tša Dihlalefi

EXECUTIVE SUMMARY

Title: Testing and development of a solar-dish cavity receiver for the melting of zinc metal

Author: P.J.A. Bezuidenhout

Supervisor: Prof W.G. le Roux

Department: Mechanical and Aeronautical Engineering

University: University of Pretoria

Degree: Master of Engineering, MEng (Mechanical Engineering)

Concentrated solar power (CSP) technologies have been shown to reach temperatures well in excess of what is required for most high-temperature industrial heat applications. South Africa's solar resource can be used to address the carbon footprint of industrial heat applications and to improve the value cycle of local mineral resources. Zinc has been identified as one of the underutilised mineral resources, especially since South Africa has one of the largest zinc reserves; however, at the time of writing, no local beneficiation took place as all zinc ore was being exported. The material properties of zinc made it a suitable starting point for demonstrating the melting of metals with a low melting point using CSP as the heat source. One of the most common methods of producing zinc is the hydro-metallurgical or Roast-Leach-Electrowin (RLE) process, producing about 80% of the world's zinc. The last step of this process, the remelting of the zinc metal cathodes, has been identified as a suitable starting point for demonstrating the concept of applying CSP as an alternative heat source to a high-temperature industrial application. To demonstrate this concept, the practical considerations for the melting of zinc metal, using CSP, needed to be investigated.

In this study, an experimental and analytical analysis of a rotating cylindrical cavity receiver for the indirect melting of zinc metal, using CSP, is presented. The experimental setup was constructed around a multi-facet parabolic dish with an incident area of 2.85 m^2, located on the roof of Engineering Building 2 at the University of Pretoria. This parabolic dish was developed as part of a previous study aimed at demonstrating cost-effective parabolic dish designs with good optical properties. In combination with the parabolic dish, a novel cylindrical cavity receiver for the indirect melting of zinc metal was evaluated. This receiver had the capacity to house 17 kg of

zinc metal, in the unprocessed form, and had an aperture diameter of 0.2 m. The receiver was also fitted to a drive system to be rotated between 20 and 42 rpm to improve mixing and heat transfer in the zinc feedstock. Five experimental test runs were executed, of which four demonstrated the concept of melting zinc using only CSP, such that molten zinc could be tapped from the receiver. During the experimental tests, up to 73.5% of the molten inventory could be tapped from the receiver in the molten state, and average thermal efficiencies of up to 42% were achieved.

In support of the experimental work, a predictive analytical model was developed in the Python coding language to be used for the evaluation of the experimental work and for further development of this field of study. The experimental results were used to validate the predictive model as well as to experimentally determine a heat transfer efficiency factor. The heat transfer efficiency factor accounted for the voids in the zinc feedstock, which impaired heat transfer in the system. It was determined that a heat transfer factor of 0.6 was required for new receivers and that a factor of 0.8 could be used for a receiver that had a layer of solidified process material in the zinc cavity. The analytical model made use of historical weather data to predict the temperature of zinc in the cavity receiver with an average accuracy of 2.7%. The predictive model showed that it would be possible to process 41 kg of zinc, using the small-scale solar experimental setup, on a day with a peak direct normal irradiance (DNI) of 900 W/m^2 and wind speeds of below 2 m/s. This demonstrates that 14.4 kg of zinc can be processed in a typical day for each m² of parabolic dish reflector area.

The predictive model has the potential to serve as a robust tool for the further development of this technology application. Even though this study has proven that it is possible to melt zinc metal using CSP, the predictive model highlighted that there are still shortcomings in the body of knowledge related to this field of study. The heat loss mechanisms from cavity receivers in various environmental conditions need further development to allow for more accurate theoretical estimations. The heat transfer in a packed bed of feedstock requires further investigation to address the required heat transfer efficiency factor used in this work. This study has shown that it is possible to melt zinc metal using a cavity receiver and that this molten material can be tapped from the receiver and cast into ingots, demonstrating the use of the technology for batch-driven casting, recycling, and galvanisation applications. This work lays a foundation for future batch smelting applications relying on CSP as the heat source and has the potential to reduce the carbon footprint of some high-temperature industrial heat applications.

ACKNOWLEDGEMENTS

I would like to give thanks and extend my gratitude to the following people who supported me in this work and throughout my postgraduate studies:

- Prof Willem G. le Roux for his continued support and guidance throughout the study. Thank you for your endless patience and broad knowledge of this field of study that guided me to an in-depth understanding of my subject matter.
- Dr Joalet D. Steenkamp for her tireless support and guidance throughout the study. Thank you for the advice, guidance, emotional support, and endless enthusiasm throughout the process.
- Dr Quinn G. Reynolds for his guidance and assistance in developing the computational model for this study. Thank you for your patience and for taking the time to explain and teach me the fundamentals of coding, and thank you for the excellent friend you are to me.
- Dr Lina Hockaday for introducing me to this field of study and for the groundwork she has done to make this field of study a reality.
- Mr Jonathan Swanepoel, Mr Casey Roosendaal, and Mr Westley Roosendaal for their amazing support and contribution to this research. Thank you for always being willing to help and for the excellent work you have done in the past which has helped to make this study a reality.

I would also like to thank:

- Mintek and Tenova Pyromet for the financial support needed during this study;
- The University of Pretoria, together with the staff and previous postgraduate students that aided in the development of the multi-facet solar dish;
- Mr R. Fondse, Mr M.G. Kotze, and Prof W.G. le Roux for sponsoring the solar tracking system;
- The South African Universities Radiometric Network (SAURAN) for providing the solar and weather measurements that were required for this study;
- The Renewable Energy Hub and Spokes Programme of the Department of Science and Innovation (DSI) for financial support through the UP Solar Thermal Spoke.

Lastly, I would like to thank my family and friends for supporting me throughout my studies. Your motivation and support have driven me to excel and persist in this process. Then, to my lovely wife, Chanté – Thank you for always being there for me and for the endless support and assistance throughout this study; I could not have done this without you.

RESEARCH OUTPUTS

The following research outputs were published as a result of this work:

1. **Conference Paper:** P. J. A. Bezuidenhout, W. G. le Roux, and J. D. Steenkamp (2023), “Experimental Analysis of Zinc Melting Using CSP”, in C. Fleuriault, et al., Advances in Pyrometallurgy, TMS 2023, The Minerals, Metals & Materials Series. Springer, Cham. https://doi.org/10.1007/978-3-031-22634-2_21;

2. **Journal Article:** P. J. A. Bezuidenhout and W. G. Le Roux (2024), “Solar cavity receiver for melting zinc metal”, Applied Thermal Engineering, vol. 247, 122984, https://doi.org/10.1016/j.applthermaleng.2024.122984.

TABLE OF CONTENT

LIST OF FIGURES

LIST OF TABLES

NOMENCLATURE

Symbols	
a_{ss}	Actual value of the series (ss)
A_{Ap}	Area of the receiver aperture [m^2]
A_{cav}	Surface area of the cavity [m^2]
A_D	Dish incident reflective area [m^2]
c	Heat transfer efficiency constant
c_1	Zinc density coefficient [$kg\ /m^3$]
c_2	Zinc density coefficient [kg/m^3K]
C	Constant for cylinders in cross-flow
c_p	Specific heat capacity [$J/K \cdot kg$]
$c_{p_{liquid-Zn}}$	Specific heat capacity of molten zinc [$J/K \cdot kg$]
$c_{p_{solid-Zn}}$	Specific heat capacity of solid zinc [$J/K \cdot kg$]
$c_{p_{steel}}$	Specific heat capacity of mild steel [$J/K \cdot kg$]
c_v	Volumetric heat capacity [J/m^3K^1]
d	Aperture diameter [m]
D_{ap}	Diameter of the receiver aperture [m]
D_D	Dish diameter [m]
D_i	Receiver cavity inner diameter [m]
D_{ins}	Outer diameter of insulation material [m]
f_D	Dish local focal length [m]
f_s	Shading factor
f_{ss}	Forecast value of the series (ss)
g	Gravitational acceleration [m/s^2]
Gr_L	Grashof number
h_D	Height of parabola [m]
h_{in}	Internal convection heat transfer coefficient of the receiver [$W/m^2 \cdot K$]
h_o	Convection heat transfer coefficient on outer surface [$W/m^2 \cdot K$]
I	Solar direct normal irradiance (DNI) [W/m^2]
k_{ins}	Thermal conductivity of insulation material [$W/m \cdot K$]
l_c	Aperture-cavity radius ratio

L_{rec}	Receiver characteristic length [m]
L_o	Original length of the component [m]
ΔL	Change in length of the component [m]
m	Constant for cylinders in cross-flow
m_{steel}	Mass of receiver steel [kg]
m_{zn}	Mass of zinc inventory/batch [kg]
$m_{zn,liquid}$	Mass of zinc inventory/batch in molten form [kg]
Nu	Nusselt number for convection inside receiver
$Nu_{cav,forc}$	Nusselt number for forced convection from the cavity
$Nu_{cav,nat}$	Nusselt number for natural convection from the cavity
$Nu_{D,forc}$	Nusselt number for forced convection over receiver cylinder
$Nu_{D,nat}$	Nusselt number for natural convection over receiver cylinder
p	Coefficient for calculating Nusselt number for forced convection
$P(\theta)$	Function of receiver tilt angle
Pr	Prandtl number
q	Coefficient for calculating Nusselt number for forced convection
$\dot{Q}_{net}$	Nett thermal input into zinc rate [W]
$\dot{Q}_{ap,in}$	Thermal input collected at receiver aperture rate [W]
$\dot{Q}_{cond,loss}$	Thermal conduction heat loss rate [W]
$\dot{Q}_{conv,loss}$	Thermal convection heat loss rate [W]
$\dot{Q}_{rad,loss}$	Thermal radiation heat loss rate [W]
$\dot{Q}_{rad,em}$	Rate of radiation losses due to emissivity [W]
$\dot{Q}_{rad,ref}$	Rate of radiation losses due to reflection [W]
r	Coefficient for calculating Nusselt number for forced convection
$r_{i,ins}$	Inner radius of insulation material [m]
$r_{o,ins}$	Outer radius of insulation material [m]
$Ra_{D,ins}$	Rayleigh number on the insulation outer surface
R_{conv}	Convection resistance [K/W]
$Re_{D,ins}$	Reynolds number for flow over insulation material
R_{ins}	Thermal resistance of insulation material [K/W]
R_{tot}	Combined thermal resistance [K/W]

s	Coefficient for calculating Nusselt number for forced convection
ss	Series being forecast
SS	Number of series being summarised
t	Coefficient for calculating Nusselt number for forced convection
T_{bulk}	Bulk mean temperature inside the cavity $[K]$
T_{cav}	Receiver cavity temperature $[K]$
T_{∞}	Ambient temperature $[K]$
T_{ref}	Reference temperature $[K]$
ΔT	Change in temperature $[K]$
$T_{Zn,ave}$	Average zinc temperature $[K]$
N	Statistical sample size
v_{air}	Kinematic viscosity of air $[m/s^2]$
V_{wind}	Wind speed $[m/s]$
Zn	Zinc
Greek Symbols	
α	Coefficient of linear thermal expansion $[K^{-1}]$
α_{cav}	Cavity absorptance
α_{eff}	Effective absorptance
β	Receiver inclination angle $[deg]$
β_v	Volumetric thermal expansion coefficient $[1/K]$
ε_{cav}	Emissivity of cavity
ε_{eff}	Effective cavity emissivity
λ_{zn}	Latent heat of fusion of zinc $[J/kg]$
$\varphi_{rim,D}$	Dish global rim angle $[deg]$
$\eta_{th,rec}$	Thermal efficiency of the receiver [%]
η_D	Dish reflector efficiency [%]
θ	Receiver tilt angle $[deg]$
Γ	Intercept factor
μ_{air}	Ambient air viscosity $[kg/m \cdot s]$
ρ	Density $[kg/m^3]$
ρ_{air}	Density of air $[kg/m^3]$

ρ_D	Facet reflectivity [%]
φ	Incident angle of wind direction relative to receiver aperture [deg]
σ	Stefan-Boltzmann constant [$W/m^2 \cdot K^4$]]
Subscripts	
air	Air properties
ave	Average
ap	Aperture
D	Dish
cav	Cavity
$cond$	Conduction
$conv$	Convection
eff	Effective
em	Emissivity
$forc$	Forced
i	Inner
in	Internal
∞	Ambient conditions
ins	Insulation material
L	Length of receiver
nat	Natural
rad	Radiation
rec	Receiver
ref	Reflectivity
s	Surface
t	Time
tot	Total
o	Outer
$wall$	Available on the receiver cavity wall
zn	Zinc
Abbreviations	
CFL	Circular Fresnel Lens
CPC	Compound Parabolic Collector

CSP	Concentrated Solar Power
CSV	Comma Separated Values
CTC	Cylindrical Trough Collector
DAQ	Data Acquisition
DNI	Direct Normal Irradiance
EAF	Electric Arc Furnace
ETC	Evacuated Tube Collector
FPC	Flat-Plate Collector
GDP	Gross Domestic Product
HFR	Heliostat Field Reflector
HTF	Heat Transfer Fluid
ISP	Imperial Smelting Process
LFR	Linear Fresnel Reflector
MPE	Mean Percentage Error
MAPE	Mean Average Percentage Error
NEMA	National Electrical Manufacturers Association
NG	Natural Gas
PCM	Phase Change Medium
PDR	Parabolic Dish Reflector
PTC	Parabolic Trough Collector
PV	Photovoltaic
RLE	Roast-Leach-Electrowin
RMSE	Root Mean Square Error
SAURAN	South African Universities Radiometric Network
SF	Solar Furnace
SHG	Special High-Grade
STC	Solar Thermal Collectors
TC	Thermocouple
VNC	Virtual Network Computing
WOX	Waelz Oxide
WS	Water Splitting

1. INTRODUCTION

1.1 Background

The global energy sector is generally represented by the power sector, transport sector, and industry sector. The industry sector is represented by the segment of the economy that is made up of businesses that are predominantly involved in manufacturing or producing any form of product. A significant shift from fossil fuels to renewable energy sources and better building insulation regulations have resulted in a substantial reduction in greenhouse gas emissions in the power sector [1]. In recent years, the transport sector has also attracted some attention, and improved efficiencies and electrification have reduced emissions in most transport segments [1]. The industry sector has not attracted the same attention and is predicted to be, by far, the biggest greenhouse gas emission producer of the energy sector by 2060 [1]. Process heat represents two-thirds of the industrial energy demand, of which 90% is currently being supplied by fossil fuels. It is within this space that abundant opportunities exist to reduce the predicted greenhouse gas emissions by making use of renewable alternatives such as solar thermal energy. Various authors ([1 - 4]) have stated and demonstrated that it is possible to achieve temperatures in excess of 400 °C using concentrating solar technologies and that these technologies can be used together with industrial heat applications.

South Africa is classified as one of the countries with the highest solar potential in the world [5] due to the country's above-average solar irradiance, as shown in Figure 1 [6]. For comparison, the solar insolation from Direct Normal Irradiation (DNI) is approximately 2400 kWh/m² per year compared to the global average of 1340 kWh/m² per year [6]. In addition to the excellent solar resource, it is estimated that about 44% of the total energy demand in South Africa is attributed to heat generation [7]. South Africa is ideally situated to exploit the solar energy resource to not only reduce greenhouse gas emissions but also to explore more cost-effective alternatives for industrial heat supply. A struggling power utility, increasing electricity costs, talks of carbon tax increases, and sustainability incentives are all reasons that allowed the South African Solar Thermal Technology Road Map (SA-STTRM) to predict exponential growth in the solar thermal energy market until 2030 [5].

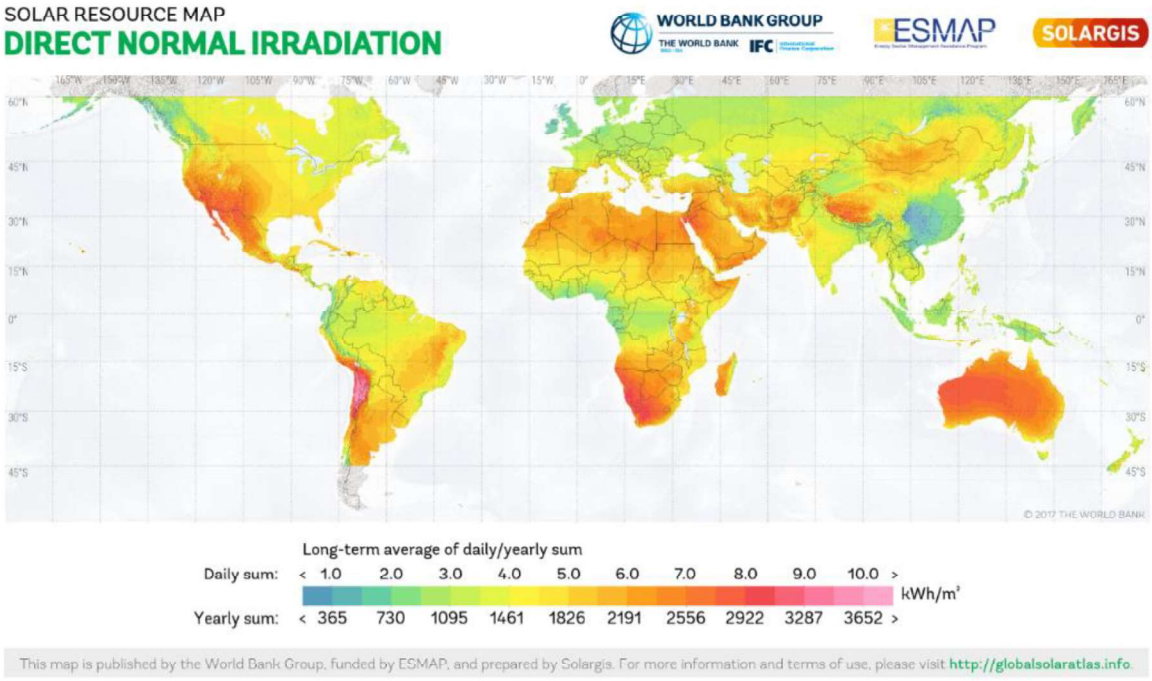

Figure 1. Direct Normal Irradiation (DNI) world map [6].

In current literature, the focus is placed on finding solar thermal energy applications within the industry sector's low and medium-temperature categories, typically associated with the agri-processing and textile industries [1, 3, 8]. Less work has been done in the high-temperature category (> 400 °C) [4], which is earmarked for mining applications [1], even though this sector accounted for approximately 10% of the global greenhouse gas emissions in 2018 (only considering primary production) [9]. The challenges that hinder the development of high-temperature applications are high capital cost, large land area requirements, and the lack of experience [10], most of which will be addressed as concentrated solar thermal technologies mature.

There exist various high-temperature industrial applications with the potential to make use of solar thermal energy, but for this study, the melting of zinc is selected. Zinc is a versatile mineral with applications ranging from metals to medicines. Zinc is deemed essential for modern living and stands fourth in terms of all metal production in the world [11]. Not only does zinc metal have favourable material characteristics permitting the use of solar thermal energy, such as a relatively low melting point and good thermal capacity, butit is also an essential part of modern renewable energy solutions as it is typically used for provideing corrosion protection to steel structures through galvanisation. Galvanisation technologies currently rely primarily on burning fossil fuels as the heat source for melting [12]. Zinc is also not being utilised to its full

potential in the South African mining environment. Even though South Africa has great potential for zinc production, noting that South Africa is ranked 5th in terms of worldwide zinc reserves [13], the minimum is mined, and all the mined material is exported for processing elsewhere [14]. This speaks to the non-existent beneficiation of this versatile mineral in South Africa and the need for a novel technology to bring the potential benefit of this mineral within reach.

Figure 2 [15, 16] shows that most of the South African zinc deposits are located in areas with exceptional solar irradiance, enabling the possibility of directly linking a solar thermal technology to the production of zinc. The dissociation and reduction of zinc oxide (ZnO) using CSP have been demonstrated by several authors [17, 18, 19, 20, 21, 22, 23]. However, little attention has been given to the direct melting of zinc metal using CSP as part of the zinc production flowsheet. One of the most common methods of producing zinc is the hydro-metallurgical or Roast-Leach-Electrowin (RLE) process, producing about 80% of the world's zinc [24]. A detailed description of the RLE flowsheet is outlined by van Dyk [25]. It typically consists of a roasting, leaching, solution purification, cooling, electrowinning, and a casting step. After the electrowinning process, during which zinc metal is plated to aluminum cathodes, the zinc metal is stripped from the cathodes and remelted at 450 °C in induction furnaces to produce ingots [25]. The significant energy demand of the RLE process, as a whole, makes it unlikely to be satisfied by current CSP technologies, but a desktop study by Sithole et al. [26] has shown that solar thermal heating can reduce the energy costs of the casting process by more than 50% and the indirect CO_2 emissions by up to 80%.

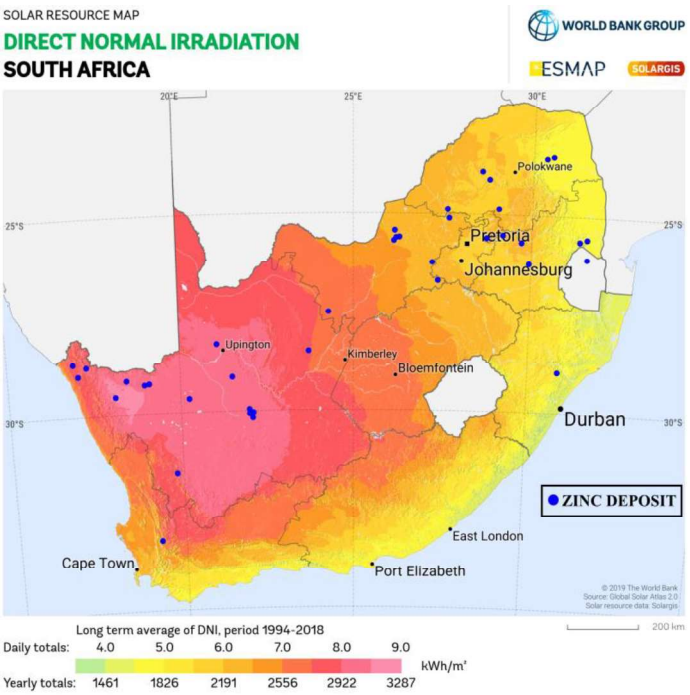

Figure 2. Zinc deposits superposed on the South African solar resource map [15, 16].

The casting step of the RLE process presents an opportunity to make use of solar thermal energy to reduce the carbon footprint of this process and has the potential for energy cost savings, especially when considering future electricity cost projections. This opportunity is not only limited to the RLE process but also for other zinc melting technologies such as galvanisation and the zinc casting industry, as zinc melting applications currently, and predominantly, rely on gas, coal, and oil-fired heat sources [12, 27]. Current melting heat sources are becoming increasingly more expensive as resources become scarcer and produce significant amounts of greenhouse gas emissions in the process of generating the required energy for melting [28]. Concentrated solar thermal energy has the potential to meet the heat demand for a variety of zinc melting applications, but the casting step of the RLE process can serve as the starting point to demonstrate this concept.

1.2 Problem statement

Currently, there exists limited literature and experimental data on the use of solar thermal energy directly for high-temperature process heat applications. Solar thermal technologies possess the ability to reduce the large carbon footprint of the industry sector, by replacing some of the heat currently being supplied by fossil fuel energy sources. The socio-economic situation in South Africa and the decline in the

beneficiation of local resources emphasises the need to find alternative mineral processing solutions. Many South African mineral resources are ideally located to exploit South Africa's excellent solar resource to its full potential. The material characteristics and location of deposits make zinc a good starting point for determining the feasibility and practicality of using solar thermal technologies for high-temperature process heat applications. An experimental setup is therefore required to test and evaluate the practicality and feasibility of using solar thermal energy to melt zinc and how it can be applied to zinc metal flowsheets.

1.3 Justification of research

Not only is the initiative to reduce the carbon footprint of industrial applications driven and motivated by political and environmental pressures, but also by financial incentives such as increasing fuel and electricity costs and carbon taxes. The increase in maturity of renewable energy technologies and the increasing uptake of these technologies already indicate cost prediction trends well below that of existing fossil fuel energy sources [27, 28]. These trends allow for making the assumption that the energy market will be motivated to make use of renewable energy sources in the future.

The cost trends, mentioned above, can also be used to argue that the best way forward would be to use electricity generated by renewable energy sources such as the sun. However, the generation of electricity from the sun, to be used for heating applications, results in significant conversion losses in the process. By directly making use of the sun's energy in a CSP application, the renewable heat-to-electricity-to-heat conversion loss is avoided, making the renewable energy application more efficient [3, 29]. Electrification also requires a reliable power network, which is unfortunately not the case in the South African context [30].

This study will, therefore, be instrumental in determining the feasibility and practicality of linking a solar thermal technology to a high-temperature industrial heat application. The industrial heat application selected for this study is the melting of zinc metal due to the potential impact on the South African mineral processing environment and other zinc metal-related technologies such as thermal storage applications, galvanisation, and zinc cathode remelting. Authors such as Fernández-González, et al. [31] and

Eglinton, et al. [10] have expressed the potential for zinc-solar applications in energy storage and mining applications.

1.4 Research objective and main contribution

The research carried out in this work is aimed at investigating the possibility of combining a solar thermal technology with a high-temperature industrial process heat application. This study set out to experimentally demonstrate the melting of zinc, using only concentrated solar power, in order to provide valuable insight into the operational requirements of this technology application. By demonstrating that the small-scale processing of a low-melting-point metal is achievable, using only CSP, the entry barrier for metal melting applications using a renewable energy source can be lowered. This technology can be applied to a range of applications, including but not limited to: casting (including small-scale battery technology and ingot casting as part of the RLE process), metal recycling, galvanisation, and small-scale thermal storage. Zinc was used to demonstrate this concept given the importance of this metal and the favourable material properties. The study will therefore also serve as a starting point to demonstrate the potential for using CSP to beneficiate local resources, such as zinc ore in the South African context, and for the use in other melting applications. An analytical model was developed to serve as a desktop tool for the further development of this technology, and the accuracy thereof was demonstrated by comparison with experimental data, providing the necessary confidence in the model. A validated model can be used to further refine the design parameters of this technology application or as a tool for feasibility studies to determine, for example, the molten zinc production rates for a given location.

1.5 Overview

Chapter 2 consists of a literature review of information relevant to this study and provides supporting theoretical background to the design decisions and calculations made during the execution of the study. Chapter 3 describes the experimental investigation, which includes the experimental design as well as the experimental method. Chapter 3 also provides the details of the thermal analysis conducted as part of this study and will outline the theory behind the computational model developed as part of this work. Chapters 4 and 5 contain the results and discussion of both the experimental and analytical work. The research together with some recommendations for future work, are summarised in Chapter 6.

2. LITERATURE STUDY

2.1 Introduction

It has been shown in the previous chapter that South Africa has an excellent solar resource with the potential to be used in high-temperature processing heat applications. The current study aims to show that it is possible to process low-melting-point metals using solar thermal energy. However, a thorough understanding of existing and potential solar thermal technologies is required before this can be done. In this chapter, the direct use of solar thermal energy for melting metals with a medium melting temperature as well as other solar thermal technologies operating in a similar temperature range, will be investigated. Thereafter, a review will be conducted on the fundamental components of a solar thermal system. A comprehensive description of each component in the solar thermal system is required to ensure a proper understanding of the system as a whole and how the various components are integrated to achieve the required outcome. The literature and information gathered in this chapter will be used as the basis for the design of the experimental setup.

2.2 Zinc metal

Considering that zinc metal had been identified as the metal to be used to demonstrate melting (using only CSP input) and that an analytical model will be validated against these results, the material properties of zinc had to be well understood. This section will investigate the material properties of zinc metal that will be included and used in the analytical model. The more accurate these material properties, the more accurate the behaviour of the zinc metal can be modelled. A brief investigation of existing zinc extraction processes will also be included to provide context for the existing zinc melting technologies and processes.

2.2.1 Zinc material properties

To determine what specifications a solar thermal technology will need to comply with to be able to melt zinc metal, a comprehensive understanding of the material properties of zinc metal is required. Zinc is classified as a transition metal with an atomic number of 30 and has five stable isotopes: ^{64}Zn (48.63%), ^{66}Zn (27.90%), ^{67}Zn (4.90%), ^{68}Zn (18.75%), and ^{70}Zn (0.62%) [32]. Zinc is slightly more abundant than copper in the Earth's crust, making it the 23rd most abundant element on Earth [32], with approximately 65 grams for every ton of Earth's crust [33]. Zinc is not only an essential trace element in the human body but also finds applications ranging from

plant nutrition to metal galvanisation. The effective protection against corrosion and the ability to be cast in complicated shapes make zinc metal essential in various industrial and household products [24]. Aside from being essential in its pure form, approximately 25% of zinc is earmarked for alloying applications [24].

2.2.1.1 Density

By using large bodies of data and experimental testing, Assael et al. [34] found that liquid zinc metal shows a linear decrease in density with an increase in temperature. This allowed the authors to propose a linear regression model that describes the density of liquid zinc as a function of temperature, as shown in Equation 1 (with the required reference temperature and coefficients shown in Table 1):

$$\rho_{zn} = c_1 - c_2(T - T_{ref}) \quad (1)$$

Table 1. Coefficients and reference temperature for the density equation with a 95% confidence level [34].

$T_{range}(K)$	$c_1\ (kg\ m^{-3})$	$c_2\ (kg\ m^{-3}\ K^{-1})$	$T_{ref}\ (K)$	$Deviation(2\sigma)(\%)$
692 - 910	6559	0.884	692.677	0.7

Using any temperature within the temperature range, the density of liquid zinc at that given temperature can be calculated. Zinc metal has a density of $\rho_{solid} = 7140\ kg\ m^{-3}$ [35] at room temperature (300 K) and a density of $\rho_{liquid} = 6559\ kg\ m^{-3}$ [34] as it transitions into the molten state. By considering the density in the solid state as compared to the liquid state, a volumetric expansion of approximately 8.14% is noticed and should be kept in mind when designing a containment vessel.

2.2.1.2 Linear thermal expansion

The linear thermal expansion of a material is described by Equation 2.

$$\Delta L = \alpha L_o \Delta T \quad (2)$$

The coefficient of linear thermal expansion of pure solid zinc is given as $\alpha_{zn} = 39.7\ ppm/°C = 39.7 \times 10^{-6}\ (K^{-1})$ [36].

2.2.1.3 Thermal conductivity

Thermal conductivity describes a material's ability to conduct heat. The higher the thermal conductivity of a material, the more effective the material is at transferring heat. Thermal conductivity depends on the material's temperature, and for most pure metals, the thermal conductivity will decrease with an increase in temperature [37]. Most references only refer to the thermal conductivity of solid materials. However, Touloukian et al. [38] have done substantial work on the thermal conductivity of metallic elements and alloys and reference some thermal conductivity values for molten zinc. The solid and liquid thermal conductivities of zinc at various temperatures are listed in Table 2.

Table 2. Thermal conductivity of zinc as a function of temperature [33, 36].

Solid		***Liquid***	
Temperature (K)	**Thermal conductivity** $(W\ m^{-1}\ K^{-1})$	**Temperature** (K)	**Thermal conductivity** $(W\ m^{-1}\ K^{-1})$
200	118 [35]	700	49.9 [38]
400	111 [35]	800	55.7 [38]
600	103 [35]	900	61.5 [38]
692.65	100 [38]	1000	67.3 [38]

2.2.1.4 Heat capacity

Heat capacity (c) is a material property defined as the amount of heat to be added to a given mass of material to cause a unit change in temperature in the material [35]. Heat capacity can be divided into specific heat capacity (c_p) which is the heat capacity of a material divided by the mass, and volumetric heat capacity (c_v) which represents the heat capacity of a material divided by the volume. The volumetric heat capacity is calculated using the specific heat capacity and the material density, as shown in Equation 3 [35].

$$c_v = \rho\ c_p \tag{3}$$

Bergman et al. [35] have shown that the specific heat capacity of zinc metal increases with temperature (see **Error! Not a valid bookmark self-reference.**).

Table 3. Specific heat capacity of zinc at various temperatures [35].

Temperature (K)	***Specific heat capacity*** $(J\ kg^{-1}\ K^{-1})$
100	297
200	367
400	402
600	436

2.1.2 Zinc extraction processes

The most common raw material for the production of zinc is known as sphalerite or zinc sulfide (ZnS) [24], of which the deposits in South Africa are highlighted in Figure *2*. Zinc is extracted from the raw ore by either employing hydro-metallurgical processes or pyro-metallurgical processes. Only about 20% of worldwide zinc production makes use of the pyro-metallurgical route [24]. Due to the high energy consumption and low yields, pyro-metallurgical processes such as the retort and electrothermal process are becoming less common. The pyro-metallurgical process is known as the Imperial Smelting Process (ISP). ISP involves feeding a sinter mix of ZnO, PbO, coke, and limestone into a furnace. In the furnace, the ZnO-PbO mixture is reduced, and a lead bullion is collected at the hearth of the furnace, while zinc vapour is condensed at the top by circulating liquid lead at 600 °C [24]. Due to a solubility difference between Zn and Pb, the two metals are separated with gradual cooling.

The most common hydro-metallurgical process for the production of zinc is known as the Roast-Leach-Electrowin (RLE) process, and about 80% of the world's zinc output is produced in this way [24]. The RLE process is started by roasting zinc sulfide in a fluidised-bed roaster to produce zinc oxide, also known as calcine [25]. This carbothermic process is maintained at approximately 930 °C to 950 °C with the help of water as a coolant [24, 25]. This temperature is within the range of solar thermal technologies but would require accurate and expensive optics and collector surfaces to obtain and maintain these high temperatures, as will be discussed in the next section. In the roasting step, sulphur dioxide (SO_2) gas is produced as a by-product. The zinc oxide is then milled to a powder and processed in a series of leaching units,

maintained at around 150 °C using heat produced during the roasting step [25]. Sulphuric acid (H_2SO_4), produced from the SO_2 by-product, is used as a leaching agent to help remove unwanted elements (Pb, Si, Fe, Mn, Mg, and Ag) while producing a liquid zinc concentrate [25]. This zinc concentrate is then processed at the purification stage. The purification stage involves precipitation by adding zinc dust to precipitate unwanted elements, such as Cu, Ni, Co, Sb, Cd, and Ge [25]. The zinc concentrate solution is fed into an electrowinning process where the zinc metal is plated onto aluminium cathodes [25]. The zinc metal is then stripped from the cathode and remelted at 450 °C, 30° C above the melting point of zinc, in an induction furnace to produce ingots [25]. The remelting temperature of 450 °C is well within reach of CSP technologies and is an area where solar thermal has the potential to reduce the carbon footprint of the zinc production flowsheet [26]. A desktop study by Sithole et al. [26] has shown that solar thermal remelting of the zinc cathodes, produced by the RLE process, can reduce the energy cost of the casting process by more than 50% and the indirect CO_2 emissions by up to 80%. These findings make this application an attractive starting point for demonstrating the concept of applying a CSP technology as the heat source for a high-temperature industrial application.

Another zinc extraction process worth mentioning is zinc distillation. Zinc distillation is a process during which Special High-Grade (SHG) zinc is produced. In this process, zinc is distilled off by heating the feed material past zinc's vapour point (950 °C) to condensate very high-purity zinc in a condenser [31, 39]. The feed product can be processed zinc from the conventional zinc flowsheet, or it can be done from primary ore feed sources. The two most common processes employed for producing SHG zinc are the New Jersey Process, which makes use of fossil fuel-heated boilers, and the Zincref process, which is electrically powered [39]. All of the existing technologies for producing SHG zinc rely on fossil fuel-supplied energy sources, again allowing the opportunity to investigate greener heat source alternatives such as CSP.

Aside from primary zinc production, a significant focus has been placed on establishing processes that tend to secondary zinc sources. Zinc waste streams, still containing zinc, are classified as hazardous waste under the Basel Convention and must be treated before they can be stored in a landfill [24]. Secondary zinc sources include material streams such as zinc scrap, old zinc anodes, zinc dust from electric arc furnace (EAF) operations, zinc dross from galvanising industries, and many more.

Technologies such as the AUSMELT process, Mintek Enviroplas, QSL process (also known as the Waelz kiln process), ZINCEX process, EZINEX process, to name a few, have been developed to tend directly to secondary zinc streams [24]. Selecting a suitable process depends on factors such as the zinc content in the waste stream, the volume, the cost of electricity in the region, and the quality of pure zinc required. Most of these recycling processes involve the fuming of zinc, as in the case of SHG zinc production, which requires operating temperatures of up to 950 °C. This requirement also allows CSP to be considered as an alternative heat source for the recycling of zinc waste streams.

2.3 Solar thermal technology

An understanding of the different solar technologies and their characteristics is required to select the most suitable solar thermal technology for the intended application. Solar energy can be converted to either electricity, by making use of photovoltaics (PV), or to thermal energy by making use of solar thermal collectors (STC) [3]. As this study intends to directly link solar thermal energy to an industrial application, PV technology will be disregarded and only focus on STC technologies. STC technologies, in turn, can be divided into three subcategories: stationary, single-axis tracking, and two-axis tracking [2, 38]. Within these three categories, there are two basic types of solar collectors: non-concentrating and concentrating. Non-concentrating collectors are characterised by a similar intercepting and absorber zone, which entails that the receiver also makes up the absorber. The combination of the receiver and absorber can sometimes increase the design complexity and even increase the production costs [3]. Concentrating collectors, on the other hand, make use of a large collector area to concentrate solar radiation to a reduced absorber/receiver area. By doing so, higher operating thermal efficiencies are achievable as a result of reduced heat losses when compared with non-concentrating collectors occupying the same surface area [2, 3]. Figure 3 shows some of the more common solar thermal collector technologies.

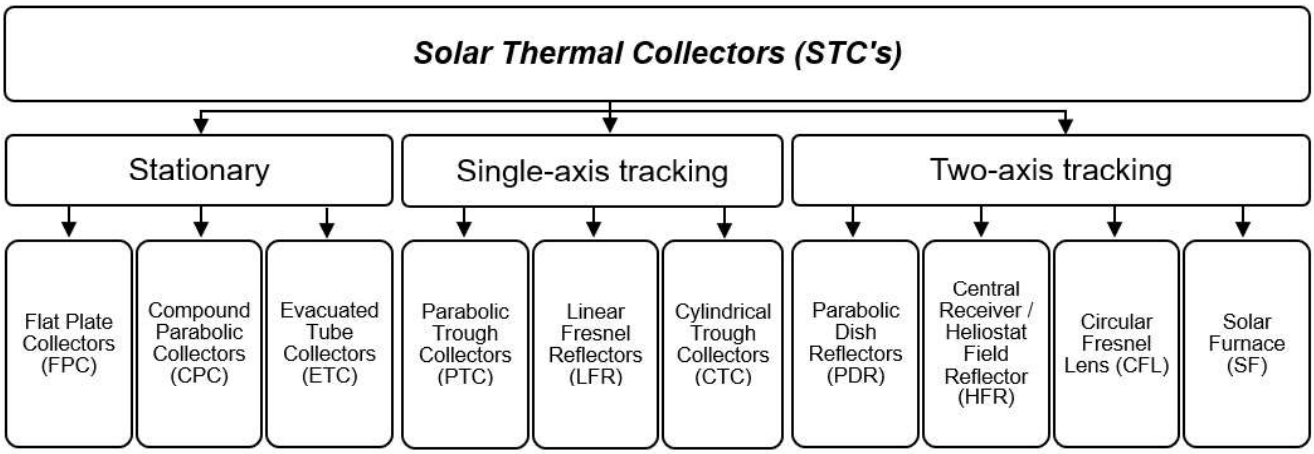

Figure 3. STC technology summary [2, 3, 38].

Stationary STC's are permanently fixed in one position and do not track the sun [2]. Due to the lack of solar tracking, this type of STC's are usually arranged in such a manner as to enlarge the collection area and positioned at a predetermined orientation and tilt angle for maximum efficiency. The tilt angle and orientation are dependent on the geographical location of the stationary collector system [40].

Concentrating collectors are typically fitted with some form of solar tracking, be it single or two-axis tracking. The solar irradiance intensity is affected by diurnal and seasonal movement [41]. Therefore, by fitting a solar tracking system to a collector, one can compensate for this movement to ensure an optimum orientation relative to the sun. Mousazadeh et al. [41] mention that it is possible to increase the collected solar energy by 10% to 100% if a tracking system is employed. Tracking systems are, however, not recommended for low-capacity systems due to the added cost and energy requirements [3, 38, 39].

Single-axis tracking collectors are typically positioned along the North-South line and then track the sun in only one direction, from East to West [3, 40]. This is achieved by rotating the solar collector along with a single pivot point throughout the day. Single-axis tracking is usually the more cost-effective tracking solution due to the reduced complexity of the system, but the system cannot compensate for the seasonal movement of the sun, which can result in efficiency losses [3]. Single-axis tracking is typically found with parabolic trough collector (PTC), linear Fresnel reflector (LFR), and cylindrical trough collector (CTC) applications [40].

Two-axis tracking, also known as the altazimuth method [2], requires a tracking device to orientate the collector in both altitude and azimuth. This will, theoretically, allow the collector to follow the sun's movement exactly. To achieve two-axis tracking, the tracking system has two pivot points, each with its own motor. One motor controls the azimuth angle, while another motor controls the elevation angle. Employing a two-axis tracking system makes it possible to adjust for diurnal and seasonal changes, ensuring optimal efficiency all year long. Two-axis tracking enables concentrating collector technologies such as parabolic dish reflectors (PDRs) and heliostat field reflectors (HFRs), also known as solar towers, to achieve very high efficiencies due to optimum solar exposure [3].

Based on the summary of STC technologies in Table 4, only concentrating technologies with two-axis tracking, such as PDRs and HFRs, will be able to achieve operating temperatures high enough to melt zinc metal at 420 °C. Due to the initial cost and scale of HFR setups, it would not be feasible to make use of this technology for the intended study. PDR is widely regarded as the most efficient solar concentrating technology [42], not only because of excellent optical performance but also because mass-production techniques can be applied to limit the production cost of these units [42]. Considering that a single dish represents a full CSP system, operating temperatures similar to HFR are achievable, but with a significantly smaller footprint and at lower cost. The availability of PDR test facilities at research institutions such as the University of Pretoria and Mintek made PDR the ideal testing platform for high-temperature CSP applications. For the remainder of this literature study, a focus will therefore be placed on PDR technology and how it can be employed to provide energy for the intended high-temperature industrial application.

Table 4. Summary of STC technologies [2, 3, 38, 40, 41].

Type	***Description***	***Absorber type***	***Concentration ratio***	***Temperature range [K]***	***Tracking***
Flat plate collector	Translucent glass sheet covering an absorber plate. Copper tubes are brazed to the absorber plate in which an HTF is heated.	Flat	1	300 - 350	None
Compound parabolic collector	Translucent glass covers two parabolic reflecting surfaces, and an absorber tube is fitted at the bottom. Design can also consist of a series of absorber tubes, individually covered in an evacuated glass tube, fitted into a compound parabolic collector.	Tubular	1-5	330 - 510	None
Evacuated tube collector	Consists of a pipe enclosed in a glass tube. The pipe uses a PCM to heat a working fluid in a heat exchanger. This system can also be used to directly heat an HTF in an enclosed glass tube.	Flat	1	320 - 480	None
Parabolic trough collector (PTC)	A parabolically shaped reflector trough focuses solar radiation on an absorber tube containing an HTF. The HTF is typically inside a pipe and an evacuated/non-evacuated glass tube.	Tubular	15 - 45	330 - 580	Single

Type	*Description*	*Absorber type*	*Concentration ratio*	*Temperature range [K]*	*Tracking*
Linear Fresnel reflector	A linear mirror array focuses solar radiation on a fixed absorber tube containing an HTF.	Tubular	10 - 40	330 - 520	Single
Cylindrical trough collector	Similar to a PTC, but the trough is cylindrical, resulting in the solar rays converging on a focal plane rather than a focal line.	Tubular	10 - 50	330 - 580	Single
Parabolic dish reflector (PDR)	A parabolically shaped reflector dish that concentrates solar radiation to a focal point.	Point	100 – 1000	380 – 1770	Two
Heliostat field reflector (HFR)	A large heliostat field of individual mirrors that focuses sunlight to a central tower receiver.	Point	100 – 1500	420 – 2280	Two
Circular Fresnel lens	A series of convex lens sections are used to focus solar rays to a focal plane.	Point	2640	1500 – 2000	Two
Solar furnace	Similar to an HFR, it also uses a heliostat field, but a secondary concentrator increases the solar flux even further.	Point	<5000	<3500	Two

2.4 Existing technologies

2.4.1 Zinc metal processes

Zinc is one of the most widely used non-ferrous metals [24], after copper and aluminium, illustrating the usefulness and importance of this metal. Although zinc can be found in various markets and applications, the two most common are in the use of galvanisation and as an alloying element for casting purposes [24, 25]. Both of these applications, in general, need the zinc metal to be in the molten form. It is, therefore, worth investigating the processes and technologies used to generate the molten zinc for these two most common markets of zinc metal.

Numerous processes exist in which zinc metal is prepared and processed for alloying and casting applications. Zinc is melted in gas-fired, oil-fired, electric, or coal-fired furnaces with capacities of up to 100 tons or by low-frequency induction furnaces with a capacity of a few tons [43, 44]. The metal is typically maintained at a temperature above the melting point, but below 500 °C, to minimise the loss by oxidation [43, 44]. In the melting process, alloying elements are either added to the zinc, or zinc is added as an alloying element to obtain the required material composition. The molten material is then transferred to the next processing step, which can be anything ranging from a die-casting station to a forming press.

The most common application of using zinc metal is galvanisation, which accounts for over 80% of the zinc distribution in the South African market [25]. To illustrate the importance of the galvanising process – it is believed that monetary losses in steel parts due to corrosion are equal to approximately 5% of the Chinese GDP [12]. It is believed that this figure can be lowered by up to 30% if effective protection measures, such as galvanising, are implemented [12]. One of the most common galvanisation technologies is what is known as hot-dip galvanising. In this process, steel or iron is coated in a layer of zinc to improve the corrosion resistance of the base metal.

The hot-dip galvanisation process starts with cleaning the steel sections, that are to be galvanised, with caustic soda to remove oil and grease, then pickling steel in an acidic solution to remove mill scale, after which it is rinsed off before being submerged in a molten zinc bath. The zinc bath is obtained by heating a kettle, utilising different heat sources, most of which are from the burning of fossil fuels (coal, oil, diesel, and natural gas) or electricity [12]. The zinc kettle is a large steel container which is used

to contain the molten zinc, the size of which is determined by the size of the steel sections it needs to be able to accommodate. The zinc kettle is typically maintained at temperatures of between 440 °C and 460 °C, during which the steel sections are submerged and retracted from the molten bath. The duration of the submersion depends on the galvanisation layer thickness required. Thereafter, the coated sections undergo post-treatment, including a quenching and passivating step. The quenching and passivating steps allow the galvanised sections to be ready for storage sooner and to avoid wet storage stains [12]. The galvanising bath is the largest energy consumer of the entire hot-dip galvanising process, consuming 66% of the total required energy, followed by the heating of the flux and caustic tanks (30%), which are used to clean and prepare the steel sections before galvanisation [12]. These figures speak to the large energy consumption by the heating source of a galvanisation process, which can theoretically be replaced by making use of solar thermal energy. The operational temperatures of the hot-dip galvanisation process are well within reach of concentrated solar thermal energy, and by using the heat directly, one would avoid the conversion efficiencies that need to be considered when renewable electricity, such as electricity generated by PV panels, is proposed as an alternative.

2.4.2 Zinc-related solar thermal applications

2.4.2.1 Thermal reduction of ZnO (Water/CO_2 splitting) using solar thermal energy

Zinc can also be applied in the oxide form to renewable energy storage applications. One of these applications is in the production of syngas through the two-part water-splitting process (WS). The ZnO/Zn system is ideal for WS due to its combination of suitable thermodynamic properties [23], such as the fact that it is satisfactorily non-precious to react with water and has a low atomic weight resulting in a high energy content per mass [23]. In the first step of WS, as shown in Equation 4, the thermal reduction of ZnO to Zn occurs at temperatures above 2000 K, which can theoretically be obtained by solar thermal energy. This step is followed by the exothermic reaction between Zn and H_2O and/or CO_2 at temperatures in the range of 1300 K, as shown in Equations 5 and 6 [18]. The described chemical reactions are used for the production of syngas, and the ZnO produced can then be returned to the solar reactor to close the cycle [18].

Step 1 – Exothermic reduction of ZnO (Using solar thermal energy).

$$ZnO_{(s)} \rightarrow Zn_{(g)} + \frac{1}{2}O_2 \quad (4)$$

Step 2 – Exothermic oxidation of Zn.

$$Zn + H_2O \rightarrow ZnO_{(s)} + H_2 \quad (5)$$

$$Zn + CO_2 \rightarrow ZnO_{(s)} + CO \quad (6)$$

There exist numerous designs, ranging from concept designs to pilot-scale plants, to demonstrate the dissociation of ZnO (only the first step) as well as water/carbon dioxide splitting. Even though the production of syngas using solar thermal energy as a heat source has been successfully proven, it is stated that further research efforts are required to achieve feasibility on a commercial scale [18, 23].

It is, however, helpful to study the different types of receivers/reactors investigated that led to the above-mentioned conclusion. The first type of receivers/reactors used to investigate the solar thermal reduction of ZnO were directly irradiated receivers [23]. One of the first prototype receivers was developed and tested at the Paul Scherrer Institute (PSI) – this receiver was known as the SLOPE reactor [18, 22], as shown in Figure 4 (a) [22]. The successor to the SLOPE receiver was a 6.3 kW rotating cavity receiver, capable of operating at temperatures up to 2000 K, named ROCA (Figure 4 (b)) [47]. As a last attempt, the ROCA receiver was followed by a 10 kW receiver named ZIRRUS, shown in Figure 4 (c) [48]. All three of these receivers relied on a quartz window-covered aperture, through which ZnO particles were directly irradiated by concentrated solar radiation, and the airtight environment prevented the re-oxidation of the dissociated zinc.

(a)

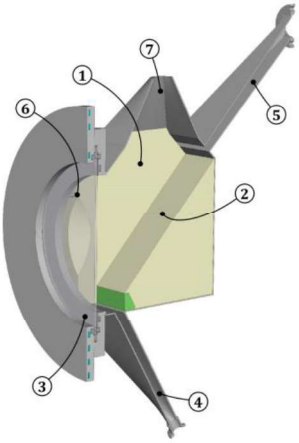

1 – Reaction chamber, 2 – Sloped reaction surface, 3 – Quartz window, 4 – Outlet for non-reacted ZnO, 5 – Feed shute, 6 – Inert gas stream, 7 – Chimney for gaseous products.

(b)

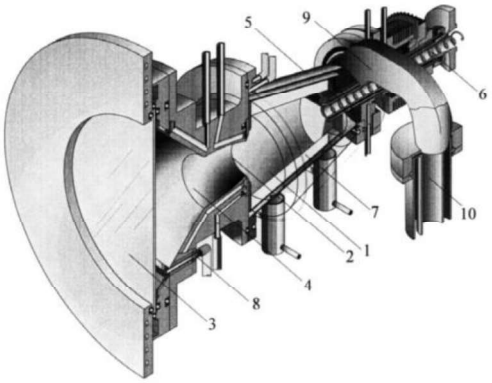

1 - Rotating cavity, 2 – Cavity aperture, 3 – Quartz window, 4 – CPC, 5 – Outside conical shell, 6 – Reactant feeder, 7 – ZnO layer, 8 – Purge gas inlet, 9 – Product outlet, 10 – Quench device.

(c)

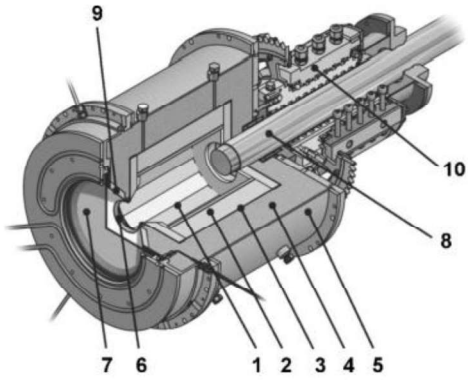

1 - Rotating cavity lined with ZnO sintered tiles, 2 – Insulation, 3 – Ceramic matrix composite, 4 – Alumina fibres, 5 – Al reactor shell, 6 – Aperature, 7 – Quartz window, 8 – Dynamic feeder, 9 – Conical frustum, 10 – Rotary joint.

Figure 4. Cavity receivers designed by PSI with (a) named SLOPE [22], (b) ROCA [47], and (c) ZIRRUS [48].

An alternative to the rotary cavity receiver/reactor was proposed by Koepf et al. and was named GRAFSTRR abbreviated from “Gravity-Fed Solar Thermochemical Receiver/Reactor” [17]. This receiver avoided the operational and maintenance complexities associated with the rotating cavity design. Seeing that this receiver was gravity-driven, it had to be used with a beam-down solar concentration system [17].

The reactor is closed off to the atmosphere by the use of a water-cooled window at the aperture. Fifteen vibrating feeders distributed the ZnO feed material evenly over the conical reaction surface, creating a continuously moving material bed, as shown in Figure 5 [17].

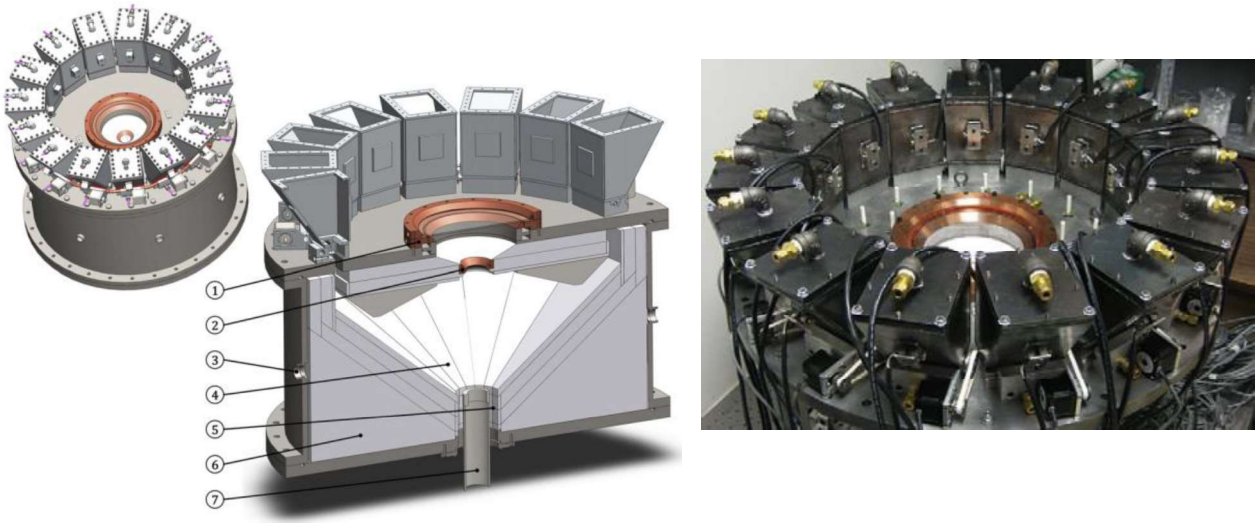

1 – Water-cooled window mount and vortex flow generator, 2 – Water-cooled cavity aperture, 3 – Data-acquisition cavity access port, 4 – Alumina tile reaction surface, 5 – Annular solid ZnO exit, 6 – Bulk insulation and cavity support, 7 – Central vapour product and gas exit.

Figure 5. The GRAFSRR beam-down solar thermochemical reactor [17].

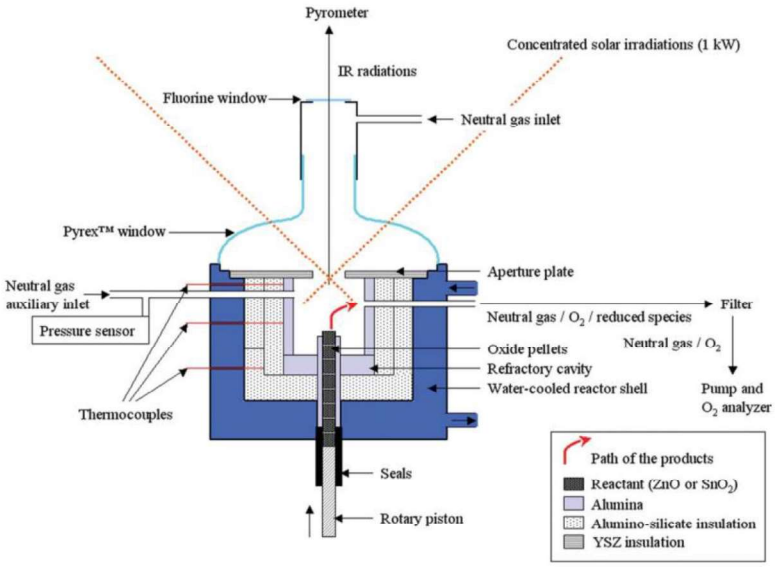

Figure 6. Moving-front solar thermal reactor for the dissociation of ZnO [19].

Another approach to mitigate the problems associated with rotating cavity reactors/receivers, such as the sealing of rotating equipment and the difficulty of adding measurement equipment, is to use a “moving front reactor” [19, 47]. This

reactor/receiver is typically a vertical cavity, covered with a Pyrex window, that contains a solid reactant that can be pushed into the cavity by a screw piston [23]. An example of such a design is shown in Figure 6 [19].

2.4.2.2 Carbothermal reduction of ZnO using solar thermal energy

An alternative to the thermal dissociation of ZnO is the carbothermal reduction of ZnO. In this process, solar irradiation is used as the source of process heat, and a carbon source is added to aid in the ZnO reduction step. When compared to the thermal dissociation of ZnO, the addition of carbon results in some important advantages. The addition of carbon reduces the required process temperature by approximately 600 K, and the product gas produced consists of $Zn_{(g)}$ and CO, rather than $Zn_{(g)}$ and O_2 [18]. The condensation of Zn from the above-mentioned gas mixture prevents Zn vapour and O_2 from recombining into ZnO [18]. These advantages do, however, come at the expense of consuming a carbonaceous feed material and producing an ash byproduct.

The simplified reaction options for the carbothermal reduction of Zn are shown in Equations 7 and 8 [18]:

$$ZnO + C \rightarrow Zn + CO \quad (7)$$

$$ZnO + CH_4 \rightarrow Zn + CO + 2H_2 \quad (8)$$

In the first reaction, a solid carbonaceous material is used, and CO gas is produced as a by-product. In the second reaction, methane is used as a reducing agent to produce syngas as a by-product, which can be converted to liquid hydrocarbons [18].

Although the carbothermic reduction of the zinc-oxide can be used as part of a zinc-air fuel cell cycle ($Zn + O_2 \rightarrow ZnO$) or to produce hydrogen ($Zn + H_2O \rightarrow ZnO + H_2$) and liquid fuels ($Zn + CO_2 \rightarrow ZnO + CO$) [18], extensive research has been done on using this process for the carbothermic production of zinc metal using solar power [18, 20, 21, 48, 49, 50]. Steinfeld et al. were among the first to propose and test a novel solar chemical reactor for the co-production of metallic zinc and syngas [20]. The receiver named “SynMet” was designed for the carbothermal reduction of ZnO using natural gas (NG) as a reducing agent and concentrated solar thermal energy as the heat source. The solar reactor/receiver design consisted of a circular cavity that induced a vortex flow of solid ZnO particles entrained in the active gas, fed from the back of the cavity, which were then directly exposed to concentrated solar

radiation [20]. A schematic of this receiver is shown in Figure 7 [20]. With a net solar power input of 5 kW, this receiver reached temperatures of up to 1600 K, and the carbothermic reduction of ZnO was achieved. The first tests yielded up to 90% chemical conversion of the zinc in a single pass [20], and technical feasibility was demonstrated.

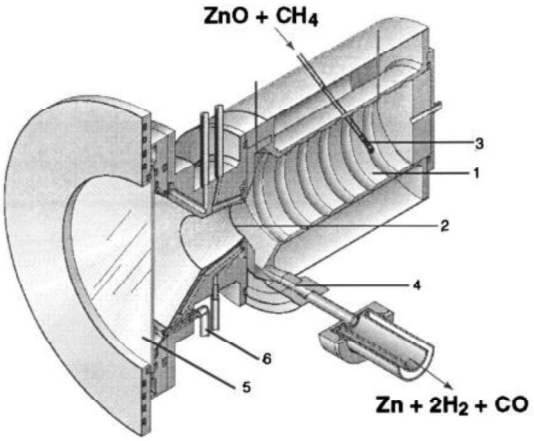

1 - Vortex-inducing cavity, 2 – Aperature, 3 – Inlet port for reactants, 4 – Outlet port for chemical products, 5 – Quartz window, 6 – Auxilary gas flow

Figure 7. SynMet solar chemical receiver for co-production of metallic zinc and syngas [20].

The successful results obtained from the SynMet project and other concept designs [48, 49, 50] enabled the formation of a joint research project in the early 2000s, named SOLZINC, with funding from the European Commission [18]. The project was aimed at scaling up the reactor technology for what was called the most promising process for the solar production of Zn by carbothermic reduction of ZnO [53]. After completing various laboratory-scale tests, a 300 kW pilot solar reactor was designed and fabricated as part of the SOLZINC project. This reactor/receiver was successfully commissioned and operated using a beam-down solar concentrator system, which consists of a heliostat field and solar tower, situated at the Weizman Institute of Science (WIS) [21]. The solar reactor featured two cavities in series. The upper cavity served as the solar absorber while the bottom cavity was used as the reaction chamber [21]. This arrangement allowed the upper cavity's aperture quartz window to be protected against process particles and condensing gases while serving as a thermal shock absorber [21]. The two cavities were separated from one another by a SiC/graphite divider, and both the upper and lower cavities were fabricated from

steel and lined with foam insulation [21]. The reactor was batch-operated at temperatures in the 1300 K to 1500 K range and achieved a zinc production rate of 50 kg/h with a purity of 95% [21]. A thermal efficiency of 30% was achieved, which describes the ratio of reaction enthalpy to the solar power input [21]. A schematic of the reactor as well as a photo of the actual SOLZINC plant is shown in Figure 8 [21]. This technology shows greater potential for commercial applications. However, it is still associated with significant risk if it were to be used for a first-of-its-kind solar chemical plant [18].

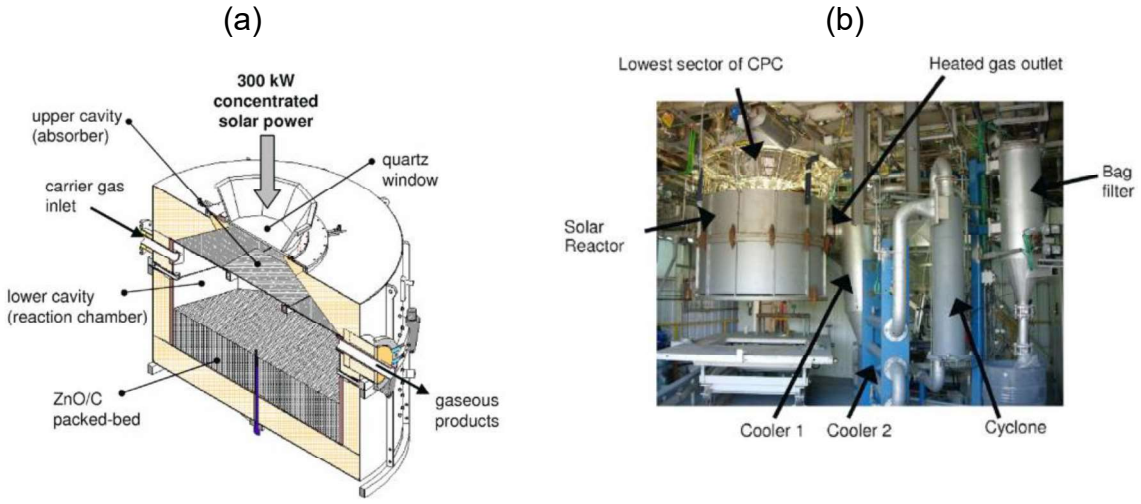

Figure 8. SOLZINC reactor (a) design schematic and (b) actual construction [21].

2.4.2.3 Recycling of Waelz oxide using solar thermal energy

Another zinc-related technology worth mentioning for which concentrated solar thermal energy is used is the thermal recycling of Waelz oxide (WOX). WOX is a secondary product produced as dust during the recycling of galvanised steel in an electric arc furnace (EAF). For every ton of galvanised steel recycled, 15 kg to 25 kg of dust is generated, which contains approximately 18-35wt.% ZnO [54]. This dust is classified as a hazardous solid waste material and needs to be disposed of in specially allocated landfills, at a high disposal cost, or treated to take advantage of the valuables in the dust [54]. More than 95% of EAF dust recycling is currently done through a pyrometallurgical process named the Waelz process. In this process, the EAF dust is fed into a kiln together with a carbonaceous reducing agent and a flux, typically silica or lime. The feed stream is heated to 1470 K, and an iron-rich Waelz slag and the WOX are produced [54]. The WOX contains approximately 60% to 65% Zn in the form of ZnO, together with some chlorides and fluorides [54]. Tzouganatos et al. [54]

proposed a process in which the WOX is recycled using concentrated solar thermal energy. The authors demonstrated both the solar clinkering of the WOX and the carbothermal reduction of the clinkered WOX [54]. A heliostat field and a beam-down solar tower were used to provide heat to the system. A schematic of the reactor used for the solar thermal recycling of the Waelz oxide is shown in Figure 9 [54]. Solar clinkering of WOX was successfully demonstrated using the described solar reactor, and the chlorine (Cl) and lead (Pb) content was shown to be lower than that of conventional processes [54].

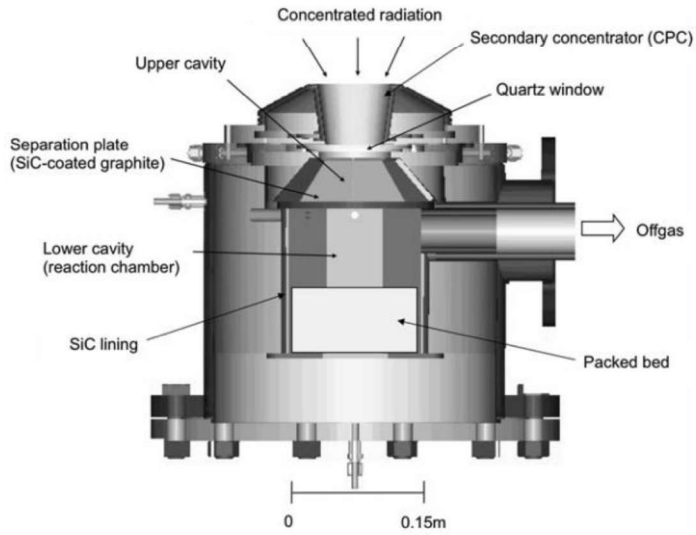

Figure 9. Schematic of a packed-bed reactor for solar recycling of Waelz oxide [54].

2.4.3 Other metal-melting solar thermal applications

Aside from the thermal and carbothermal reduction of zinc using concentrated solar irradiance, limited literature exists on the subject of solar melting of zinc metal. Therefore, to better understand the solar melting of medium melting-temperature metals, an investigation was launched into the solar melting of aluminium, as comparable temperature ranges are applicable, as well as solar melting in general.

2.4.3.1 Heliostat field applications

The majority of the concept and tested solar reactors/receivers for the melting of aluminium are based on the principle of rotary kilns [53, 54, 55]. Typically, the process employs a heliostat field to focus concentrated solar radiation to a point at which the rotary kiln is positioned. The kiln is either placed on a ramp, usually a solid mount with a plateau [55], or on a tower - with both options permitting a larger heliostat field than

if the kiln was on the same level as the heliostat field. The solar kiln and a proposed plateau layout are shown in Figure 10 [55].

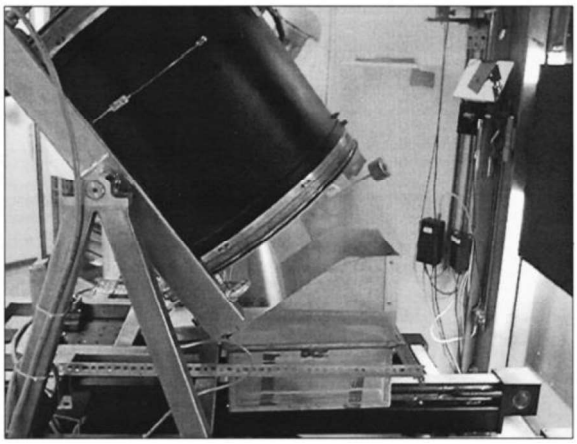

(a)

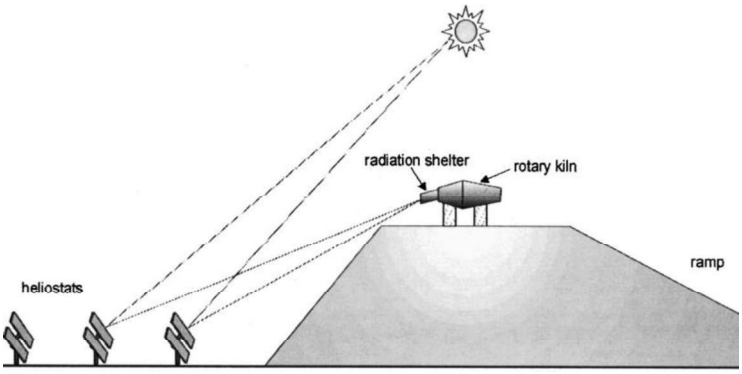

(b)

Figure 10. Aluminium melting using a solar-heated kiln with (a) the discharge of molten aluminium from a laboratory-scale kiln and (b) a proposed solar plant configuration [55].

The solar kiln operation closely mimics that of a conventional kiln that uses fossil-fuel burners to provide the process heat, with the main difference being the need for an open aperture for introducing solar radiation [55]. The aperture can be closed off with a quartz glass window, but this adds a layer of complexity to the design as the window needs to be cooled to prevent thermal shock and needs to be kept free of pollutants that might reduce the efficiency. The concentrated solar radiation enters the aperture, and due to the typical geometric configuration, it preferentially heats the upper part of the kiln cavity [55]. The surface of the bulk feed material is heated by reflected radiation and thermal emission from the overheated upper wall [55]. The rotation of the reactor/kiln ensures effective mixing of the feed material and added salts, used to

protect the molten aluminium bath against the oxidising atmosphere [55]. The rotation of the reactor not only aided in the effective mixing of the feed materials and additives but also aided in improving the heat transfer in the system [55]. The added salt mixture not only protects the molten bath but also aids in the separation of the aluminium and non-metallic compounds [55].

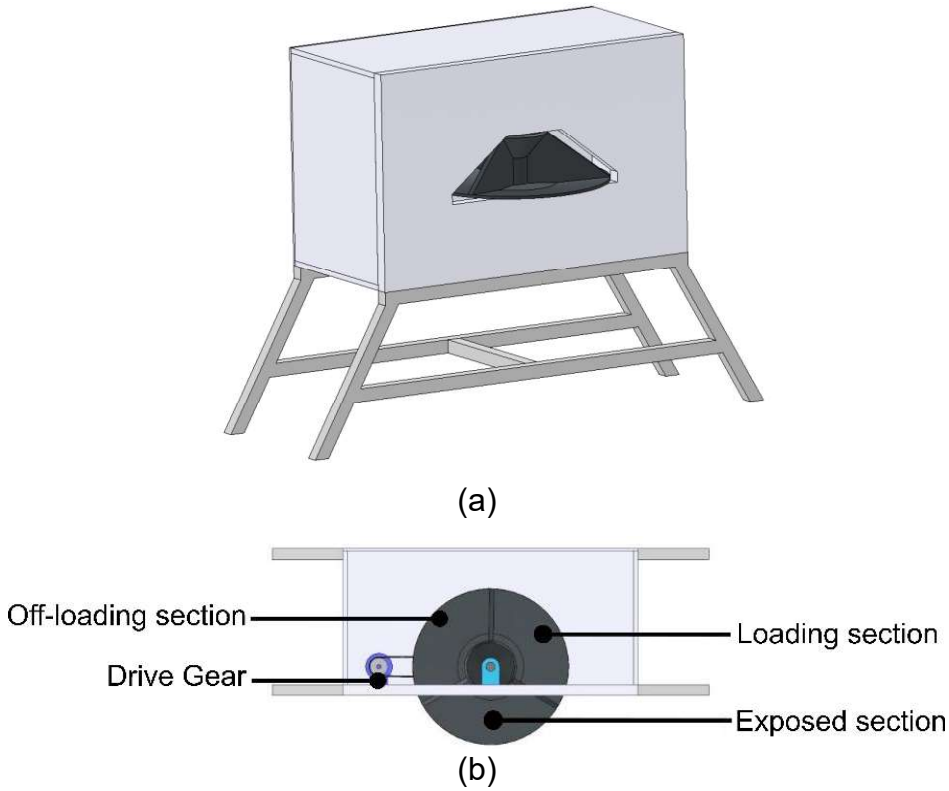

Figure 11. Rotor-type concept solar melting furnace arrangement with (a) showing an isometric view of the receiver and (b) the top view (figures redrawn from Ref. [58] *and adapted).*

For an industrial-scale solar kiln, a radiation shielding tube can be added to the aperture. This shielding tube helps to reduce radiation losses through the aperture while protecting the reactor cavity from climatic influences such as wind and moisture [55]. Puttkamer et al. [56] proposed a secondary concentrator at the aperture to improve the incident radiation while providing the same benefits as mentioned for the shielding tube [56]. The solar kiln process is operated using a batch feeding strategy, during which material is fed into the kiln, melted down, drained, and then repeated [53, 54]. Laboratory scale tests have revealed that it is possible to melt aluminium using solar-powered kilns operating at close to 1073 K [56]. No commercial-scale testing has been done, but simulation models for plant operations, making use

of an 8-ton capacity kiln, predict an overall plant efficiency of 52% and a maximum daily efficiency of 72% [57].

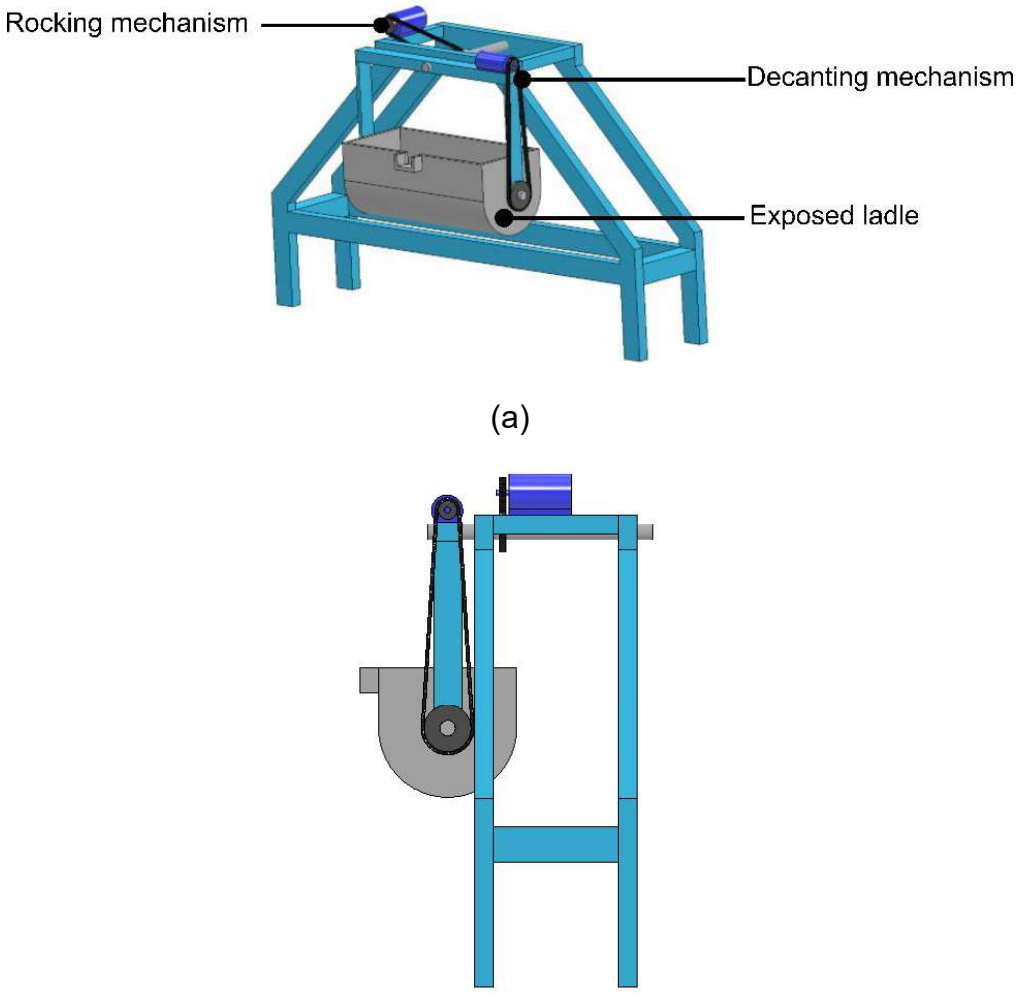

Figure 12. Ladle-concept solar melting furnace arrangement with (a) showing the isometric view of the receiver and (b) the side view (figures redrawn from Ref. [58] and adapted).

Aside from the solar-heated kiln, Abdurakhmanov et al. [58] proposed two other general arrangements that can be used for melting using a solar furnace as a heat source: a rotor type and a ladle type concept [58]. The rotor-type melting furnace arrangement refers to a rotating disk, divided into three sections. This arrangement allows one section to be exposed to solar radiation, and to maintain that position until the reaction is completed. The second section, positioned behind the protective screen, is being drained/unloaded while the third is being loaded and prepared, also behind the protective screen. The rotor assembly is water-cooled to protect it from the high heat input. Figure 11 [58] shows an example of such a rotor. The ladle-type

arrangement consists of positioning a ladle containing the process material at the focal point. This ladle is then directly heated to melt the process material. A rocking mechanism is added to the ladle to agitate the ladle and its content to ensure a homogenous state in the molten liquid [58]. Critical components of the ladle and the rocking mechanism are actively cooled to protect it from overheating and degradation. Once the content in the ladle is fully melted, it can be decanted and filled with a new batch. A schematic of the ladle arrangement is shown in Figure 12 [58].

2.4.3.2 Parabolic dish applications

Up to this point, all the high-temperature solar applications in literature made use of a heliostat field and central tower arrangement to generate the heat used for the process. This is due to the high concentration ratios and temperatures achievable at a stationary receiver. By keeping the receiver stationary, the design can be simplified. A parabolic dish is the other concentrating solar technology that can achieve similar temperatures and concentration ratios. The advantage of this technology is that comparable temperatures are achievable with a much smaller footprint, but the disadvantage is that the receiver has to track with the parabolic dish to remain at the focal point. By doing so, the receiver is exposed to dynamic forces, and the receiver design needs to account for the continuous change in orientation during the tracking cycle. The weight of the receiver is also limited by the dish structure design – more weight is associated with a more complex and costly structural design. The tracking actuators can, however, be used to position the receiver closer to ground level for access and maintenance purposes. This will allow the possibility of tipping and emptying the receiver using the actuation system.

At the time of doing this study, only one example of the use of a parabolic dish for the melting of medium-temperature metal could be found. Demitras and Özcan [29] investigated the thermal analysis of aluminium melting using a parabolic dish setup. In this study, the authors designed and tested a parabolic dish concentrator and an open-cavity conical receiver to investigate the direct melting of aluminium and lead samples [29]. The experimental setup is shown in Figure 13 (a) [29]. The parabolic dish design was optimised to meet the temperature requirements for melting aluminium under the climatic conditions of Trabzon in Turkey [29]. A 1.42-m-diameter parabolic dish was fabricated as a result, obtaining concentration ratios of up to 548 and an average focal temperature of 1023 K [29]. The authors chose a conical receiver

design based on their literature study, which showed that it would limit radiation heat losses [29]. A schematic of the conical, open-cavity receiver is shown in Figure 13 (b) [29]. However, limited information on the actual design of the receiver was provided. An overall system efficiency of 46% was attained and a total melting efficiency of 22% and 36% was attained for aluminium and lead, respectively [29].

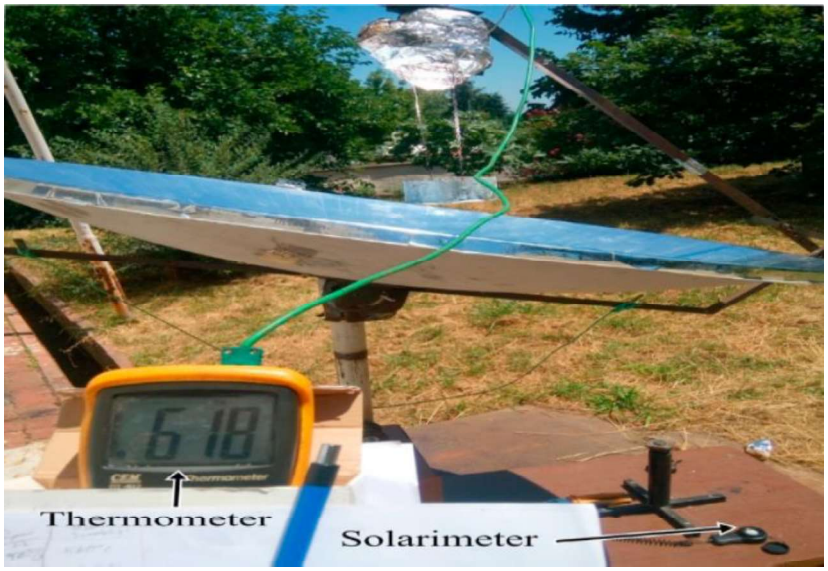

(a)

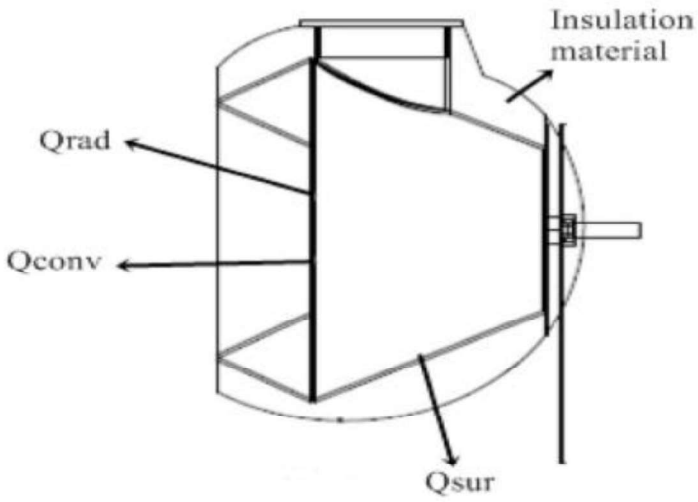

(b)

Figure 13. Parabolic dish and conical receiver for the melting of aluminium and lead showing (a) the general experimental setup and (b) the schematic of the conical receiver employed [29].

2.5 Solar parabolic dish system

To design and fabricate a receiver for melting zinc metal, a thorough understanding of the solar dish system and how the individual components affect each other is required. In this section, an investigation is launched into the different components that form part of a typical solar parabolic dish concentrator/receiver system and how each of these components influences the efficiency of the system. Some design considerations regarding each of these components will also be discussed.

2.5.1 Reflector/concentrator

The reflector, also known as the concentrator or collector, is the optical surface used to collect and concentrate incoming solar radiation. This can consist of a continuous, faceted, or mirrored surface arranged in a paraboloid [42]. A support structure maintains the parabolic surface to ensure optical accuracy and structural integrity under environmental influences [42]. The support structure is used to position the reflective surfaces and is used to support the receiver and the required tracking system.

2.5.2 Receiver

The receiver can be described as one of the most important components of any concentrated solar technology, as it is the receiver that converts the concentrated solar radiation to a useful form. All CSP receivers are designed to transfer the heat generated by the concentrated solar flux to a heat transfer medium of some kind. A wide range of receiver designs exists for both direct and indirect heating of the heat transfer medium, and this medium can consist of a gas, liquid, or solid [59]. Direct heating cycles have the advantage of reduced exergetic losses, while indirect heating enables the possibility of thermal storage [59]. When receiver design considerations are evaluated, each variable's impact on one another also needs to be considered. This sometimes results in a trade-off study to achieve the best possible outcome. An example of a trade-off is larger receiver apertures, which will be beneficial for solar absorption, but will increase heat losses as well as result in an increase in the cost of the receiver.

2.5.2.1 Receiver geometry and design considerations

Numerous studies on parabolic dish concentrator/receiver systems, both numerical and experimental, have been performed. Several authors [59, 60, 61, 62, 63, 64, 65,

66] set out to describe and define the optical performance of different cavity geometries, including conical, cylindrical, cylinder-conical, hemispherical, and cubical designs. In a recent review paper by Kasaeian et al. [68], a comprehensive summary of different cavity receiver geometries was discussed, drawing clear comparisons and conclusions on existing cavity receivers [68].

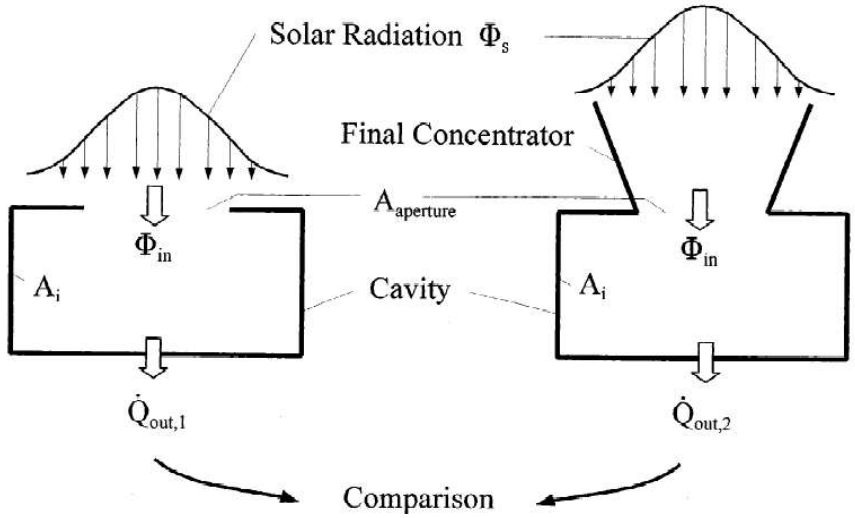

Figure 14. Comparison between a cavity without and a cavity with a concentrating cone [69].

The findings by Bellos et al. [62] and Kasaeian et al. [68] indicate that a cylindrical-conical cavity design generates some of the highest thermal and exergy efficiencies, followed by conical and cylindrical cavities. Typical solar cavity receiver designs are illustrated in Figure 15 [62]. Bellos et al. [62] predicted an optimum optical efficiency of 85.42% for cylindrical-conical cavities and 81.34% for cylindrical designs. These authors also estimated a thermal efficiency of about 68% for cylindrical-conical cavities at 300 °C and 60% for a cylindrical design [62]. Bellos et al. [62], Daabo et al. [63], and Kasaeian et al. [68] showed that there were thermal and optical efficiency differences between the different cavity designs but that it was relatively small in comparison, given the number of variables at play. When selecting a cavity receiver design, not only are the optical and thermal efficiencies important, but also the fabrication complexity and the associated cost. Small gains in the optical properties of the cavity receiver might not always justify a large increase in fabrication-related costs. Bellos et al. [62] and Kasaeian et al. [68] indicated that for rectangular, cylindrical, and conical cavities, the optimum cavity length is equal to the cavity aperture diameter [68] (for cavity receivers up to 350 °C [62]).

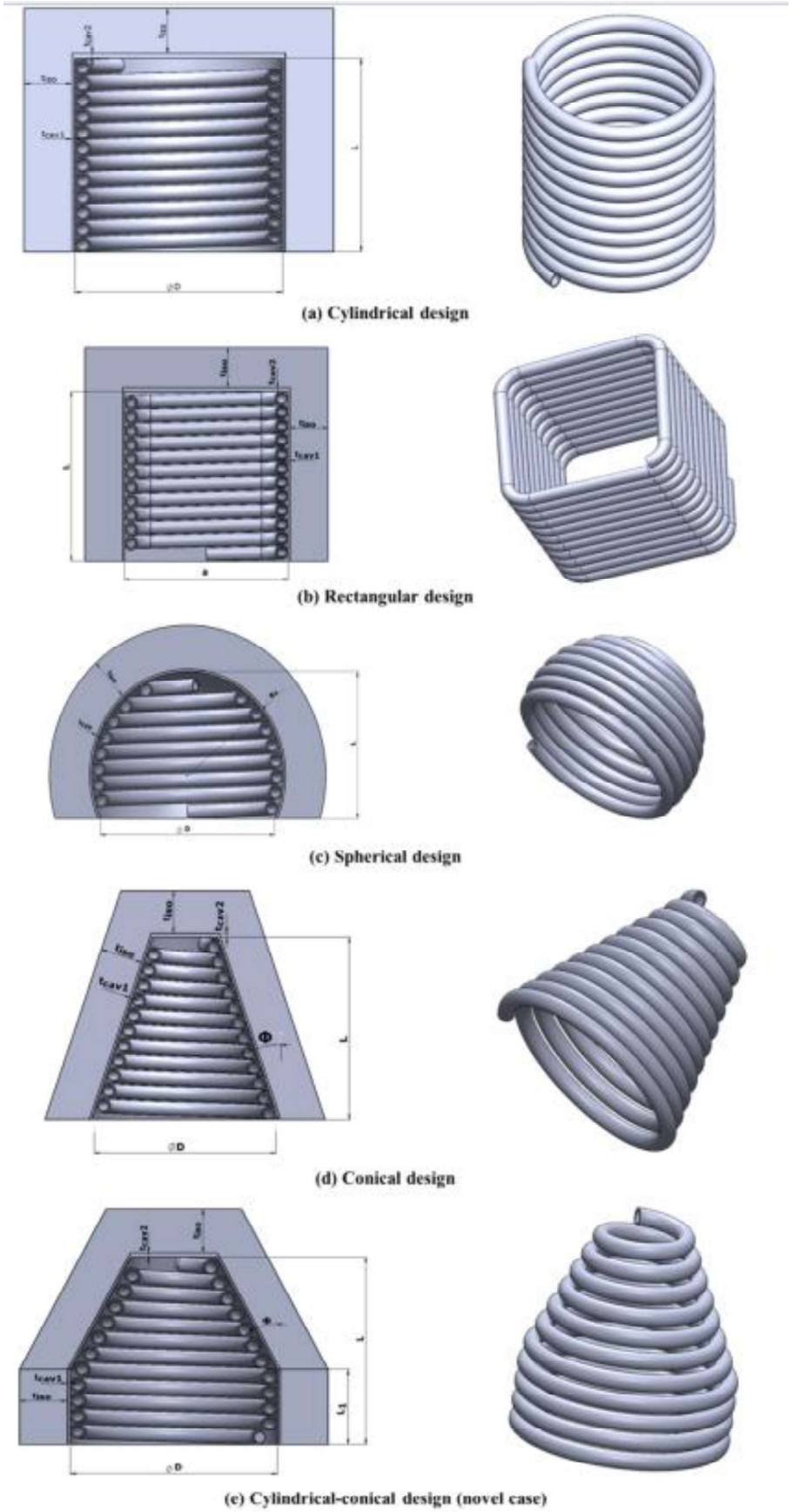

Figure 15. Typical solar cavity receiver designs [62].

Another design addition to be considered for open-cavity receivers is to use a concentrating cone on the cavity aperture [69], as shown in Figure 14 [69]. A simpler alternative to the addition of the concentrating cone is to make use of a modified cavity aperture [59, 69], as shown in Figure 16 [70]. By adding a plate to the receiver face with a smaller aperture than the cavity, a modified cavity is achieved, which then aids in reducing convection heat losses through a range of inclination angles. This design addition also marginally reduces radiation heat losses, which can become substantial at elevated temperatures [60]. This design change, unfortunately, results in a compromise between maximising solar radiation capture and minimising heat losses [71]. Lee et al. [72] have experimentally shown the influence of different aperture ratios (aperture diameter/cavity diameter) on heat losses from cavity receivers. The authors found an increase of 15 % in heat losses as the aperture ratio increased from 0.33 to 1 for a tilt angle of 30° and wind speeds of above 3 m/s [72]. This speaks to the need for considering these designs to limit heat losses from the cavity receiver.

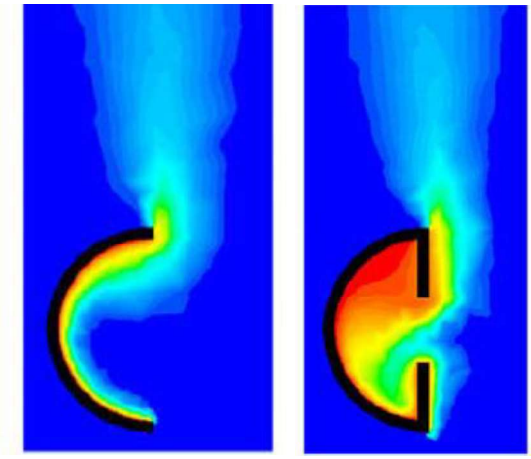

Figure 16. Temperature contours within a standard and modified hemispherical cavity [70].

2.5.2.2 Material of construction

When selecting a material of construction for a receiver, a wide range of variables need to be considered, ranging from thermal to optical properties. Wu et al. [73] proposed 304 stainless steel (SS304) as a suitable material for high-temperature solar receivers exposed to temperatures of up to 1050°C, based on the good optical and thermal properties of this material as well as it being a cost-effective material. The high silicon content of SS304, however, would make it highly vulnerable to chemical attack

and erosion by molten zinc [74], excluding it as a potential construction material for the current study.

With conventional materials of construction for cavity receivers, such as stainless steel, not being an option for the current study, an alternative approach was required. Given that the current study focuses on the containment of molten zinc, galvanising kettles where investigated. Due to the aggressive nature of liquid zinc towards steel, zinc kettles are usually made of low-carbon, low-silicon steel [73, 74, 75, 76]. An example of such a material is Armco Steel, with a material composition of 0.08 wt% C, 0.4 wt% Mn, 0.015 wt% P, 0.025 wt% S, and traces of Si [77]. Other steels used for zinc kettles are hot rolled, low carbon steels, such as SAE 1010 [76] and A1006 [74]. What all of these have in common is the low carbon and silicon content. A silicon content of lower than 0.01 wt% recommended [74]. Although low carbon, low silicon steels also experience erosion, it is to a much lesser degree. When molten zinc reacts with low-carbon steel, it creates an alloy that adheres to the steel surface, limiting erosion [75]. At temperatures below 470 °C, the alloying reaction produces a stable layer on the surface of the steel container, very similar to what is experienced on the surface of a galvanised product [75]. At temperatures greater than 470 °C, the surface alloy becomes non-adherent, allowing the molten zinc to come in contact with the container's surface, accelerating the erosion of the container [75]. A solution to the mentioned problem is to apply a ceramic coating to the steel container, but this again affects the thermal conductivity of the system and is an added expense [77].

2.5.2.3 Thermodynamic modelling of cavity receivers

The objective of any receiver design is to achieve the highest possible thermal efficiency, which loosely translates to a design that maximises solar absorptance and minimises heat losses. At elevated temperatures, the most common loss from a receiver is usually radiation heat loss, followed by convective heat loss, and the smallest fraction is accounted for by conductive heat loss [77, 78, 79]. Cavity receivers achieve high optical efficiencies by trapping incident solar radiation inside the cavity, and by doing so, the effective absorbance of the receiver increases [62].

The convection heat losses from a cavity receiver depend on variables such as the temperature inside the cavity, the receiver shape, the inclination angle of the receiver, the wind direction, the wind speed, and other design considerations such as the use

of a wind-shield. Given the complexity of convection heat losses from a cavity receiver, several authors have attempted to quantify these losses. Natural convection heat loss from cavity receivers is fairly well understood and backed by good experimental results as published by Taumoefolau et al. [81], Yazdanipour et al. [82], and Abbasi-Shavazi et al. [83]. Ma [84] found that forced convection as a result of high wind speeds, can be as high as three times the maximum level of natural convection. This finding highlighted the need to include forced convection heat losses when evaluating a receiver design that will be exposed to environmental conditions. Several authors [83, 84, 85, 86, 87] have considered the effect of wind speed on convection heat losses, but these authors only considered wind speed with no wind direction or wind speed with only two receiver orientations (vertical and horizontal). Under real conditions, the wind can come from various directions relative to the receiver aperture. Interestingly, Ma [84], Uzair et al. [89], and Reddy et al. [90] found that the highest convection heat loss was experienced during a side-on-wind. In contrast, Prakash et al. [87] and Jilte et al. [88] stated that the highest heat losses were experienced during a head-on-wind.

Limited studies have investigated the effect of wind speed together with wind yaw angle. Authors such as Lee et al. [91] and Wu et al. [71] have experimentally investigated the effect of wind speed and yaw angle on heat loss, but this was done at either lower temperatures than what the current study will achieve (the melting temperature of zinc) or only at selected receiver inclination angles. Reddy et al. [90] developed a numerical model for a range of receiver inclinations, wind speeds, and directions as well as for cavity temperatures of up to 600 °C.

2.6 Conclusion

At the time of writing, limited literature could be found on the melting of zinc metal using concentrated solar power, and no literature of experimental data demonstrating this concept. In order to contribute to this limited body of knowledge, a literature study was first conducted to identify opportunities and to make use of proven design considerations pertaining to other solar thermal applications. A detailed look into the material properties of zinc was completed, together with an overview of existing zinc melting and extraction processes. In literature, the remelting of zinc cathodes, produced during the hydro-metallurgical production of zinc, has been identified as a suitable application to apply CSP to a high-temperature industrial application. This melting process forms part of the last step in the Roast-Leach-Electrowin (RLE)

process, which is used to produce approximately 80% of the world's zinc output. This step is conventionally done by melting the zinc cathodes in induction furnaces, however, the operating temperature of 450 °C makes this a suitable candidate to apply a CSP technology. At the time of writing, South Africa had no active zinc-producing plants, making this application more favourable in the South African context by allowing this metal to be beneficiated locally using the country's excellent solar resource. Other zinc-related process applications such as the carbothermic roasting and distillation of zinc have also been discussed, but the higher operating temperatures required have earmarked these topics for future studies.

A brief investigation into solar thermal technologies confirmed that the selected solar thermal technology, a PDR, will be suitable for the intended study. Literature shows that PDRs not only achieve excellent optical and thermal efficiencies but also that their small footprint makes them ideal for unique solar thermal research projects. The small footprint and the use of cost-effective fabrication methods, enable PDRs to achieve thermal and optical properties similar to much larger systems such as HFRs. This allows PDRs to simulate environments that can be expected from much larger industrial CSP plants, but at a fraction of the cost and scale.

An in-depth investigation into alternative zinc-related solar thermal technologies was also done, with the aim of identifying lessons learned from other solar-zinc technologies. Most of the existing zinc-solar technologies are related to thermal or carbothermic reduction, not melting, but it still allowed for an insight into unique solar receiver designs. The most value was gained from investigating the limited available literature on the melting of other metals with low melting points in solar thermal applications. The literature demonstrated the benefit of having a rotating cavity receiver in that it aids in the mixing and heat transfer in the medium being heated. This design requirement was found in most of the solar receiver designs used for the thermal reduction of ZnO as well as in the aluminium melting application using a solar-heated kiln. The literature study also highlighted that a two-axis tracking solar thermal collector will be the only solar thermal technology that can provide sufficient heat for melting applications.

An exploration of literature pertaining to existing solar thermal receivers allowed for insight into suitable receiver geometries and possible design considerations aimed at

reducing heat losses from the system. From the literature, it could be concluded that cavity receivers are most commonly paired with PDR systems. Most high-efficiency systems rely on cavity receivers rather than alternative technologies such as flat plate receivers. It has been shown that cylindrical-conical cavity receivers achieve some of the highest optical and thermal efficiencies, followed by conical and cylindrical cavity receivers, for cavity temperatures up to 350° C. The literature study on cavity receivers also pointed out that cavity receivers with apertures equal to the cavity depth offer some of the best thermal performance.

Lastly, the literature review showed that limited literature is available on the thermodynamic modelling of solar thermal cavity receivers when considering environmental conditions such as wind. This is primarily a result of limited information being available on forced convection heat losses from cavity receivers, which consider factors such as wind speed and direction relative to the receiver aperture.

3. METHODOLOGY

3.1 Introduction

In this chapter, the details related to the experimental setup, experimental methodology, and analytical model developed as part of this work are discussed. The experimental set-up and analytical model aimed to demonstrate that small-scale processing of a low-melting-point metal is achievable using only CSP. This was done by showing that molten metal could be tapped from the experimental receiver design, and the recorded temperatures were used to validate the analytical model.

An experimental setup built around an existing multi-facet parabolic dish system is described, including the solar dish design, receiver design, data acquisition method, as well as the tracking system that was employed.

In support of the experimental work, and to support further development of this technology application, an analytical model was developed. A detailed overview of the theory on which the analytical model was based upon is provided, followed by an explanation of how this model was implemented. Lastly, the weather data used as input for the analytical model is discussed.

3.2 Experimental setup

To investigate the potential for melting zinc metal using CSP, an experimental setup was constructed to evaluate this concept under real environmental conditions. The experimental setup, which included a multi-facet dish assembly, a solar receiver, a drive system, a data logging system, and a tracking system, is shown in Figure 17.

The multi-facet modular dish is referred to as the solar dish. The solar dish consists of six reflective facets fitted to a facet mounting base, as shown in Figure 17. The solar receiver absorbed the concentrated solar radiation and housed the zinc metal inventory. The receiver was positioned at the focal point of the multi-faceted dish using four adjustable receiver arms. Using a drive system, the solar receiver was rotated to limit the possibility of hot spot formation inside the receiver and improve heat transfer and mixing of the zinc feedstock. The solar dish and receiver assembly were allowed to face the sun for the duration of the testing period by adjusting the tracking system in both the azimuth and elevation direction. The elevation tracking actuator and the azimuth tracking base were used for the solar tracking process. The receiver cavity temperature and the temperature of the zinc metal were remotely monitored, using the

remote data logger. These temperature measurements were also used as an indication as to when the zinc inventory was fully molten and could be tapped from the receiver. In the following sections, each of these individual sub-systems are discussed in greater detail.

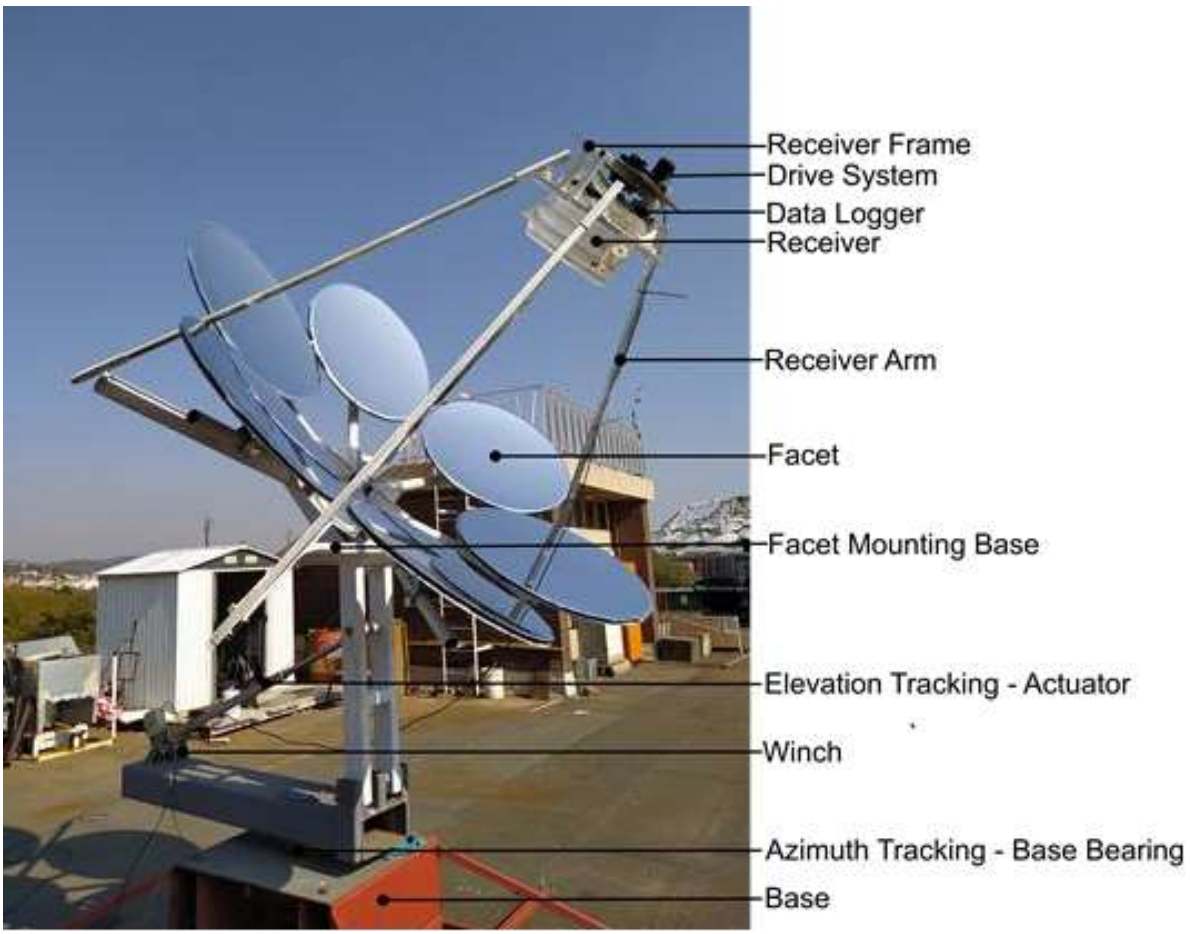

Figure 17. Experimental setup showing all the individual sub-components.

3.2.1 Solar dish design

An existing parabolic dish platform was used, developed and constructed at the University of Pretoria, with the design considerations outlined in the work by Roosendaal et al. [92] and Swanepoel et al. [93]. The solar dish was made up of six smaller mirror facets that worked independently to concentrate incoming solar radiation to a single focal point at which the receiver was positioned. Each mirror facet was constructed by stretching and sticking a sheet of EverBright mirror film [94] to the rim of an ordinary television satellite dish. This assembly method, together with a pneumatic valve fitted to the back of the satellite dish, allowed a vacuum to be drawn and maintained behind the membrane. By pulling a vacuum behind the membrane, the reflective surface of the membrane could be formed into a concave shape that

aided in focusing the collected solar radiation. Roosendaal et al. [92] and Swanepoel et al. [92, 94] provided a detailed description of how these facets can be constructed.

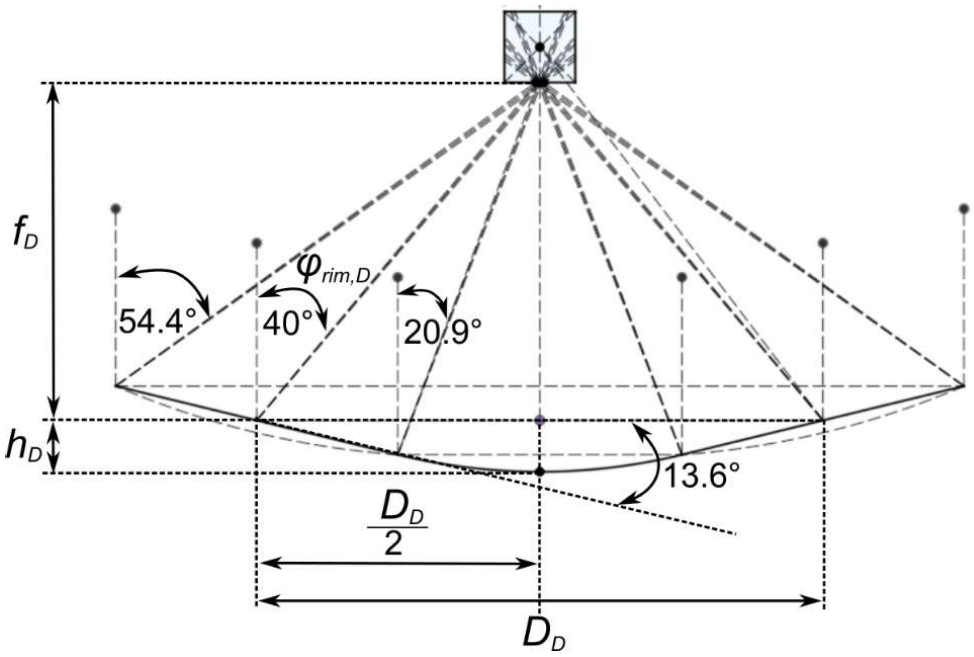

Figure 18. Geometric dimensioning of the multi-facet dish assembly.

The inner dimensions of each facet were measured to be 820 mm × 757.5 mm [92], resulting in an elliptical shape rather than a circle. Zanganeh et al. [96] have shown that this characteristic can be advantageous. By tilting the elliptically shaped facet to face the receiver, as done in the multi-facet design, a near circular image can be projected onto the receiver aperture [96]. Making use of elliptically shaped facets increases not only the intercept factor but also the concentration ratio of the assembly [96]. Each facet was tilted 13.6° upward from the horizontal plane to achieve the above-mentioned projection characteristic. A rim angle was selected based on the flux distribution achieved on the inside of the cavity wall (see Section 2.5 for the description of the solar receiver). An effective rim angle of 40°, as illustrated in Figure 18, allowed for sufficient penetration onto the receiver cavity while maintaining a relatively short focal length. As the focal length increases, the receiver arm (the structural steel section that supports the receiver) would also increase in length, resulting in the dish assembly becoming top-heavy or introducing unwanted movement at the receiver end during tracking. Each facet was positioned at $D_D/2$ = 0.8 m from the centroid of the global dish assembly, which resulted in an effective dish diameter, D_D, of 1.6 m. To ensure the predetermined geometric characteristics were met, a wooden template was fabricated to position each facet at the correct position and

orientation. The wooden template was cut to the correct length to identify the centroid between two facets, and a digital inclinometer was used to get the required facet tilt angle. The wooden template is shown in Figure 19. Once all the facets were installed, a water-cooled plate was positioned where the receiver aperture would be positioned and used for the final alignment and focusing of the individual mirror facets. The water-cooled plate used for calibration is shown in Figure 20, and the result of the successful calibration is visually demonstrated in Figure 21. A summary of the geometric characteristics of the multi-facet dish assembly is listed in

Table 5.

The EverBright mirror film's spectral reflectivity is 95% on average for all light wavelengths [93, 96]. Roosendaal et al. [92] determined the intercept factor for a similar multi-facet dish assembly using a novel lunar flux mapping method. They calculated an intercept factor of 89.9% for a 0.135 m × 0.135 m aperture. The results by Roosendaal et al. [92] were used to calculate the expected intercept factor for the larger 0.2 m aperture diameter used for this work. This calculation, based on the results obtained by Roosendaal et al. [92], verified by the water-cooled plate calibration work, allowed for an intercept factor of 100% to be assumed for the current test work.

Figure 19. Facet positioning method using a wooden template and digital inclinometer.

Figure 20. Facet calibration method using the water-cooled plate.

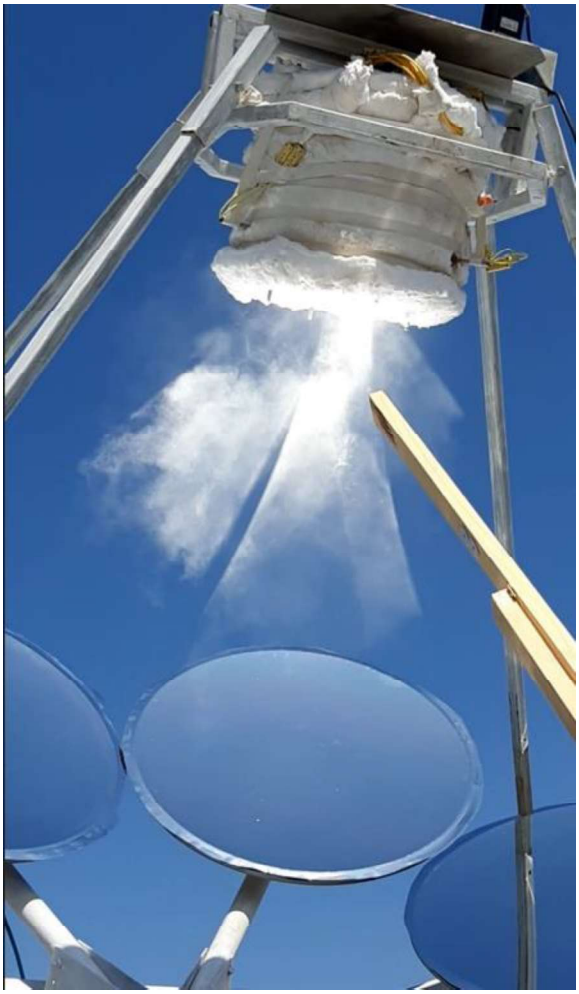

Figure 21. The concentration of incoming solar radiation is demonstrated by putting a wooden beam at the focal point.

Table 5. Geometric design characteristics of the multi-facet dish assembly.

Parameter	***Symbol***	***Unit***	***Value***
Global dish diameter	D_D	m	1.6
Global rim angle	$\varphi_{rim,D}$	degrees	40
Local focal length	f_D	m	1.098
Virtual dish depth	h_d	m	0.145
Total incident reflective area	A_D	m^2	2.845
Reflectivity	ρ_D	%	90
Intercept factor	Γ	%	100
Shading factor	f_s	-	1

3.2.2 Solar receiver material of construction

Considering the duration and nature of the test work to be conducted for the current study, standard structural steel was deemed a suitable material of construction for the solar receiver. Weldable structural mild steel, such as 350WA has a silicon content of less than half of what is specified for SS304 [98], making it a much better candidate. Not only does it have a favourable Si content, but it is also cost-effective and readily available.

Limited literature exists on the optical properties of mild steel due to the variability of the material composition of this type of generic steel, as well as inconsistent surface conditions. Sadiq et al. [99] mention that there is no consensus on the value of emissivity (ε) for structural steel in the steel construction industry. They also found that the emissivity of steel differs significantly depending on the temperature. Sadiq et al. [99], therefore, proposed a generic calculation for the emissivity of steel depending on the temperature. The emissivity of structural steel can be calculated as per Equation 9 [99].

$$\begin{aligned} \varepsilon &= 0.28, \quad For\ T < 380\ ℃ \\ \varepsilon &= 0.00293T - 0.833, \quad For\ 380\ ℃ \leq T < 520\ ℃ \\ \varepsilon &= 0.69, \quad For\ T \geq 520\ ℃ \end{aligned} \tag{9}$$

The absorptivity of a material is a function of surface roughness, incident radiation intensity, wavelength, and temperature. This, together with the range of material compositions available for structural mild steel, makes it difficult to get an exact value for solar absorption of this material. Sarkar et al. reference an absorptivity of 0.52 for mild steel [100] at a surface roughness of 1.05 μm (similar surface finish to cold rolled steel). This value was used for the current study.

3.2.3 Solar receiver design

The solar receiver comprised a primary receiver cavity, which was exposed to the concentrated solar radiation, and a secondary zinc cavity which housed the zinc metal inventory. The as-built receiver assembly is shown in Figure 22, and the receiver is shown in the installed state in Figure 23. A cylindrical cavity shape was selected for the receiver design based on good optical properties, as found by Kasaeian et al. [80] and Bellos et al. [62], and because this shape allowed for simple and cost-effective fabrication. The receiver cavity had an aperture opening of 200 mm in diameter and a cavity depth of 200 mm. The zinc cavity was radially 30 mm larger than the receiver cavity and this allowed for a zinc cavity volume of approximately 5.95 liters. Figure 24 illustrates all the relevant receiver design dimensions. The entire receiver assembly was fabricated from 350WA mild steel material, with the receiver vessel weighing approximately 6.7 kg, excluding the insulation material and instrumentation. The receiver cavity and zinc cavity were fully welded to one another and the back plate of the receiver was secured in place using a flanged arrangement and sealed using a high-temperature sodium silicate-based sealant. This allowed the back plate to be unbolted when the zinc cavity had to be inspected or when the cavity was to be charged with zinc feedstock.

The back plate housed a drive shaft that was secured in two flanged pillow blocks, allowing the receiver to rotate freely inside the receiver support frame, as shown in Figure 22. The receiver support frame was, in turn, secured to the receiver arms to position the receiver at the focal point of the solar dish, as shown in Figure 23. The drive shaft was fitted to a chain and sprocket assembly, with a gear ratio of 4:1, allowing the receiver to rotate at between 20 rpm and 42 rpm. The rotational system was driven by a NEMA 23 stepper motor, locally controlled from an Arduino Uno micro-controller board and a TB6600 stepper driver. Also fitted to the back plate was a

tapered steel plug, that was removed when the zinc inventory was fully molten, allowing the zinc metal to be drained from the zinc cavity.

A shield made from a 3 mm thick aluminium sheet was bolted in between the receiver support frame and pillow block bearing to serve as a radiation shield for the electronic equipment. This arrangement ensured that the electronic equipment fitted to the back of the receiver was always shielded and protected from direct solar radiation.

Figure 22. As-built receiver assembly installed in the receiver support frame.

Figure 23. Installed receiver fitted with insulation material and connected to the drive system.

To measure the receiver cavity wall temperature and the zinc temperature, four dual-junction K-type thermocouples were used. Each thermocouple probe was 6 mm in diameter and housed a thermocouple junction at the tip of the probe and a second, 30 mm back. This allowed for eight temperature measurements, from only four openings in the zinc cavity outer wall. The thermocouples were positioned using a brass compression fitting screwed into a ½ inch socket, which was welded to the outside of the zinc cavity as well as the back plate. Three probes were positioned 50 mm up from the receiver aperture and spaced 120° apart, and the last probe was fitted through the back plate, as shown in Figure 24. When the ports were drilled for the probes, a small divot was drilled into the outer face of the receiver cavity wall. This allowed the junction positioned at the tip of the probe to make good contact with the receiver cavity wall. The second junction was then positioned at the back of the zinc cavity and provided a temperature representative of the entire zinc volume. TC1 to TC4 represented the thermocouple junctions at the receiver cavity wall, and TC5 to TC8 represented the junctions at the back of the zinc cavity.

With the thermocouple probes secured in place and the back plate fitted, multiple layers of ceramic fibre blanket were used to cover and insulate the receiver. Two layers were fitted to the side as well as the back of the receiver, resulting in an insulation thickness of 50 mm in these areas. Only a single layer of 25-mm-thick insulation was applied to the face of the receiver body. The insulation was secured in place by a combination of mechanical fasteners and Scotch 27 glass cloth electrical tape. The receiver cavity was left as untreated mild steel, of which the optical properties were discussed in Section 3.2.2.

The total cost of the receiver came to approximately 9750 ZAR. This cost included the steelwork, insulation material, drive system, instrumentation required to drive the stepper motor, and temperature logging equipment.

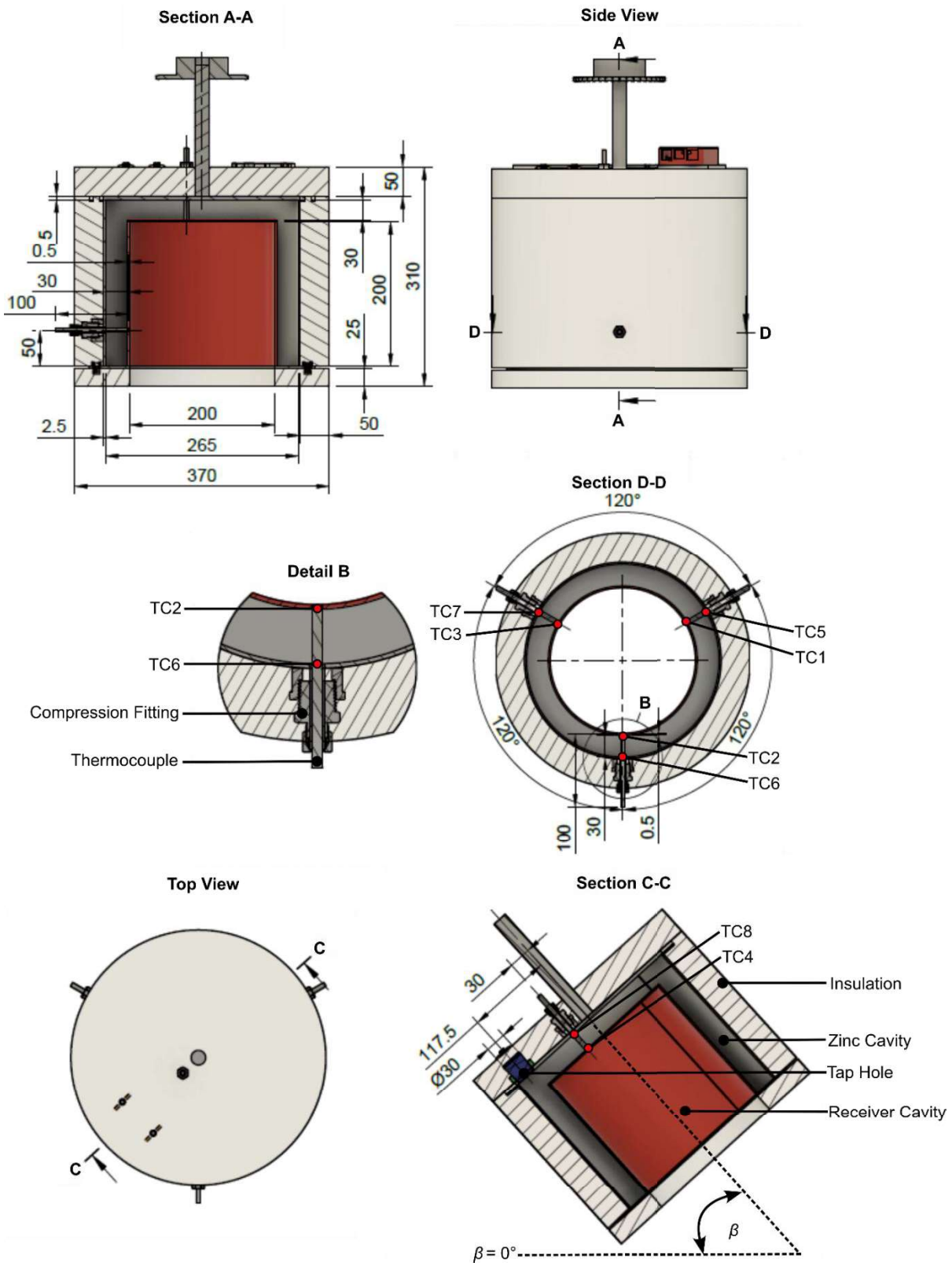

Figure 24. The receiver design showing the major dimensions and the thermocouple positions.

3.2.4 Data acquisition

By rotating the receiver cavity, additional complexity was added to the data logging system as no wire connections could be made to ground level as it would result in the cable being wound up around the drive system. For this reason, the entire temperature data logging system had to be mobile and rotate with the receiver. This was achieved by fitting a temperature data logging system to the back of the receiver. The data logging system consisted of a Raspberry Pi 3B single-board computer [101] fitted with two MCC134 thermocouple data acquisition (DAQ) hats (“hardware attached on top”) by Measurement Computing Corporation [102]. Each of the two MCC134 DAQ hats was capable of reading four thermocouples, resulting in the required eight temperature measurements. The single-board computer and the attached hardware were powered by a 20 000 mAh ADATA battery pack. The data logging system is shown in Figure 25.

All data collected were stored locally on the Raspberry Pi, but could also be viewed remotely using a Virtual Network Computing (VNC) connection over a local Wi-Fi network. This arrangement avoided the situation in which an internet connection failure could corrupt the data being collected but still allowed the operator remote access to the receiver temperatures. After the successful completion of an experimental test, the data could be downloaded from the Raspberry Pi for analysis. Each temperature channel was recorded on a 1-second interval to ensure high-resolution recordings of the temperatures in the receiver cavity and the zinc. These readings were saved, together with a time and date step, in a CSV (comma-separated values) file for post-processing of the data.

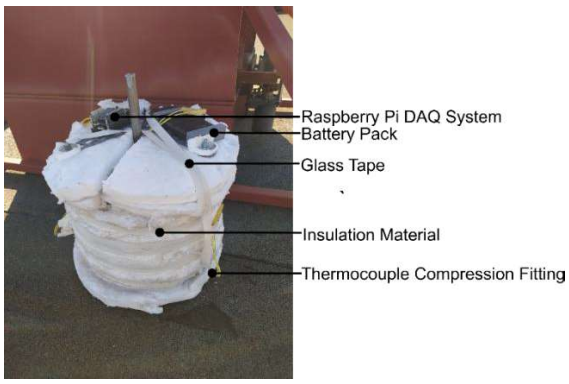

Figure 25. The data logging system is shown fitted to the back of the receiver.

3.2.5 Tracking system

To enable optimum solar radiation collection by the solar dish/collector, a two-axis tracking system was employed to ensure the dish was always directly facing the sun throughout the day. The dish could be adjusted in the azimuth axis and in elevation, with both axes being operated manually. To ensure the accuracy of the manual tracking method and to confirm that the tracking error remained within 1°, a pin-hole tracker was employed, as shown in Figure 26. A pin-hole tracker consists of a calculated length of tubing blanked off at the face pointing towards the sun, with a pin-hole in this face. A semi-transparent material with a target surface is positioned at the other end of the tubing. As long as the light shining through the pin-hole was kept within the target surface, a tracking error of less than 1° was maintained. A simple geometry calculation was used to calculate the length of the tube to be used and the diameter of the target surface. A 200 mm long section of 25 mm × 25 mm square tubing was used, and the length of the tubing resulted in a target surface with a diameter of 7 mm.

Figure 26. The pin-hole tracker showing a light spot within the 1° target.

3.3 Experimental method

The experimental setup was used to evaluate the solar collector and solar receiver system on five different days to gather information over a range of environmental conditions. For easier access to the receiver frame, the elevation drive linear actuator was disconnected, and a hand winch was used to tilt the dish assembly to ground level. Each experimental run began by filling the zinc cavity with solid zinc feedstock, as shown in Figure 27. Thereafter, the back plate was put in position and the zinc cavity was sealed close. The data logging equipment was then fitted to the back of the receiver before the receiver unit was installed into the receiver frame and the drive system connected.

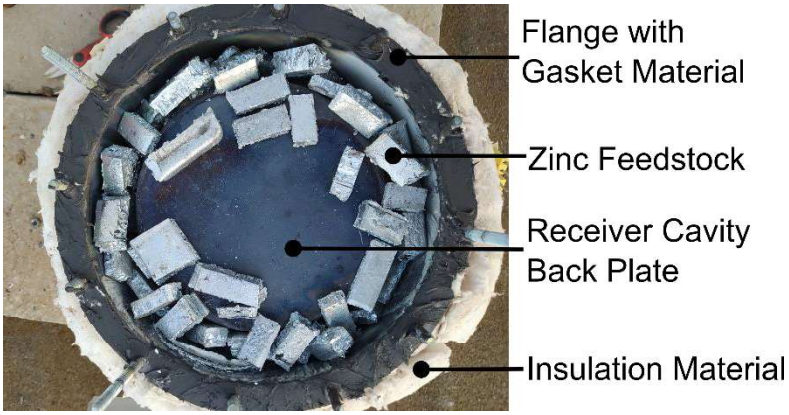

Figure 27. The zinc cavity before heating showing the zinc feedstock and gasket material used for sealing the back plate.

After the receiver had been installed, the hand winch was used to tilt back the assembly and re-connect the elevation drive. The tracking system, as well as the pin-hole tracker, were then used to get the solar dish to face the sun directly, allowing the sunlight to be focused into the centre of the receiver cavity. The vacuum behind each of the facet membranes was then drawn to concentrate the collected solar radiation to a smaller focal point into the receiver cavity. At this stage, the data logger was already busy recording temperatures and was remotely monitored on a laptop next to the experimental setup. The rotation of the receiver was also activated at this time. With all of the auxiliary systems in operation, the tracking system was continuously manually adjusted to keep the tracking error within 1°, using the pin-hole tracker as guidance. Once the temperatures of the thermocouples at the zinc cavity sidewall started to rise above 420 °C (the melting point of zinc), it was assumed that the zinc inventory was fully molten and that the latent heat phase had been completed. The rotation of the receiver was then stopped, and the assembly rotated to face opposite to the sun before the assembly was lowered to the tapping position. The same position and procedure used for loading the receiver were used to position the receiver for the tapping operation. The assembly in the receiver maintenance and tapping position is shown in Figure 28. The plug at the back of the receiver was then removed which allowed for the molten zinc to be drained into a steel ladle which was coated with a release agent to aid in releasing the ingot from the ladle afterwards.

The cast zinc ingot was allowed to cool in the ladle before it was removed for inspection. The receiver was also removed from the receiver frame to cool down separately and to allow access to the data logger to recover the locally stored data.

The same experimental procedure was repeated during each test. A step-by-step description of the experimental procedure is outlined in Appendix A

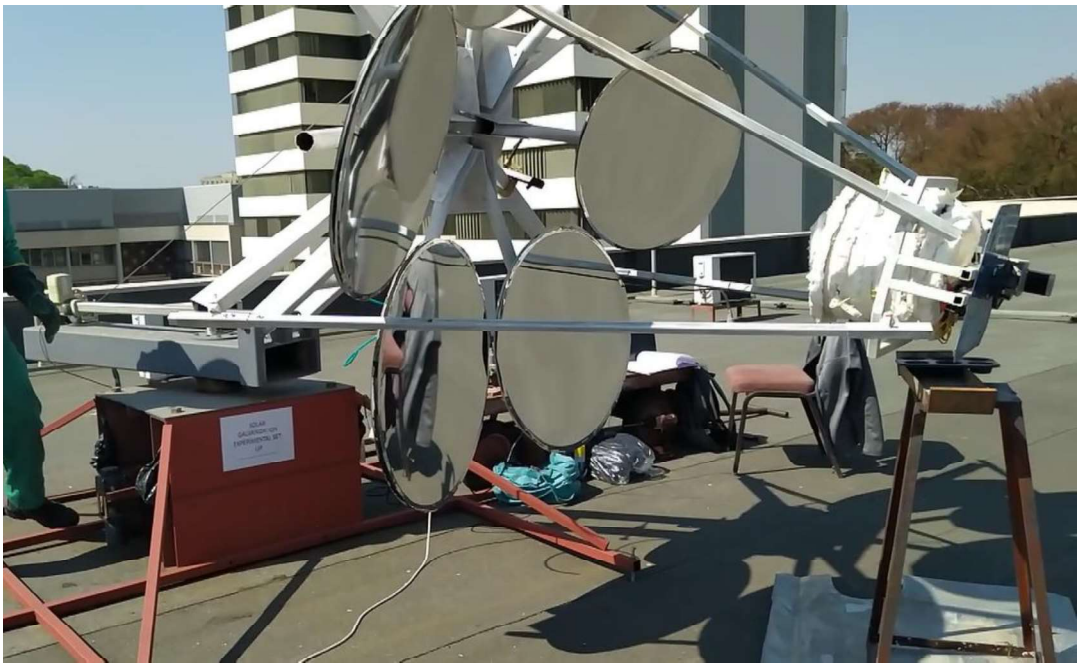

Figure 28. Receiver charging and discharging position with the whole assembly lowered to ground level for easier access.

3.4 Analytical model

An analytical model was developed in the Python programming language [103] to determine the efficiency of the proposed CSP system. This model considers the solar input, based on measured solar data, as well as the heat loss associated with the receiver design, orientational movement, and environmental conditions. The model results were then validated against the experimental results.

The model was used to calculate the first-law thermal efficiency (at each timestep) for the receiver ($\eta_{th,rec}$), as shown in Eq. 10.

$$\eta_{th,rec} = \frac{\dot{Q}_{net}}{\dot{Q}_{ap,in}} \tag{10}$$

Note that $\dot{Q}_{net}$ is the net thermal heat input rate to the zinc metal and $\dot{Q}_{ap,in}$ is the solar thermal input rate collected at the receiver aperture.

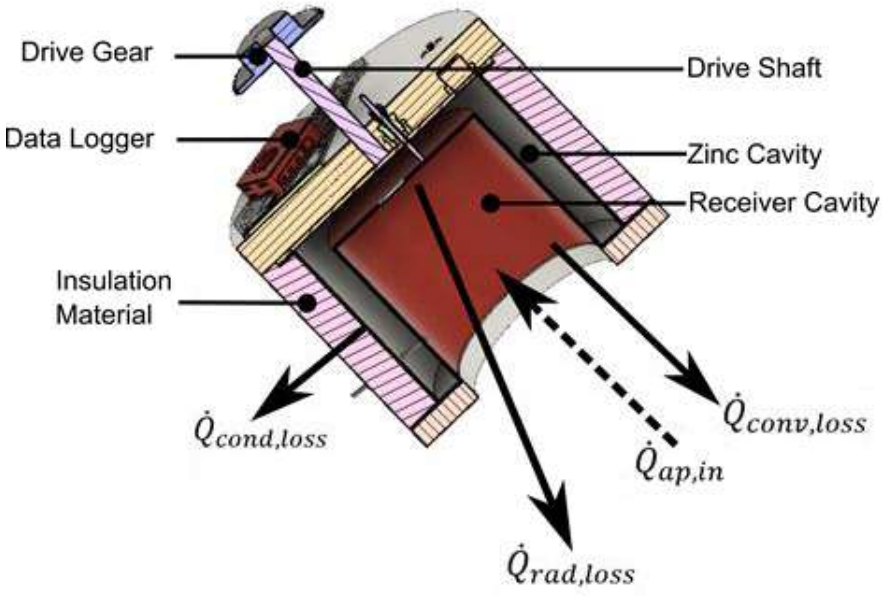

Figure 29. Schematic of heat loss mechanisms from the open-cavity receiver exposed to the environment.

A schematic of the receiver and the heat losses are shown in Figure 29. The heat loss from the receiver consists of conduction ($\dot{Q}_{cond,loss}$), convection ($\dot{Q}_{conv,loss}$), and radiation heat loss ($\dot{Q}_{rad,loss}$). The net heat transfer rate available in the zinc cavity was calculated using Eq.11. The constant, *c*, is the heat transfer efficiency constant that will be discussed in greater detail in the results section but was used to correct for the fill density in the zinc feedstock and for contact between the receiver wall and the zinc. The *c*-constant is therefore unique to the state of the zinc packing structure and will be experimentally determined. Air gaps in the zinc feedstock negatively affect the heat transfer between the receiver cavity wall and the zinc.

$$\dot{Q}_{net} = c \cdot \dot{Q}_{wall} = c \cdot (\dot{Q}_{ap,in} - (\dot{Q}_{cond,loss} + \dot{Q}_{conv,loss} + \dot{Q}_{rad,loss})) \quad (11)$$

The useful solar heat supplied at the receiver aperture is expressed in Eq. 12 [104]. This equation considers the DNI (I) reaching the solar reflector surface area (A_D) and the reflector efficiency (η_D).

$$\dot{Q}_{ap,in} = I \cdot A_D \cdot \eta_D \quad (12)$$

The reflector efficiency (η_D) shown in Eq. 13, depends on the geometry, manufacturing

process, imperfections, mirror soiling, reflector material, and optical properties of the reflector [104].

$$\eta_D = \Gamma \cdot f_s \cdot \rho_D \tag{13}$$

As illustrated in Figure 29, the fundamental heat loss components consist of convection and radiation heat loss through the cavity aperture and conduction heat loss from the receiver insulation. The solar radiation intercepted through the aperture is also shown. The individual heat loss components will be discussed in greater detail below.

3.4.1 Conduction heat loss

At elevated temperatures, conduction heat loss from the receiver walls represents a small fraction of the total receiver heat losses if sufficient insulation is applied [77, 104]. The insulation thickness is typically specified in such a manner as to limit the conductive heat losses while limiting the shading factor of the receiver. Because of the use of the multi-facet dish design, the shading factor was not of real concern and was specified as $f_s = 1$. For this receiver design, ceramic fibre blanket insulation material was selected to be used as receiver insulation based on the material's low thermal conductivity, flexibility, and availability. The ceramic fibre blanket has a thermal conductivity of 0.11 W/mK at 673 K [106]. The conduction heat loss from the receiver insulation was calculated as per Eq. 14, assuming that the average zinc temperature equals the average wall temperature.

$$\dot{Q}_{cond,loss} = \frac{\left(T_{Zn,ave} - T_\infty\right)}{R_{tot}} \tag{14}$$

As it could not be assumed that the outer surface of the insulation material would be at ambient temperature, natural and forced convection between the surface and ambient environment, needed to be incorporated into the conduction heat loss calculation. The combined thermal resistance (R_{tot}) of the cylindrical receiver system was calculated by Eq. 15, with R_{ins} and R_{conv} being the insulation and convection resistances, respectively [35].

$$R_{tot} = R_{ins} + R_{conv} = \frac{\ln\left(\frac{r_{o,ins}}{r_{i,ins}}\right)}{2\pi\, L_{rec}\, k_{ins}} + \frac{1}{2\pi r_{o,ins}\, L_{rec} h_o} \tag{15}$$

The convection heat transfer coefficient (h_o) represents a combination of natural and forced convection at the outer surface of the receiver insulation material. Forced convection will be dependent on the wind speed and angle of attack. Cross-flow over the receiver was assumed for all scenarios, and heat loss from the back of the receiver was neglected as it was fitted with an additional insulation layer and was shielded by a sun shield installed to protect the data logger. Conduction heat losses from the drive shaft were also neglected due to the relatively small area of this component. To determine the convection coefficient, the average Nusselt number ($Nu_{D,forc}$) for forced convection over a cylinder in a cross-flow wind was evaluated using Eq. 16 and 17 [35].

$$h_o = \frac{Nu_{D,forc}\, k_{ins}}{D_{ins}} \tag{16}$$

$$Nu_{D,forc} = \frac{h_0\, D_{ins}}{k_{ins}} = C\, Re_{D,ins}^{m} Pr^{1/3} \tag{17}$$

Constants C and m for cylinders in cross-flow used for Eq. 17 can be found in [35], based on the calculated Reynolds numbers ($Re_{D,ins}$).The Reynolds number ($Re_{D,ins}$) is defined by Eq. 18 [35].

$$Re_{D,ins} = \frac{\rho_{air}\, V_{wind} D_{ins}}{\mu_{air}} \tag{18}$$

The free/natural convection Nusselt number for a cylindrical body was calculated as per Eq. 19 [35], valid for $Ra_{D,ins} \leq 10^{12}$, where $Ra_{D,ins}$ is the Rayleigh number ($Ra_{D,ins} = Gr_L\, Pr$) and Pr the Prandtl number.

$$Nu_{D,nat} = \left(0.6 + \frac{0.387 Ra_{D,ins}^{\frac{1}{6}}}{\left(1 + \left(\frac{0.559}{Pr}\right)^{\frac{9}{16}}\right)^{\frac{8}{27}}} \right)^2 \tag{19}$$

To determine whether the natural and forced convection should be combined or either one to be neglected, the following checks were completed, as shown in Table 6.

Table 6. Check for combining free and forced convection [35].

Check	***Outcome***
$\frac{Gr_L}{Re_L^2} < 0.1$	Free convection is negligible
$\frac{Gr_L}{Re_L^2} > 10$	Forced convection is negligible
$0.1 \leq \frac{Gr_L}{Re_L^2} \leq 10$	Free and forced convection need to be combined

Note that the Grashof number was calculated using Eq. 20, with all the air properties calculated at the average temperature between the exposed insulation surface and the ambient conditions.

$$Gr_L = \frac{g\,\beta_v\left(T_{s,ins} - T_\infty\right)L_{rec}^3}{v_{air}^2} \tag{20}$$

To calculate the combined Nusselt number for the free and forced convection, Eq. 21 was employed with n equal to 4 for transverse flows involving cylindrical bodies [35].

$$Nu_D^n = Nu_{D,forc}^n + Nu_{D,nat}^n \tag{21}$$

3.4.2 Convection heat loss

The convection heat loss from the receiver's cavity was calculated as per Eq. 22, and the internal convection heat transfer coefficient, h_{in}, is shown in Eq. 23.

$$\dot{Q}_{conv,loss} = A_{cav}\,h_{in}\,(T_{cav} - T_\infty) \tag{22}$$

$$h_{in} = Nu\frac{k}{D_{ap}} \tag{23}$$

The Nusselt number (Nu) depended on the wind conditions and therefore, the wind

speed and direction determined whether or not natural convection, forced convection, or a combination of both occured inside the receiver cavity.

For wind speeds below 1.5 m/s, the Nusselt number for natural convection was calculated using an equation proposed by Stine and McDonald [84]. This equation is shown in Eq. 24, with $P(\theta)$ a function of the receiver tilt angle and l_c the characteristic length represented by the receiver aperture-cavity radius ratio [84].

$$Nu_{cav,nat} = 0.78\, P(\theta) l_c^{1.75} (Gr \cdot Pr)^{0.25} \tag{24}$$

To calculate the Nusselt number for natural convection for wind speeds between 1.5 m/s and 5 m/s, a correlation proposed Wu et al. [107] was considered and is shown in Eq. 25.

$$Nu_{cav,nat} = 0.00106 Gr^{0.149}\, (2 + cos\beta)^{7.228}\, (1 + \varepsilon_{cav})^{-0.0849} \left(\frac{d}{D_i}\right)^{1.466} \tag{25}$$

Concerning forced convection, a Nusselt number correlation proposed by Reddy et al. [90] was considered for all wind speeds below 5 m/s (see Eq. 26). β represents the receiver inclination angle (refer to Figure 24) and φ the incident angle of the wind, with 0° representing a side-on wind, 90° a head-on wind, and -90° a back-on wind, relative to the receiver aperture. The coefficients p, q, r, s, t were used in the calculation of the Nusselt number and are available from Ref [90]. The Grashof and Reynolds numbers were calculated using Eq. 27 and Eq. 28, respectively. It should be noted, however, that Reddy et al. [90] evaluated a modified hemispherical cavity receiver, whereas this study evaluated a cylindrical cavity receiver.

$$Nu_{cav,forc} = p(1 + cos\beta)^q\, (3 + sin\varphi + sin2\varphi + sin3\varphi)^r \left(\frac{d}{D_i}\right)^s \left(\frac{Gr}{Re^2}\right)^t \tag{26}$$

$$Gr = \frac{g\, \beta_v\, (T_{cav} - T_\infty)\, D_{ap}^3}{v_{air}^2} \tag{27}$$

$$Re = \frac{\rho_{air}\, V_{wind} D_{ap}}{\mu_{air}} \tag{28}$$

For wind speeds in excess of 5 m/s, equations proposed by Bergman et al. [35] were utilised for natural convection (see Eq. 29) and forced convection (see Eq. 30).

$$Nu_{cav,nat} = 0.52\ (Gr\ \cdot Pr)^{0.2} \tag{29}$$

$$Nu_{cav,forc} = 0.68\ Re^{0.5}\ Pr^{0.333} \tag{30}$$

The standard procedure for defining the convection state is by evaluating the $\left(\frac{Gr}{Re^2}\right)$ relationship, as shown in the conduction heat loss discussion. As the convection heat loss is calculated for a cavity, not cross-flow over a cylinder, this relationship won't be a precise estimation [35]. Ma [84] proposed simply adding the natural and forced convection together for the range of wind speed conditions but also noted that for head-on winds, this is probably incorrect and is done purely out of the convenience of a design correlation [84].

Given the uncertainty pertaining to forced and natural convection from within a cylindrical cavity, and in an attempt for a more accurate estimate as opposed to simply adding the forced and natural convection together as proposed by Ma [84], it was decided to use the $\left(\frac{Gr}{Re^2}\right)$ relationship for defining the convection state. This method was described in detail in the conduction heat loss section above and summarised in Table 6.

All air properties were calculated based on the bulk mean temperature (T_{bulk}) as shown in Eq. 31. An average cavity wall temperature was assumed for the cavity, which was also employed by the Nusselt number correlations [89, 106]. In the model, the cavity wall temperature is assumed to be the same as the zinc temperature $(T_{Zn,ave})$.

$$T_{bulk} = \frac{T_\infty + T_{Zn,ave}}{2} \tag{31}$$

3.4.3 Radiation heat loss

At elevated temperatures, radiation heat loss contributes a significant fraction of the total heat losses from the receiver [77, 85]. As opposed to the other two heat loss

mechanisms, radiation heat loss remains relatively constant throughout the day once a steady-state temperature has been reached inside the receiver [78]. The total radiation heat loss from a receiver cavity is the result of emission and reflection from the inside of the cavity [77, 85, 103].

Radiation heat loss due to emission ($\dot{Q}_{rad,em}$) from inside the cavity was calculated as per Eq. 32 [104], with ε_{eff} the effective emissivity based on the cavity emissivity (ε_{cav}) and the aperture surface area (A_{ap}) to cavity surface area (A_{cav}) ratio, as calculated in Eq. 33. The cavity emissivity (ε_{cav}) is a function of temperature as shown in Eq. 34 [99].

$$\dot{Q}_{rad,em} = \varepsilon_{eff}\, \sigma\, A_{ap}\, (T_{cav}^4 - T_{\infty}^4) \tag{32}$$

$$\varepsilon_{eff} = \frac{\varepsilon_{cav}}{1 - (1 - \varepsilon_{cav})\left(1 - \frac{A_{ap}}{A_{cav}}\right)} \tag{33}$$

$$\begin{gathered} \varepsilon_{cav} = 0.28, \text{for } T < 380°C; \\ \varepsilon_{cav} = 0.00293T - 0.833, \text{for } 380\ °C\ \leq T < 520\ °C; \\ \varepsilon_{cav} = 0.69, \text{for } T\ \geq 520\ °C \end{gathered} \tag{34}$$

To calculate the radiation heat loss as a result of reflection ($\dot{Q}_{rad,ref}$) from inside the receiver, through the aperture, Eq. 35 was used. With α_{eff} the effective absorptance, calculated as per Eq. 36 [104], and $\dot{Q}_{ap,in}$ the total energy supplied to the receiver aperture. The cavity absorptance (α_{cav}) for this study was assumed to be 0.52 [100].

$$\dot{Q}_{rad,ref} = \left(1 - \alpha_{eff}\right)\dot{Q}_{ap,in} \tag{35}$$

$$\alpha_{eff} = \frac{\alpha_{cav}}{1 - (1 - \alpha_{cav})\left(1 - \frac{A_{ap}}{A_{cav}}\right)} \tag{36}$$

The total radiation heat loss ($\dot{Q}_{rad,loss}$) from the receiver was calculated as the sum of the radiation losses as a result of emitted and reflected radiation as per Eq. 37.

$$\dot{Q}_{rad,loss} = \dot{Q}_{rad,em} + \dot{Q}_{rad,ref} \tag{37}$$

3.4.4 Heat gain calculation

With the heat input and all the heat losses accounted for, the heat gain of the zinc metal inventory could be calculated to determine at what time step the zinc inventory would be fully molten. This was achieved by using three stages, starting with the sensible heating stage, during which the full batch is still solid, followed by a transition phase known as the latent phase, as well as a second sensible heating phase during which the molten material (liquid) was heated further. During the liquid heating phase, the zinc material was heated beyond the melting point to aid in the successful tapping of the material from the receiver.

During the solid heating phase, Eq. 38 applies [35]. T_{t-1} represents the temperature of the zinc batch at the beginning of the time step (Δt = 1 minute), and was used together with the available heat (Q_{net}), to calculate the zinc cavity temperature at the end of the time step. This process was repeated until the melting point of zinc was reached. During the solid heating phase, both the zinc batch mass and the mass of the receiver steel were considered. To incorporate the mass of both the zinc and receiver, an average of the resultant specific heat capacity (c_p) was calculated at the system temperature for each time step.

$$\dot{Q}_{net} = (m_{zn} + m_{steel}) \cdot \frac{(c_{p_{solid-Zn}} + c_{p_{steel}})}{2} \cdot (T_t - T_{t-1})/60 \tag{38}$$

Once the melting point is reached, the latent heating phase, represented by Eq. 39 [35], comes into effect. This makes use of the latent heat of fusion (λ_{zn}) to calculate the amount of heat added to the zinc material. For every time step in this phase, Eq. 40 was in effect during which the mass of zinc that was already molten ($m_{zn,liquid(t-1)}$) was added to the mass of molten material formed during that time step. This was repeated until the entire batch of zinc was in the liquid state. For the latent heating phase, only the mass of the zinc batch was considered, as the steel temperature should show little to no temperature change during this phase.

$$\frac{\lambda_{zn}}{60} = \frac{\dot{Q}_{net}}{m_{zn}} \tag{39}$$

$$m_{zn,liquid(t)} = m_{zn,liquid(t-1)} + \left(\frac{60 \cdot \dot{Q}_{net}}{\lambda_{zn}}\right) \quad (40)$$

With the entire batch of zinc in the liquid state, the liquid heating took place as per Eq. 41 [35]. This process continued until a specified cut-off temperature was reached. An additional 20 K was added to the zinc melting temperature before it was removed from the heat source to be tapped. This was aimed at limiting the amount of zinc inventory that solidifies in the receiver during the tapping procedure as a result of heat losses. During the liquid heating phase, the mass of both the zinc batch and the receiver steel was again considered, as both would require energy to increase in temperature.

$$\dot{Q}_{net} = (m_{zn} + m_{steel}) \cdot \frac{(c_{p_{liquid-zn}} + c_{p_{steel}})}{2} \cdot (T_t - T_{t-1})/60 \quad (41)$$

3.5 Python computational model

A Python code, as described in Appendix B, was developed to consider historic weather data and predict the possible number of molten zinc batches that could be produced in any specified period, be it weekly, monthly, or annually. The Python code was based on the literature discussed in Section 3.4 and considered conductive, convective, and radiation heat losses from the cavity receiver. These heat losses were used to calculate the system's heat gain or heat loss to determine the time it took to melt down a batch of zinc.

3.6 Weather data

Accurate weather data was required to evaluate the performance of the solar collector and solar receiver, as well as to serve as inputs for the analytical model. This data was collected and provided by a Tier 1 SAURAN (South African Universities Radiometric Network) [108] weather station, positioned on the roof of Engineering Building 1 at the University of Pretoria. The Direct Normal Irradiance (DNI) measurement, used as solar irradiance input for all calculations, was measured by a Kipp & Zonen CHP1 pyrheliometer, positioned on a SOLYS solar tracker. A Campbell Scientific CS215 sensor was used to measure the atmospheric temperature and relative humidity, and an R.M. Young 05103-5 sensor was used to measure the wind speed and direction. All of these devices form part of the weather station at the University of Pretoria. It

should be noted that this weather station was not positioned directly next to the experimental setup, which resulted in some discrepancies between the measured and actual wind speeds. The weather station was positioned approximately 60 m away from the experimental setup and approximately 20 m higher. Wind speed data collected during a previous experiment [93] was obtained (Swanepoel, J.K., private communication, 2023) and used to evaluate the difference in wind speed between the experimental setup and the weather station. The wind speed data of seven days were evaluated, showing that wind speeds were about 5% higher at the experimental setup than what was measured at the weather station; however, this difference was assumed to be negligible. It was also found that the dominant wind direction was the same between the two measurement points.

In order for the data file generated by the weather station to be used as input to the Python model, some preparation work was required. This included classifying the wind direction into the categories as dictated by the analytical model. The data file was also evaluated for invalid or unrealistic data and corrected where necessary. A detailed description of the method used to prepare the SAURAN weather file, to be used as input for the Python model, is described in Appendix C.

3.7 Conclusion

In this chapter, the experimental and analytical methods for evaluating and demonstrating the remelting of zinc, using only concentrated solar power, were discussed. The experimental setup was discussed together with the design considerations and characteristics related to the multi-facet parabolic dish and the cylindrical cavity receiver. These sections provided information on how the multi-facet dish was assembled and calibrated and how the cavity receiver was charged and mounted to the dish assembly. The method and position of temperature data collection were also discussed.

The section on the analytical model outlined the different heat loss mechanisms and how each contributed to the net heat input in the solar thermal system. This analytical model was used to develop a computational model, in the Python programming language, which can be used to further develop this unique field of study. This computational model was based on the theory outlined in the analytical model section and made use of historical weather data to predict how many molten batches of zinc

are achievable in a given day. This computational model was validated using the experimental data collected as part of this study, and the results of this validation process will be discussed in the next chapter.

The weather data collected from the SAURAN weather station, situated at the University of Pretoria, had to be adapted to be in a usable format for the computational model. The method used, as well as the reasoning behind it, was discussed.

4. RESULTS

4.1 Introduction

Five separate experimental runs were executed to evaluate the potential for using CSP as a heat source to melt zinc metal and validate the analytical model. Each of these experimental runs had unique environmental conditions, allowing for a robust data set against which the analytical model could be validated. Appendix D highlights some of the differences between the five experimental tests. Detailed discussions describe the lessons learned and conclusions drawn from each experimental run. The results produced by the analytical model are included in this section, together with a detailed description of how the analytical model compares with the experimental results. A discussion follows on the efficiency of the system and the influence of the various environmental conditions. Each of the five experimental tests was executed as per the experimental method discussed in the previous chapter.

4.2 Experimental results

The first experimental run started at 13:36 on the 26th of July 2022. The late start resulted in the DNI already starting to steadily decrease, as shown in Figure 30, which ultimately resulted in the zinc not reaching the melting temperature of 420 °C. An average DNI of 688 W/m² and wind speed of 2.01 m/s was recorded during Experiment 1. TC6 and TC7 represent the thermocouples inside the zinc material, as illustrated in Figure 24. TC8 represents the temperature of the zinc cavity at the back of the receiver. As the zinc feedstock settles to the front of the receiver due to gravity and receiver orientation, it can be assumed that TC8 represents the air pocket temperature inside the zinc cavity. This is likely why TC8 measures lower temperatures in all the experiments because it is not in constant contact with zinc metal. TC2 to TC4 represent the temperatures of the receiver cavity, and the position of each is shown in Figure 24. TC1 and TC5 were found to be faulty and assumed to have been damaged during installation. The irregular noise in the measurement in TC4 is also most likely due to a damaged thermocouple, as it does not follow any of the other trends. The missing data around the 1-hour mark resulted from a data logger failure, but after a restart, the data logging continued. The same receiver was used for Experiments 1 to 4, and a new receiver was used for Experiment 5. This resulted in some interesting findings, which will be discussed below.

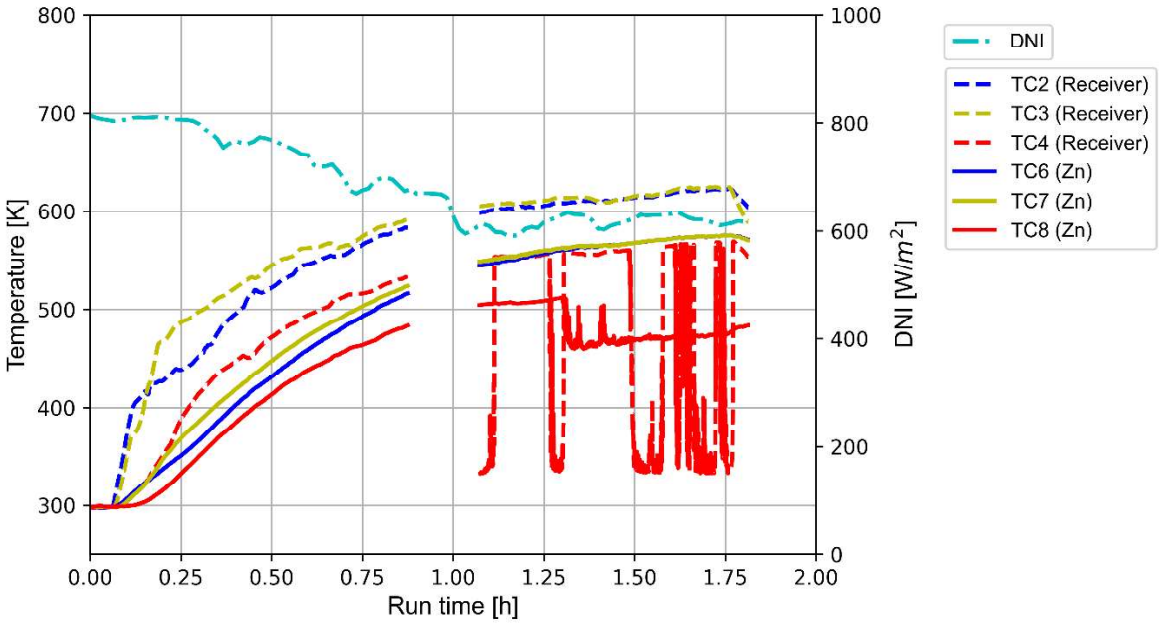

Figure 30. Receiver temperatures - Experiment 1 on the 26th of July 2022

Experiment 2 started at 10:12 on the 8th of August 2022 and made use of the same receiver and inventory as Experiment 1. A better average DNI of 792 W/m² was recorded together with a slightly higher average wind speed of 2.68 m/s, when compared to Experiment 1. It can be noticed that the receiver cavity temperatures (TC2 to TC4) sharply increased while the zinc temperatures (TC6 to TC8) increased more slowly, as shown in Figure 31. As the zinc temperature approaches the melting temperature, the receiver and zinc temperature get closer to one another, as expected, due to material softening and settling around the thermocouples and allowing for better heat transfer from the receiver cavity to the zinc. The limited deviation between the receiver temperature measurements points to a uniform receiver cavity temperature, which translates to the uniform heating of the zinc inventory. The control philosophy was to heat the receiver until temperature measurements above the melting point of zinc were observed, pointing to the latent heat phase being completed and the zinc inventory being fully molten. This was not completely the case as will be shown in the analytical model results discussion.

During Experiments 1 and 2, the face of the receiver was not protected with insulation material, resulting in excess heat loss. Not only did the exposed face result in a higher heat input required to melt the zinc feedstock, but the enlarged exposed surface and the resultant increased heat losses could also cause the molten material to solidify

again before it could be drained from the receiver. The increased heat loss, together with the time taken during the tapping procedure due to initial inexperience, is most likely why only 30.52% of the zinc inventory could be drained from the receiver in the molten form, as listed in Table 7. The increased heat loss was accounted for in the analytical model by adding additional convection heat loss from the faceplate of the receiver, as shown in Eq. 42. The additional convection heat loss was calculated in the same manner as described in Section 3.2, with the exception of the gravitational constant which was calculated as per Eq. 43 [35] to account for the buoyancy of the air in the Grashof number. The ratio between the surface area of the faceplate and the circumference of the faceplate represents the characteristic length used for the faceplate calculations.

$$\dot{Q}_{conv,loss} = (A_{cav}\, h_{in}\, (T_{cav} - T_{\infty})) + (A_{faceplate}\, h_{faceplate}\, (T_{cav} - T_{\infty})) \tag{42}$$

$$g_{faceplate} = g\cos(90° - \beta)\,, for\ 0° \leq 90° - \beta \leq 60°$$
$$g_{faceplate} = g, for\ 90° - \beta > 60° \tag{43}$$

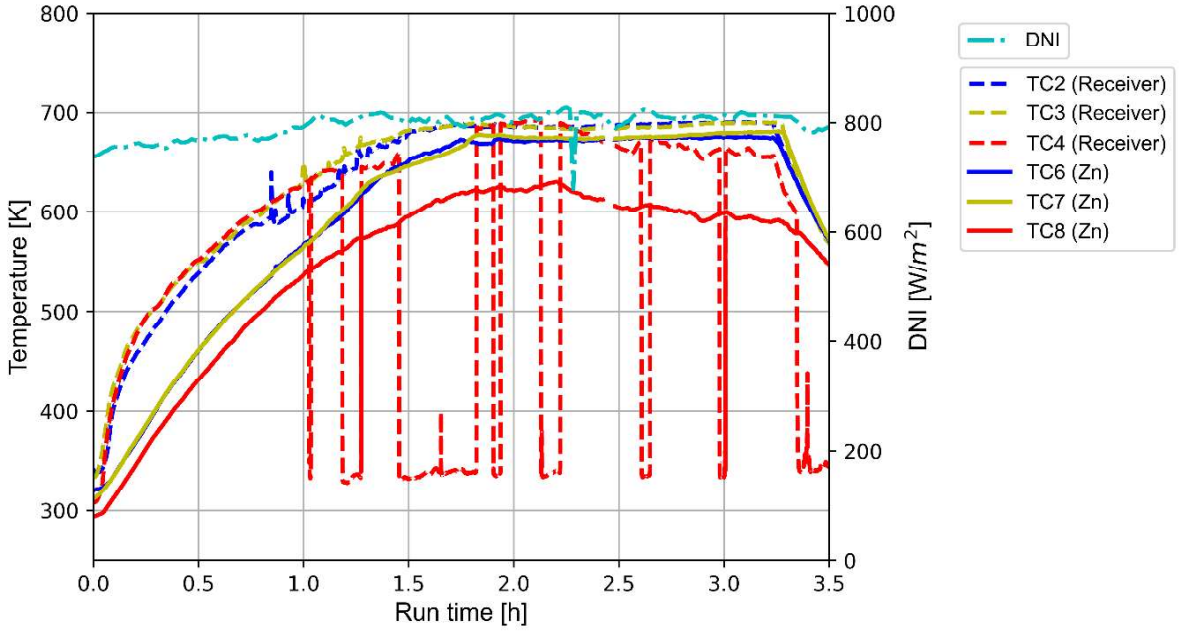

Figure 31. Receiver temperatures - Experiment 2 on the 4th of August 2022

Table 7. Molten zinc recovery by mass

Test	***Zinc mass [kg]***	***Mass drained [kg]***	***Mass remaining [kg]***	***Recovery [%]***
1	10.01	0	10.01	0
2	10.01	3.05	6.95	30.52
3	16.96	12.46	4.50	73.47
4	14.52	10.25	4.24	70.82
5	10.01	2.52	7.54	25.04

For Experiment 3, starting at 09:21 on the 16th of August, additional insulation was added to the face plate of the receiver, as illustrated in Figure 24 and Figure 29, with the aim of reducing the heat loss from this area of the receiver. During Experiment 3 the highest average DNI of 910 W/m², out of the 5 experiments, were recorded and an average wind speed of 2.14 m/s. The results of Experiment 3 are shown in Figure 32. It is assumed that the remaining inventory from Experiment 2 settled and solidified around the thermocouples towards the face side of the receiver. This assumption is based on a visual inspection of when the new zinc feedstock was added and the comparable temperatures between the receiver cavity temperatures and that of the zinc inventory, pointing to fewer voids in the feedstock. This improved the heat transfer significantly and reduced the heat input required to get the inventory to the molten state. The reduced heat loss from the receiver and the improved heat transfer between the receiver cavity and the zinc resulted in a steady and uniform heat-up of the complete system. TC4 follows the same trend at the beginning, pointing to a uniformly heated cavity, but then starts to malfunction around the half an hour mark. TC8 is likely not in contact with any process material and is, as a result, only measuring the air pocket temperature in the back of the zinc cavity. The uniform heat-up and stopping the experiment at the correct time to drain the molten inventory resulted in 73.47% of the zinc inventory being drained from the receiver in its molten state. The inventory that was not drained is believed to be a result of the high thermal conductivity of zinc and the time it took to drain the inventory, causing some material to solidify in the receiver, as all other indications pointed to the complete inventory being melted down.

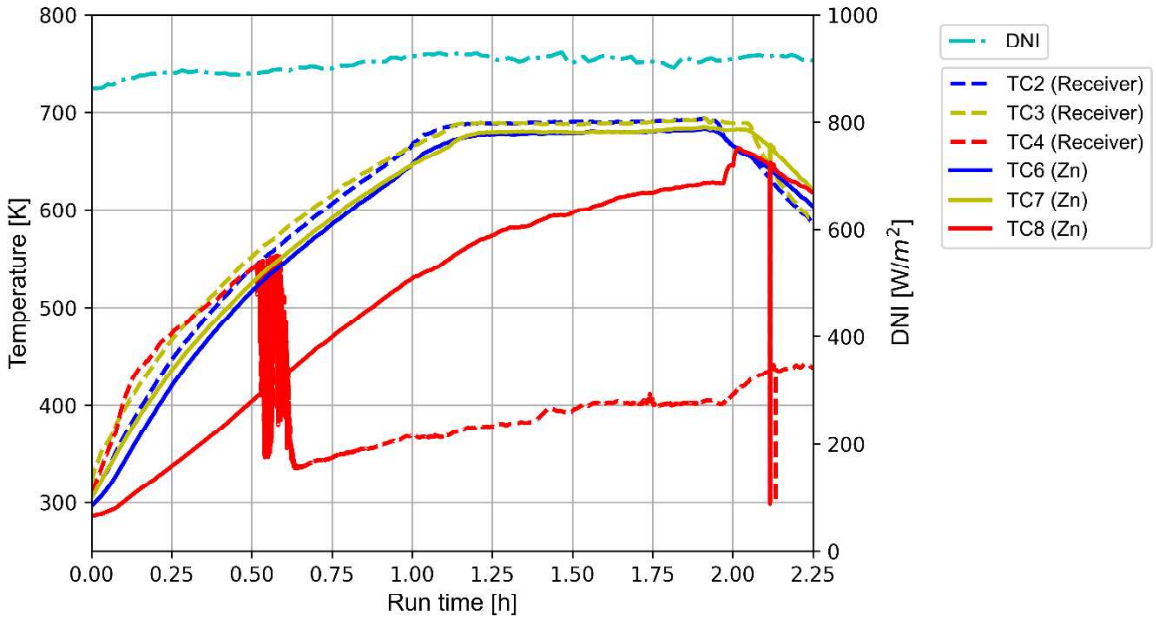

Figure 32. Receiver temperatures - Experiment 3 on the 16th of August 2022

Experiment 4 started at 09:11 on the 21st of August 2022, containing some solidified inventory from Experiment 3, but a visual inspection revealed that the material from Experiment 3 was drained to below the thermocouple position. Additional zinc feedstock was added to the receiver, adding voids in the inventory, and this is most likely why a significant temperature difference between the receiver cavity temperature and zinc temperatures is noticed, as shown in Figure 33. Even though good average solar irradiance was recorded on this day (908 W/m²), similar to Experiment 3, much higher average wind speeds (5.26 m/s) were recorded which drastically increased heat loss from the receiver. The impact of the wind speed will be discussed in greater detail in the analytical model results section. The higher heat loss resulted in less zinc being tapped from the receiver (70.82 %) even though this receiver was kept at the focal point of the parabolic dish for about 30 minutes longer than during Experiment 3. TC4 is believed to have completely malfunctioned during this experiment; therefore, the results are not reflected in Figure 33. TC 8 is again believed not to have been in contact with any process material.

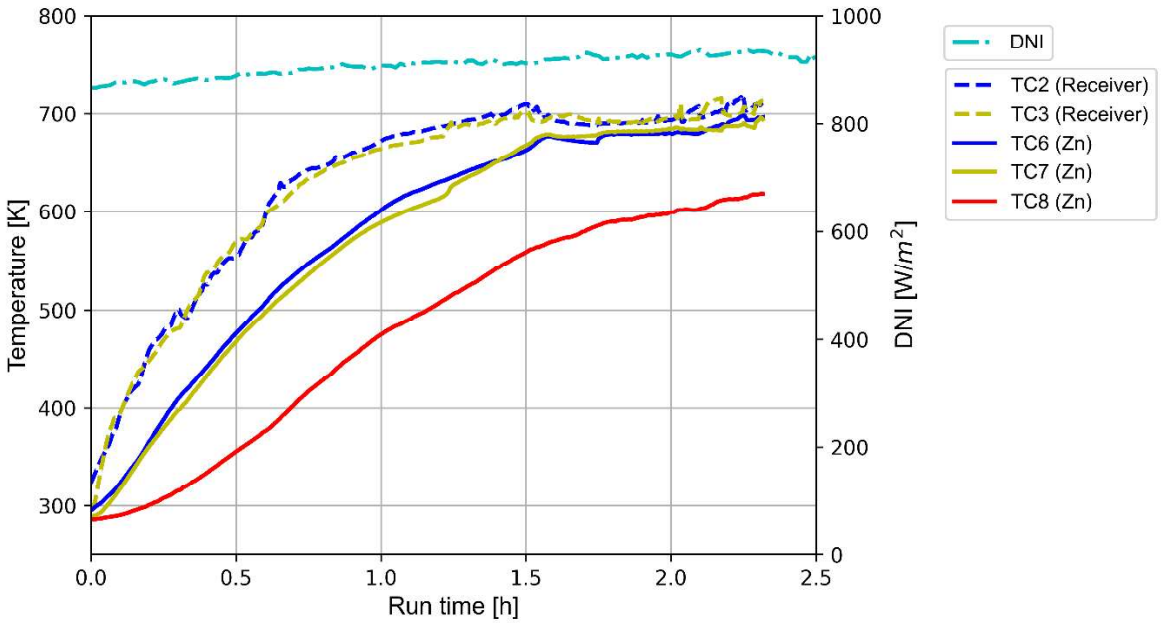

Figure 33. Receiver temperatures - Experiment 4 on the 21st of August 2022

The last experiment, Experiment 5, took place on the 5th of September 2022, and the test was initiated at 08:36. This test made use of a new receiver vessel with a fresh batch of zinc feedstock. This entailed a completely new fabricated receiver fitted with new insulation material and a new set of thermocouples. An average DNI of 835 W/m² was recorded together with the lowest average wind speed, out of the 5 experiments, of 0.95 m/s. Similar trends to Experiment 1 were noticed and are shown in Figure 34. All eight thermocouples were functional and pointed to uniform heating in the zinc feedstock, even though the receiver cavity temperatures did point to some irregularities. This can result from how and where the zinc feedstock made contact with the receiver cavity wall, utilising heat more efficiently at some positions and less at others, resulting in localised heating. Localised heating around 2.4 hours into the test (of thermocouple TC2) resulted in the zinc inventory being drained prematurely and only 25.04% of the inventory being recovered from the receiver in the molten form. This was a result of the experimental procedure, which dictated that if temperatures above 720 K were recorded after the latent heating phase, the molten material had to be tapped from the receiver.

During this experiment, there were also some operational issues with the multi-facet dish, during which three of the facets started to lose vacuum, which resulted in these facets losing their focal point. These facets had to be replaced during the test. At

20 minutes into the test, the first facet started to show signs of a leak, followed by a second around the 40-minute mark. An attempt was made to repair the leaking facets in situ, using silicone to repair the leak in the seal, and then attempting to re-draw the vacuum. But in failing to repair them, the two facets were replaced with new facets after an hour and 15 minutes. This was done while the tracking of the remaining (focussed) facets was still active, which continued to provide heat input to the receiver. It took roughly 5 minutes to replace the leaking facets with new facets, after which the experiment proceeded as normal. A third started to leak around an hour and a half into the test and was replaced with a new facet just before the two-hour mark. The test was then completed without any leaking facets. Whenever one of the facets lost its vacuum, the test could continue with the remaining facets, as it was only the heat input that was reduced, which the predictive model could account for. In the analytical model results section, more detail will be provided on how the reduced heat input was accounted for by the analytical model. This also demonstrates the method used to allow the predictive model to still accurately predict the zinc temperature, even though heat concentration capacity was lost halfway through the experiment, and regained towards the end. The leaking facets reduced the intercept factor, but by accurately recording the time at which a facet started to leak and when it was replaced, these changes could be accounted for and the analytical model could still be used to predict the zinc temperature.

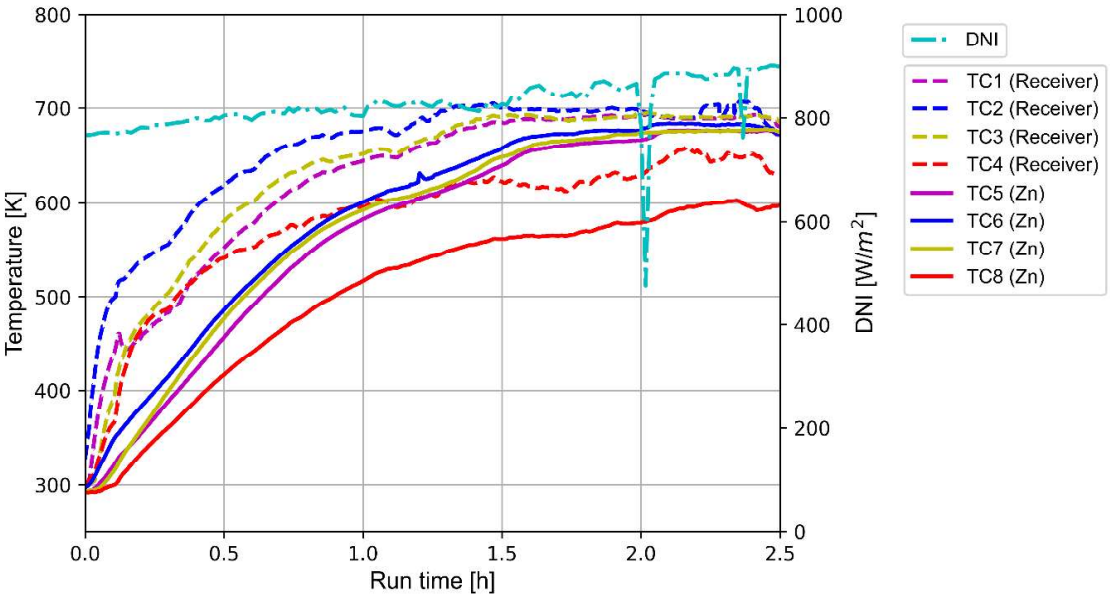

Figure 34. Receiver temperatures - Experiment 5 on the 5th of September 2022

Figure 35 shows the typical product obtained from the experimental process. The zinc was tapped into a rectangular ladle as well as into a cupcake mould for a more manageable form factor. No metallurgical comparison was done between the different tapped samples, but a similar viscosity was observed based on the good liquid flow achieved during each tap and the liquid metal being able to conform to the ladles it was tapped into. The rectangular ingot, shown in Figure 35, was later recycled by cutting it into smaller chunks using an industrial guillotine.

Figure 35. Cast zinc ingots

4.3 Analytical model results

One of the key deliverables of this study was the development of an analytical model that could be used to further investigate the potential for using CSP as a heat source for processing metals with a low melting point. To achieve this outcome, the model relies on historical weather data to predict the number of molten zinc batches that can be produced within a specified time. This model can be used as a tool to determine the feasibility and throughput of this CSP technology application. A Python model that was developed, based on the literature discussed in the analytical model section, calculates the heat balance based on the optical and design properties of both the receiver and the parabolic dish collector. The heat balance is based on the solar irradiance, ambient temperature, receiver orientation, wind speed, and wind angle that is obtained from the historical weather data.

The results from the analytical model were compared to the experimental results, not only to validate the model but also to refine user input assumptions made during the development of the model. In an attempt to account for the uncertainty related to the heat transfer between the solid zinc particles as well as between the receiver wall and zinc particles, a heat transfer efficiency constant, *c*, was included in the model. This heat transfer efficiency constant will be unique to each test run as no packing structures will be the same in how and where the zinc feedstock makes contact internally and with the cavity wall.

The results obtained from the analytical model were compared to the experimental results, and are shown in Figure 36 to Figure 40. One of the first observations made is that the zinc melted at temperatures slightly lower than the theoretical melting point (approximately 10 °C lower), and this is observed in all the experiments where the melting point had been reached (Figure 37 to Figure 40). This discrepancy is most likely due to the measurement resolution of the thermocouples used ($\pm\ 2\ °C$) together with material impurities in the zinc that resulted in a slightly lower melting point.

In Figure 36, the results for the first experiment are shown together with the output of the analytical model using the historical weather data for the test duration. The first experimental run served as a training exercise and the face of the receiver cavity was exposed to environmental conditions. The exposed surface and low DNI, coupled with a fresh batch of zinc, resulted in a slow increase in temperature and a significant

temperature lag between the receiver cavity and the zinc. The temperature difference between the receiver and the zinc is believed to be a result of the voids within the solid zinc feedstock that result in less-than-ideal heat transfer. The feedstock size also limits the volume of zinc material that fits in the zinc cavity – in this instance, only 47% of the zinc cavity was occupied by zinc material, with the rest taken up by air voids. The predictive analytical model assumes complete surface contact between the receiver cavity wall and the zinc feedstock, with no voids in the feedstock if c = 1. In order to match the predictive model to the zinc temperatures obtained in Experiment 1, a heat transfer efficiency constant of c = 0.5 was required.

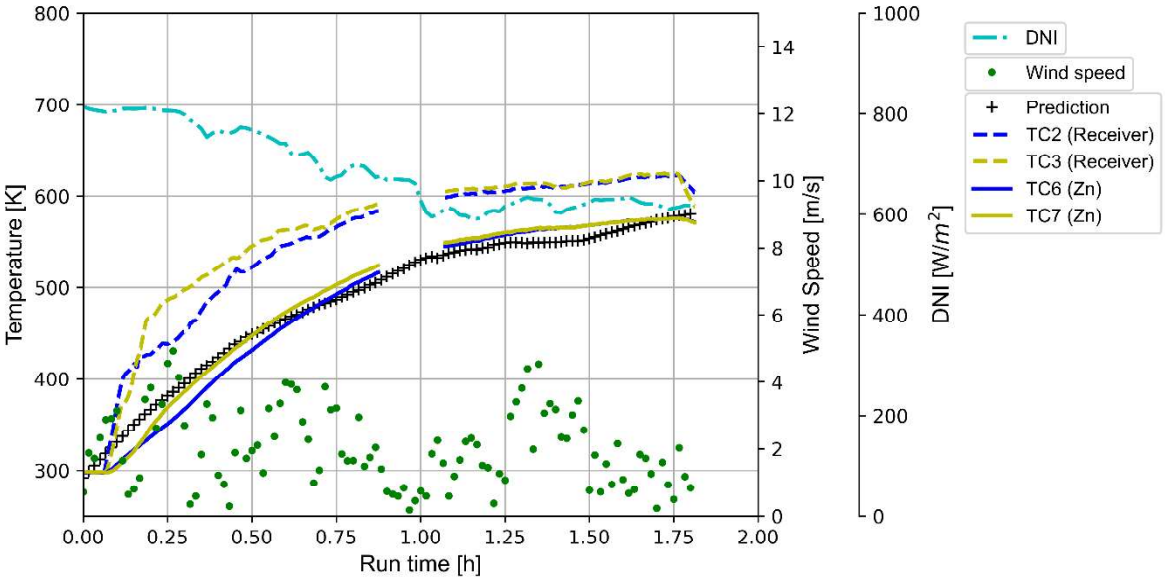

Figure 36. Experiment 1 compared to the analytical model prediction based on historical weather data.

Experiment 2 is compared to the analytical model in Figure 37. This experiment was executed using the same inventory left over from Experiment 1 and the same receiver setup, with the main difference being the environmental conditions. Experiment 2 was started much earlier during the day, and as a result, the receiver was exposed to much higher DNI intensities. The position of the sun was also different from Experiment 1, resulting in a lower receiver tilt angle, ensuring more movement in the zinc feedstock and potentially improving heat transfer. All of the differences to Experiment 1 are outlined in Appendix D. As with Experiment 1, a significant discrepancy between the receiver temperature and that of the zinc is noticed until the melting temperature of zinc is reached. The melting material ensures sufficient contact with the receiver cavity

wall, and as a result, the temperatures merge. This phenomenon is expected due to an improved heat transfer as the air voids between the zinc particles are reduced and better surface contact is made with the heated surface. In order to match the experimental zinc temperature to that of the predictive model, a heat transfer efficiency constant of $c = 0.4$ was required. The lower heat transfer efficiency constant than what was required for Experiment 1 can also result from user error in calibrating the mirror facets and the much higher wind speeds observed during this experiment. The higher wind speeds could exaggerate the heat losses from the receiver due to the exposed receiver face. The analytical model also provides insight into why only 30.5% of the zinc feedstock was tapped in the molten form. As demonstrated by the analytical model results, the latent heating phase had not been completed yet, and the receiver was drained prematurely during the experiment. If the latent phase had finished, an increase in the temperature would have been noticeable in the model curve (see Figure 38, for example). It can be observed that Experiment 2 took much longer to achieve melting temperatures when compared to Experiment 3 (Figure 38) and Experiment 4 (Figure 39), and that is with about 40% less inventory than what was used in Experiments 3 and 4 (as highlighted in Table 7). The reason for the longer melting time is likely due to a combination of factors. These factors include increased heat losses, due to the exposed receiver face, lower solar irradiance on the day, and weaker internal heat transfer due to the lower inventory volumes.

The premature tapping was only noted and validated during the analysis of the historical weather data and comparing the predictive model to the experimental results. It was prematurely tapped mainly due to operator error, as the original experimental procedure dictated that the metal should be tapped as soon as temperatures above the melting point of zinc were recorded. Only after the lessons learned from Experiment 2, was the experimental procedure adjusted to allow for some additional heating before tapping. This procedural change resulted in much higher molten metal recoveries in the following experimental runs.

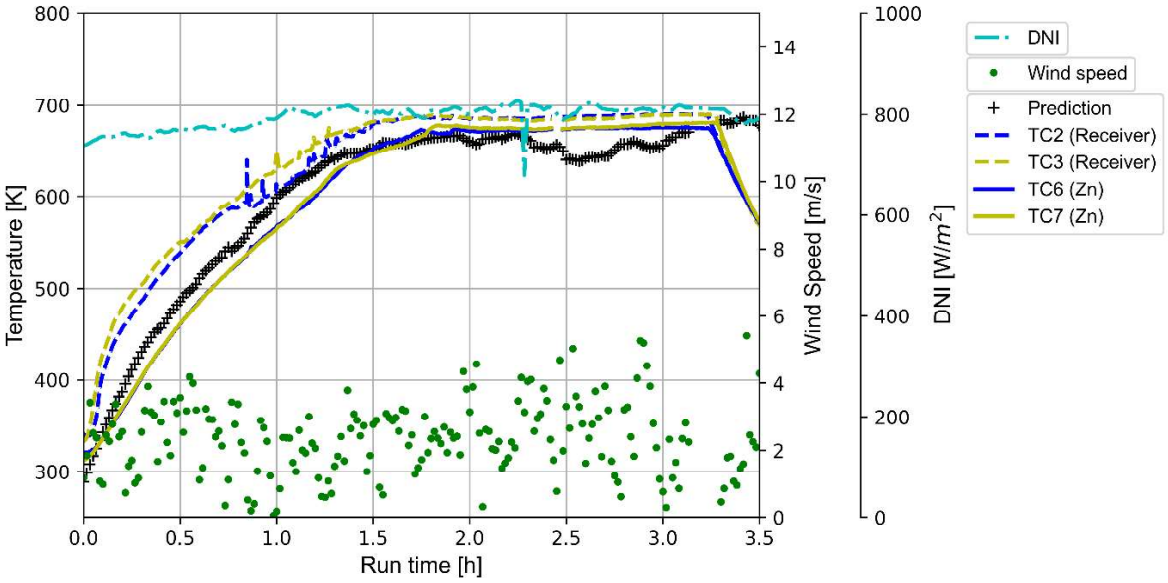

Figure 37. Experiment 2 compared to the analytical model prediction based on historical weather data.

Experiment 3 (see Figure 32) was the only one of the five experiments where the thermocouples were completely covered by solid material and this was because of the limited volume of material drained during Experiment 2. The results from Experiment 2 showed that the melting point was reached, and as a result, most of the inventory softened and settled to the front of the zinc cavity. The material that remained in the zinc cavity after Experiment 2 solidified, but this time with much fewer voids and in good contact with the receiver cavity wall. Another change to Experiment 3 was to add insulation material to the face-plate of the receiver in an attempt to reduce the heat losses from this area. In Figure 38, the results for Experiment 3 are shown, and it is clear that the receiver wall and zinc temperatures follow the same trend as opposed to the other four experiments. The analytical model also accurately predicts these temperatures, and because the zinc and cavity temperatures follow the same trend, the model prediction is much more representative of the zinc material temperatures, which was the intent of the analytical model. Experiment 3 illustrates the most ideal conditions out of all the experiments from the analytical model point of view. The nearly full zinc cavity, with limited voids as a result of Experiment 2, allows for the heat transfer mechanisms assumed in the analytical model. As mentioned, the analytical model assumes a solid zinc inventory that ensures good contact with the receiver cavity wall. This assumption is most closely reproduced in Experiment 3, and the fact

that the predictive model so closely predicts the zinc temperatures provides confidence in the accuracy of the analytical model. A heat transfer efficiency constant of c = 1 was required, which alludes to no correction required to match the predictive model to the experimental results obtained for Experiment 3.

Figure 38 shows the reason for the good recovery of molten material from the receiver (see Table 7) during the tapping procedure of Experiment 3, in that the latent heating phase was just about completed when the experiment was stopped to tap the zinc. This is shown by the sharp increase in the predicted temperature after the latent heating phase, which coincides with when the receiver was removed from the heat source to be tapped. The reason for not draining all of the zinc in the molten state is likely due to the high thermal conductivity of zinc, which caused the material to solidify on the exposed receiver cavity wall as it was removed from the heat source before it could be fully drained.

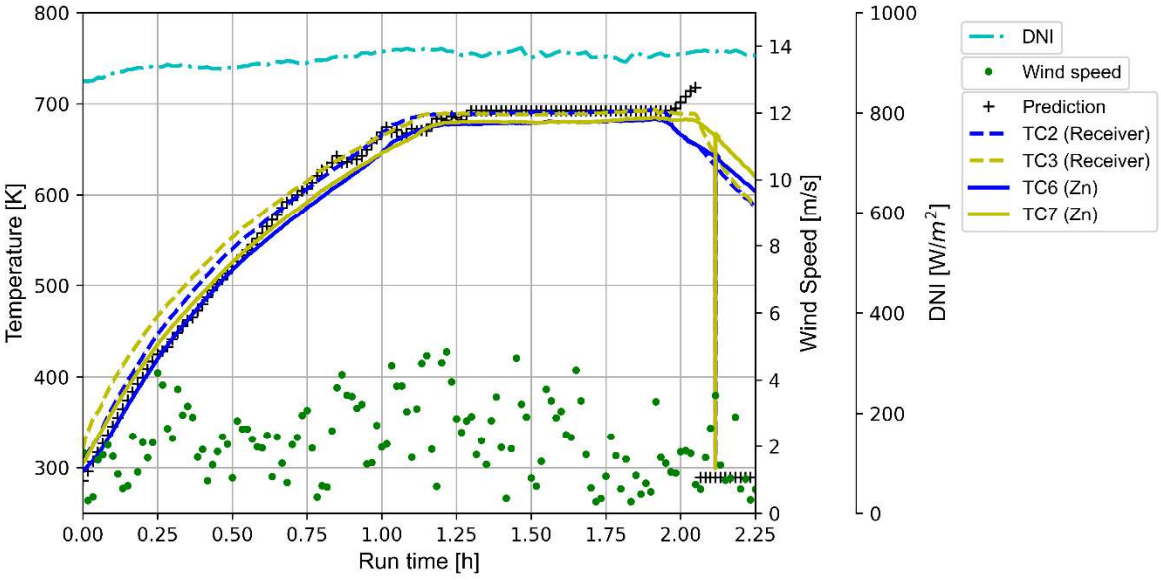

Figure 38. Experiment 3 compared to the analytical model prediction based on historical weather data.

Experiment 4 was the test run conducted during the highest average wind speeds, as shown in Appendix D. Convection and conduction heat losses are directly related to wind speed and direction, and as a result, an increase in wind speed will drastically increase heat losses from the receiver. The effect thereof is shown in Figure 39. It is illustrated by the irregular temperatures (uneven slope) during heat-up (in both the

experimental and predicted temperatures), as well as a longer heat-up when compared to Experiment 3, even though a similar average DNI was recorded. This negatively affected the heat-up time, and less molten material was drained from the receiver during this experiment. The analytical model results shown in Figure 39 again illustrate that the experiment was stopped prematurely and that more heating was required to effectively melt the entire zinc batch. Erratic temperature measurements around the two-and-a-quarter hour mark resulted in temperatures above 720 K and, as per the experimental procedure, served as an indication to drain the zinc cavity. These temperature spikes are likely due to localised heating, either caused by insufficient mixing by the rotational movement of the receiver or by the inconsistent temperature profiles in the cavity receiver due to the higher wind speeds, at which forced convection becomes the driving heat loss mechanism [90]. In order to match the predictive model to the experimental zinc temperatures, a heat transfer efficiency constant of c = 0.8 was required. At higher-than-average wind speeds, it was still possible to match the predictive zinc temperature to that of the experimental results, which again speaks to the accuracy of the analytical model. The reason for the heat transfer efficiency constant is that a significant volume of zinc was drained during Experiment 3, which was then replaced with new zinc feedstock. However, the internal walls of the receiver were still coated with a layer of solid zinc from the previous experiment. This layer of process material from the previous experiment aided in the heat transfer between the receiver cavity wall and the zinc feedstock. A heat transfer efficiency constant of c = 0.8 will, therefore, likely be the best approximation when evaluating the day-to-day operation of this technology.

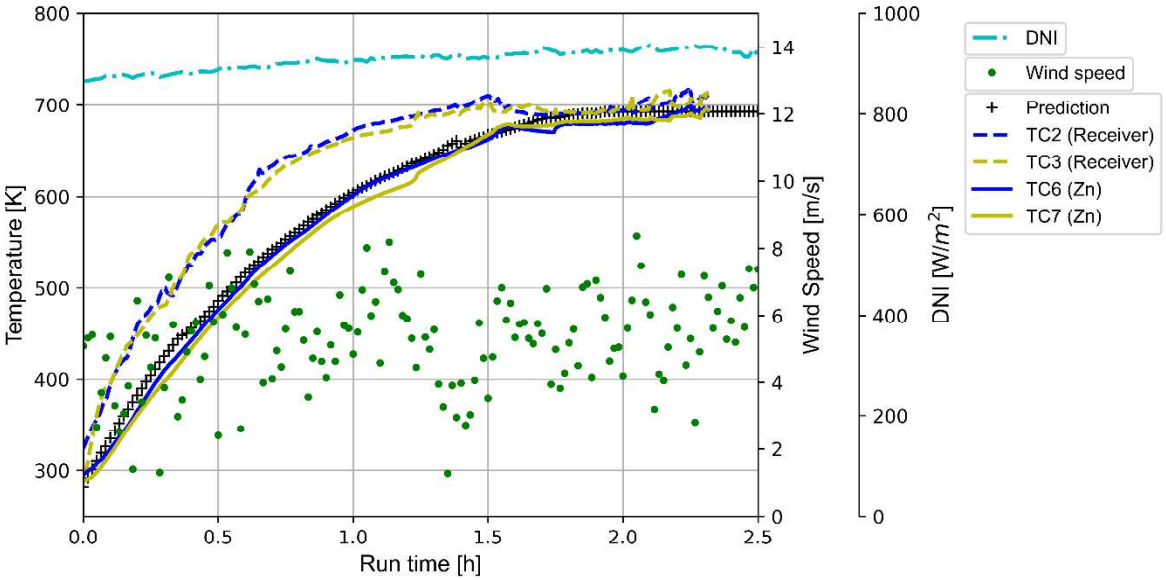

Figure 39. Experiment 4 compared to the analytical model prediction based on historical weather data.

Experiment 5, shown in Figure 40, was executed using a new receiver vessel, a new set of thermocouples, and a fresh batch of zinc feedstock. Significant temperature variations were noticed in the difference between the receiver and zinc temperatures and between the receiver temperatures themselves. The variation between the receiver temperatures is possibly due to localised heating in the zinc particles, resulting in better contact with the receiver wall in some places. This theory is confirmed by the fact that the temperatures converge as soon as the melting temperature of zinc is reached, which indicates that the zinc is softening and is now making good contact with the side wall of the receiver. Also, as opposed to the previous experiment, the wall of the zinc cavity was not lined with a layer of solidified process material from a previous experiment. This negatively affected the heat transfer between the receiver cavity wall and the zinc. During Experiment 5, the lowest wind speed out of all the experiments was recorded, and at these wind speeds, free convection is the driving force for convection heat losses. A heat transfer efficiency constant of c = 0.6 was required to match the predictive model to that of the experimental results. This heat transfer efficiency constant will typically be representative of the first batch of zinc that is processed in a new receiver when evaluating the technology as an industrial application. After the first batch, the heat transfer efficiency constant can be adjusted to c = 0.8, as determined by Experiment 4.

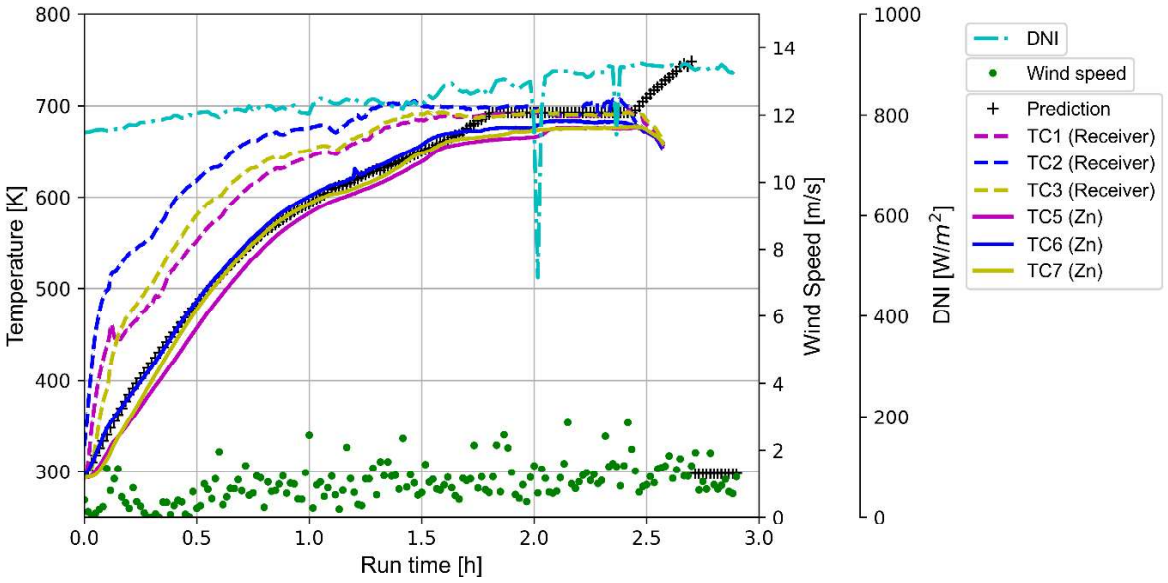

Figure 40. Experiment 5 compared to the analytical model prediction based on historical weather data.

4.4 High-level statistical analysis

In order to better understand how well the predictive model compared with the experimental results, a high-level statistical evaluation was completed on each of the datasets. Three empirical equations were used to determine how well the analytical model predicted the experimental results. The three empirical equations used were the Root Mean Square Error (RMSE), represented by Equation 44, Mean Percentage Error (MPE) and Mean Absolute Percentage Error (MAPE), as shown in Equations 45 and Equation 46, respectively [109]. The RMSE is used, mainly because of the popularity of this equation by statisticians, but it is deemed to be unreliable [109]. Not only are MPE and MAPE easier to understand, but MPE can also provide insight into the bias of the prediction, while MAPE is believed to be a more reliable representation of the statistical error in a data set than RMSE [109].

$$RMSE = \sqrt{\frac{\sum_{SS=1}^{SS}(a_{SS} - f_{SS})^2}{SS}} \tag{44}$$

$$MPE = 100 \times \frac{1}{SS} \sum_{SS=1}^{SS} \frac{a_{SS} - f_{SS}}{a_{SS}} \tag{45}$$

$$MAPE = 100 \times \frac{1}{SS} \sum_{ss=1}^{SS} \left| \frac{a_{ss} - f_{ss}}{a_{ss}} \right| \quad (46)$$

The predicted zinc temperature was compared to the experimentally measured temperature for each timestep. The full sample size was then used to calculate the prediction error for each experimental run. Because of the thermocouple redundancy, there was more than one error for each dataset. An average error was taken for the operational thermocouples. For experiments 1 to 4, two thermocouples were operational and three for experiment 5, which is shown by the solid plotted trendlines in Figure 36 to Figure 40.

After the completion of the statistical analysis of the prediction error, it can be noted that there was on average a 14.89 K RMSE across all five experimental runs. Experiment 2 had the largest difference between the experimental results and the predictive model, which is clear when comparing the different plots in Figure 36 to Figure 40. The negative MPE value highlights the bias of the predictive model to slightly overestimate the zinc temperatures. The MAPE demonstrates not only that there was on average only a 2.7% error between the predictive model and the experimental results, but it also highlights that the heat transfer efficiency constant (*c*) was accurately determined, considering the small difference in MAPE between the different experimental runs.

Table 8. Summary of statistical error of each experimental run.

Empirical method	**RMSE [K]**	**MPE [%]**	**MAPE [%]**
Exp. 1	14.49	-0.66	2.87
Exp. 2	20.46	-0.87	3.21
Exp. 3	13.18	-1.07	2.01
Exp. 4	12.14	-0.66	3.04
Exp. 5	14.21	-1.99	2.34
Average	14.896	-1.05	2.694

4.5 Conclusion

An experimental setup was used to successfully demonstrate that it is possible to melt zinc metal using only CSP as heat input. Five different experimental tests were executed, each with a unique set of environmental conditions, which allowed for a robust data set against which the analytical model was validated. As part of the validation process, a heat transfer efficiency constant (c) was determined. This heat transfer efficiency constant was used to correct and account for the heat transfer in the zinc "as-fed" inventory, which was also unique in each experimental test. Given that solid zinc feedstock is added to the zinc cavity, the irregular shape of the zinc particles results in a reduced heat transfer efficiency between the zinc and the receiver cavity wall. This reduced efficiency depends on the packing structure of the zinc, the zinc particle size, and the build-up from the previous experimental run, making it unique to each test. Using the experimental results, it was possible to demonstrate that the analytical model can correctly, within a MAPE of 2.7 %, predict the temperature of the zinc metal in the receiver. This information can be used to accurately predict when a batch of zinc will be completely molten. The experimental results were also used to determine a heat transfer correction factor for different zinc packing scenarios. A heat transfer efficiency constant of c = 0.6 is recommended for when a new receiver is being used and a new batch of zinc is being melted. This means that there was no previous melt in the receiver that allowed the inside of the zinc cavity to be lined with a layer of solidified zinc to aid in the initial heat transfer. However, after the first batch of molten zinc has been achieved in the receiver, the heat transfer efficiency constant can be increased to c = 0.8. This is because a layer of molten zinc has covered the inside wall of the zinc cavity, allowing for improved heat transfer between the cavity wall and the new batch of zinc feedstock. The heat transfer efficiency constant can only be c = 1 when the zinc inventory contains no voids, but this is highly unlikely for any new batch of zinc feedstock. The accuracy of the experimentally determined heat transfer efficiency correction factor is demonstrated by the small difference in MAPE between the different experimental runs. A standard deviation of only 0.5% is recorded between the MAPE of the five experimental runs when it is compared to the predictive model in terms of temperature.

5. DISCUSSION

5.1 Introduction

The results have shown that it is not only possible to melt zinc using CSP only, but a predictive analytical model can, within a few minutes of accuracy, predict when a batch of zinc inventory will be completely molten as well as the temperature of the zinc inventory. The comparative results shown in Figure 36 to Figure 40 speak to the accuracy of the analytical model and that it can be used to further investigate this technology application.

5.2 Receiver efficiency and heat loss

When the analytical model is broken down into the individual heat loss components, more detail can be provided into which heat loss mechanism has the most significant influence on the efficiency of the system. The heat balance of Experiment 3, shown in Figure 41, indicates that the conduction and radiation heat losses stay relatively constant throughout the experiment, but the convection heat loss is very erratic. The erratic behaviour of the convection heat loss mechanism is related to the variability in the wind speed and direction, and depending on the wind speed, this heat loss mechanism is either driven by free convection, forced convection, or a combination of both. The variability in the heat losses also resulted in the system's efficiency following the same trend. The average overall efficiency obtained for Experiment 3 was 42%, but the instantaneous efficiency varied from 82% to as low as -56%. Negative efficiencies point to a situation where the heat loss exceeds the heat input, and the system is losing energy, instead of gaining energy required to melt the zinc inventory (typically during a wind gust). Note that the instantaneous efficiency is calculated for each time step and is shown in Figure 41 and Figure 42. The achieved average overall efficiency compares well with, but exceeds, the melting efficiency of between 22% and 36% obtained by Demirtas and Ozcan [29] in a similar solar melting study. The results obtained by investigating the individual heat loss mechanism show that convection heat loss is the most unpredictable and has one of the largest influences on the system's efficiency. This statement, in turn, demonstrates the significant effect that environmental conditions, such as wind speed and direction, have on the overall efficiency and stability of this technology application. This is why not only solar input and ambient conditions need to be considered when evaluating CSP technologies for melting applications but also factors such as wind speed and direction.

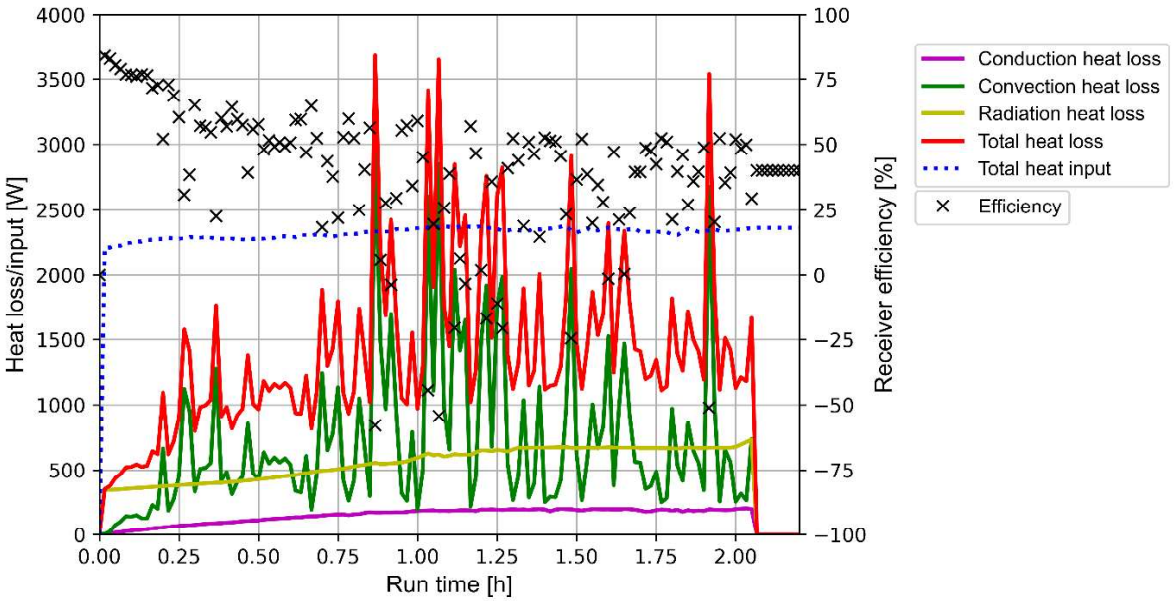

Figure 41. Experiment 3 heat input and heat loss mechanisms are shown together with the instantaneous efficiency of the system.

When the heat losses for Experiment 5 are observed, as shown in Figure 42, much more stability is noticed. This is attributed to much lower wind speeds and resulted in primarily free convection, which is the driving mechanism for convection heat loss. Free convection results in smaller heat losses for the convection heat loss mechanism, and as a result, much lower total heat losses were recorded. Even though much more stable heat losses were recorded, resulting in more stable efficiencies, the average efficiency for Experiment 5 was only 26%. The likely reason for this is the weak internal heat transfer between the receiver cavity wall and the zinc feedstock, which resulted in a lower heat transfer efficiency constant of c = 0.6. Operational issues during this test and the loss of collector surface during the test caused the variability in the total heat input to the system as shown in Figure 42. Figure 42 again demonstrates the large influence that the wind speed and direction have on the system's overall stability, especially when compared to the instability in Figure 41, which is based on much higher wind speeds.

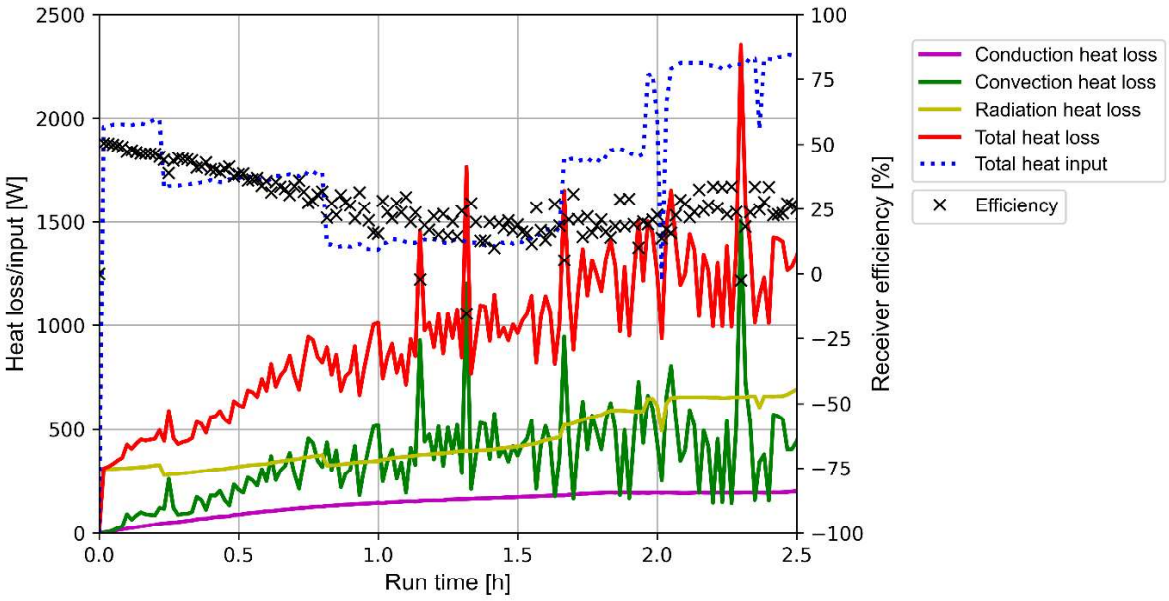

Figure 42. Experiment 5 heat input and heat loss mechanisms are shown together with the instantaneous efficiency of the system.

5.3 Case study

This study aimed to demonstrate that it is possible to melt zinc metal using only a CSP input and to develop an analytical model that can be used as a tool to develop this technology application further. The remelting of zinc cathodes, produced during the hydro-metallurgical production of zinc, has been identified as a suitable application to apply CSP to a high-temperature industrial application. This melting process forms part of the last step in the Roast-Leach-Electrowin (RLE) process. This step is conventionally done by melting the zinc cathodes in induction furnaces.

The analytical model uses historical weather conditions as an input to predict the number of zinc batches that can be processed in a day. Between 07:00 and 17:00, a full-day run on the 16th of August 2022 at Pretoria (South Africa), the setup could produce two molten batches of zinc, as shown in Figure 43. With 17 kg of zinc processed during each batch, and with 80% being tapped, just over 27 kg of molten zinc could be produced during this day, using the tested receiver design. The batch throughput is not only dependent on the solar quality but also on the wind and ambient temperature conditions, as was discussed in the analytical model section.

The environmental influence is evident when Figure 44 is observed, during which the analytical model was re-executed with the weather conditions of the 5th of September 2022 at the same location as for Figure 43. The same analytical model was used,

assuming the same heat transfer efficiency constant of c = 0.8, as determined for day-to-day operations, with the only difference being the weather conditions. On the 5th of September 2022, three complete batches could be processed, resulting in approximately 41 kg of tapped zinc, even though a slightly weaker solar irradiance was recorded on this day. These results again point to the significant influence the wind conditions have on the efficiency of the melting process and as a result, the throughput of this technology application. In average wind speeds of below 2 m/s, the experimental setup in Pretoria therefore has the potential to process 14.4 kg zinc per day per m² of solar collector surface during the spring season, providing an indication of the expected average daily performance over a typical year.

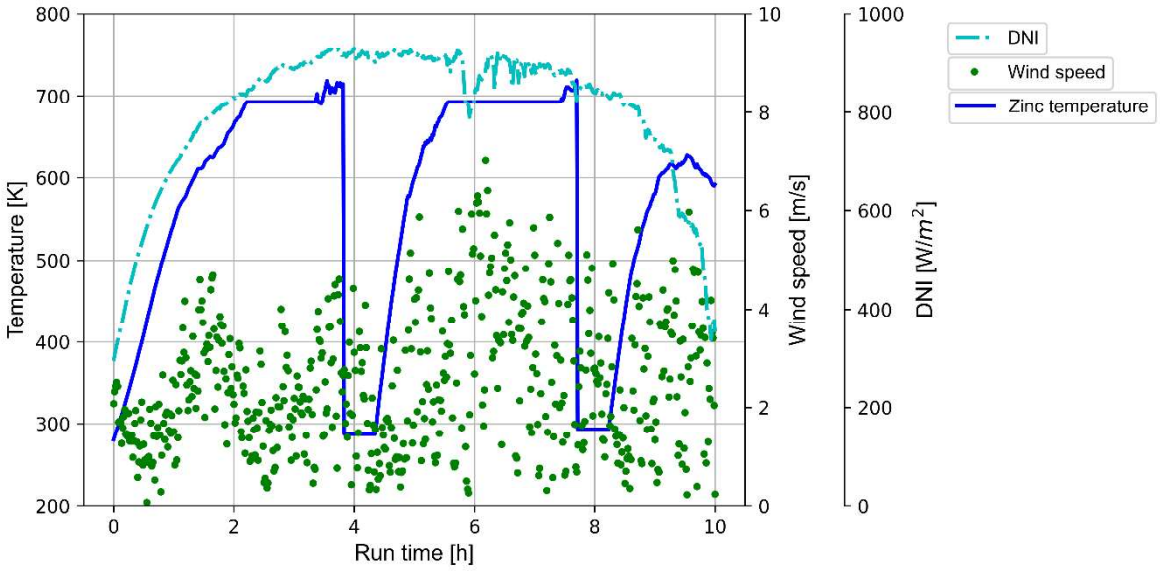

Figure 43. Batch throughput results with DNI and wind speed [108] for the 16th of August 2022 at Pretoria, South Africa.

To further demonstrate the benefit of using CSP for small to medium-scale melting of zinc, these results can be compared with more conventional heat sources. Induction furnaces as well as gas burners can be used for the melting of zinc metal [25], to produce molten zinc for downstream processes such as casting, as mentioned for the RLE process, or recycling applications.- Firstly, considering a small-scale induction furnace with a capacity of housing 15 kg of material, around 600 kWh per ton of electrical power would be required, taking into account an energy efficiency of 70% [110].

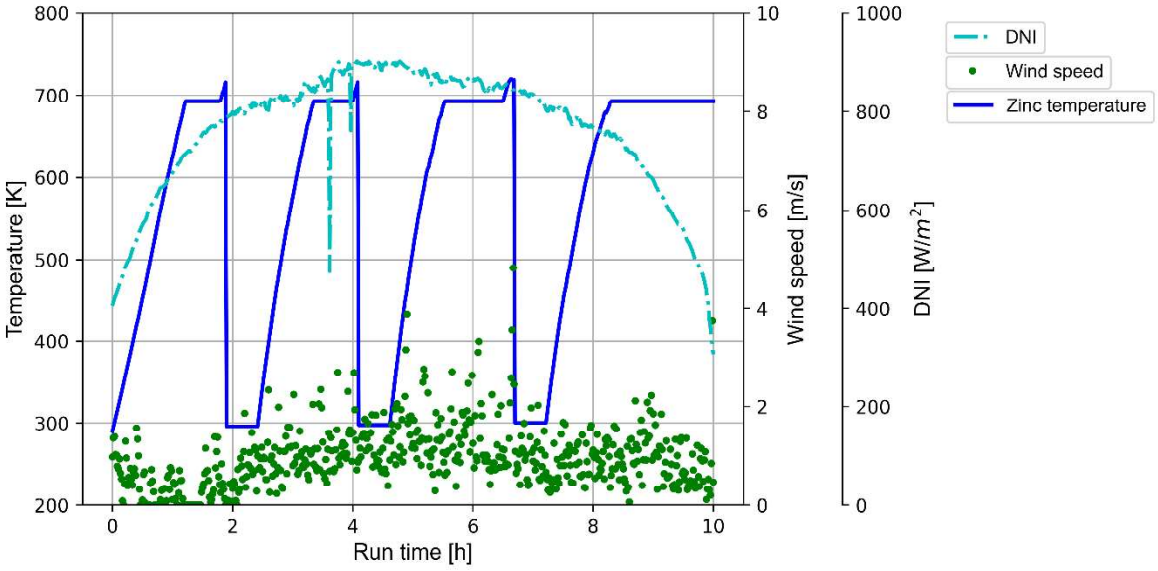

Figure 44. Batch throughput results with DNI and wind speed [108] for the 5th of September 2022 at Pretoria, South Africa.

This would result in an energy requirement of 0.6 kWh/kg of processed zinc, or 24.6 kWh/day to process the same mass of 41 kg as mentioned in the example above. Furthermore, considering that power in South Africa is mostly generated by coal-fired power stations, and assuming a CO_2 emission rate of 0.87 kg CO_2/kWh [111], 0.52 kg CO_2 is emitted for every kilogram of zinc that is processed. This results in 21.3 kg of CO_2 emissions being generated, per day, to produce the same volume of molten zinc as with the solar receiver discussed in this study. CSP melting therefore shows a 100% decrease in CO2 emissions when compared to the CO2 emissions from using electricity

In terms of equipment costs, the solar receiver prototype design used for this study had a total fabrication cost of approximately 9750 ZAR. This cost included the steelwork, insulation material, drive system, as well as the instrumentation required. To put this into perspective, a small-scale induction furnace with a 15 kg capacity costs upwards of 94 000 ZAR [112]. The amounts mentioned aims to show the cost difference between the technologies at this application scale. The CSP system can therefore be a cost-effective and feasible alternative, from an equipment requirement perspective as well, but a detailed feasibility study and financial analysis would be required before this can be said with certainty. The economy of scale principle dictates

that this conclusion will have to be evaluated on a case-by-case basis, depending on the material throughput requirement, operating conditions, and location.

The high-level case study highlights the benefit of making use of CSP as the heat source to melt zinc, not only from an environmental perspective but also from a financial point of view. These results motivate further development of this technology application. The analytical model as well as the cost-saving analysis can be used to evaluate the potential for making use of CSP in industrial applications such as the beneficiation of local zinc resources. The concept of remelting zinc metal has been demonstrated, however, a more detailed financial evaluation is required in future work to determine the feasibility of applying this technology to the conventional zinc metal flowsheet.

5.4 Conclusion

This chapter briefly demonstrated the value of the analytical model developed in support of this study. The model not only emphasised the influence weather conditions have on the output of this CSP application, but it also demonstrated that the computational model has the potential to further develop this field of study and to be used as a tool for feasibility studies based on this solar thermal application. The analytical model was used to determine that receiver melting efficiencies in the range of 42% are achievable. The achieved melting efficiency exceeded the 22% to 36% obtained by Demirtas and Ozcan [29] for a similar technology application. Furthermore, a basic cost study highlighted the potential savings if CSP were used as heat source, opposed to the conventional electrical heating as in the RLE process example. Lastly, this chapter also highlighted the areas for future work, including further development of convection heat loss models that consider environmental conditions, such as wind direction and speed relative to the receiver orientation, and a more detailed investigation into the zinc packing structure's impact on the heat transfer in the system.

6. SUMMARY, CONCLUSION AND RECOMMENDATIONS

6.1 Summary

The large carbon footprint of high-temperature industrial applications and the decline in the beneficiation of local mineral resources are both reasons why an investigation into alternative methods of process heat generation is essential. This research proposes that the combining of a solar thermal technology with a high-temperature process heat application has the potential to address the two issues mentioned. Zinc metal melting has been identified as a suitable industrial application given the favourable material properties of this metal and the versatility and impact of this metal on modern society. Over 80% of the world's zinc is currently being produced through the RLE process of which the last step involves remelting of zinc cathodes at 450 °C [24]. This process step is suitable for making use of CSP technology to provide the necessary heat and reduce the carbon footprint of this industrial application. Considering the substantial zinc reserves in South Africa, coupled with the country's excellent solar resource, applying CSP to zinc melting can have the potential for the local beneficiation of this metal. Currently, no local beneficiation of zinc ore takes place in South Africa, with all ore being exported [14].

The study was initiated by defining the research question, posed above, and by justifying the research. This was followed by a detailed literature review aimed at finding similar applications and learning from each. The literature study was used to gather information and an understanding of the design considerations pertaining to the solar collector and cavity receiver that formed the basis of the experimental setup. The experimental setup was developed to demonstrate that zinc could be melted in batches using the applied solar thermal technology. Together with the experimental work an analytical model was developed in support of this work and for the future development of this field of study.

The experimental setup and experimental methods were used to evaluate the performance of the solar receiver, designed for melting zinc, under realistic environmental conditions. The successful demonstration of zinc melting, using CSP, and the validation of the analytical model were achieved through the experimental tests executed as part of this study.

The current study demonstrated that zinc metal can be melted using only solar thermal energy. The knowledge generated by this study can also be applied to other applications such as remelting, galvanisation, or casting. In combination with demonstrating the potential and practical considerations for using CSP as an industrial heat source, an analytical model was developed that can be used to predict the zinc temperature in a cavity receiver with 2.7% accuracy. The predictive model has the potential to aid in a detailed feasibility study on the use of CSP as the heat source for this and other melting applications. The experimental results and analytical model have shown that it would be possible to process 41 kg of zinc, using the experimental setup, on a day with a peak direct normal irradiance (DNI) of 900 W/m^2 and wind speeds of below 2 m/s. These results, together with the size of the dish concentrator surface, allow for an estimated production rate of 14.4 kg/m^2 per day (based on the reflective surface area of the collector employed).

6.2 Conclusion

This research study presented an experimental investigation into the use of CSP as an alternative heat source for melting zinc metal using a cylindrical cavity receiver and a multi-facet parabolic dish setup. This setup is not only scalable but also a low-cost solution to melting low melting-point metals using CSP. To successfully prove this technology application, five experimental runs were executed. Four of these experimental runs produced molten zinc and demonstrated that it is possible to melt zinc using only CSP. The thermal efficiency of the receiver was calculated to be in the range of 42%, which compares well with the literature [29]. Each of these experimental tests also provided valuable data against which a predictive analytical model could be validated. The analytical model developed as part of this study uses historical solar and weather data as input and can not only be used to further refine the design employed but can also be used as a tool to investigate the feasibility of this technology application. The analytical model can predict the zinc temperature within the cavity receiver with a MAPE of 2.7% for the full melting cycle of this batch-driven application. This study contributes to the fundamental understanding of small-scale solar melting in that this experimental work and the analytical model can be used as building blocks for a variety of other industrial heat applications. These applications range from small-scale casting to galvanisation, all of which could make use of renewable energy as the heat source.

A case study demonstrated the value of this technology application. Not only can up to 0.52 kg of CO_2 emissions be avoided for every kilogram of zinc being processed, but this technology application also unlocks significant energy cost savings. 0.6 kWh per kg of processed zinc can be saved when compared to conventional induction furnace technology that forms part of the RLE zinc production process. The low cost and modularity associated with the design of this CSP system can make this technology application an attractive alternative for low-income or rural users without access to cost-effective power. It can allow entrepreneurs access to small/medium-scale metal die-casting and melting applications, which otherwise might not have been feasible. This work also allows for insight into a greener alternative for the processing of zinc metal, which can afford an opportunity to revisit the beneficiation of zinc ores in South Africa using the country's excellent solar resource.

6.3 Recommendations

This study highlighted other aspects that should be investigated to further refine this technology application and the associated analytical model. Some of the recommendations for future work are as follows:

- Additional research into the influence of wind speed and direction, relative to the receiver aperture, is required to further refine the forced convection heat loss estimation. The model employed for this study, by Reddy et al. [90], served as a good basis and considered both wind speed and wind direction. However, the model had limited validation and was developed for a different receiver and solar collector design. A better understanding of the mechanisms at play during the transition from free to forced convection, or the combination thereof, is still required.
- The heat transfer mechanisms in the zinc feedstock and their influence on the greater heat balance should be investigated in greater detail. The effect of the heat transfer within the zinc feedstock was not modelled but was determined through experimental work. It was found that the heat transfer efficiency constant (c) for a new batch and a new receiver vessel is in the range of 0.6. Once a molten batch has been achieved with the receiver, which will be the case for the day-to-day operation of this technology application, a heat transfer efficiency constant of $c \approx 0.8$ was determined. This heat transfer efficiency constant considers that a coating of process material remained in the receiver

after the previous batch of zinc was drained, after which a new batch is then added. The new batch will result in several voids in the inventory, but the surface coating will aid in the initial heat transfer. A heat transfer efficiency constant of c = 1 can only be assumed when a solid zinc inventory is used (no air gaps in the zinc inventory). Therefore, the heat transfer efficiency constant (c) also correlates with the mass of zinc in the receiver during the experimental run. Considering that the mass of the receiver vessel is also included during the sensible heating phase, the ratio of steel to zinc changes as less or more zinc is charged to the zinc container. The use of the zinc mass as an indication of the heat transfer efficiency constant (c), based on a zinc-to-steel ratio or the air void volume as a result of the mass of zinc charged, can also be considered in a future study.

- Successive experimental test runs are required to better define typical batch refill times and procedures for day-to-day operation. This work assumed a batch refill time of 30 minutes, but this might differ during operation. The refill time will depend on the method of charging zinc feedstock or by changing out the whole receiver assembly. More operational test work will be beneficial to refine the 30-minute assumption and improve the accuracy of the predictive model.
- A parametric investigation for optimising the cavity receiver geometry, and the associated parabolic dish, can be of use to further develop this technology application of using CSP to process low melting temperature metals.
- The development of a cost-effective flux mapping method for cavity receivers can aid in the optimisation of cavity receiver geometry and better define the actual heat input to the receiver.
- The analytical model developed and validated as part of this work can be used to complete a detailed feasibility study and financial analysis of the current or related technology applications. The model can be used to determine the suitability of different locations, considering that it makes use of actual historical weather data to determine the throughput of the technology application.
- The knowledge generated by demonstrating the melting of zinc metal using CSP can serve as the basis for various other zinc metal-related research including, but not limited to, metal phase-change studies, solar galvanisation, and thermal storage. This research can also be applied to other low-melting-point metal processing applications, including casting and recycling.

7. REFERENCES

[1] C. Philibert, “Renewable Energy for Industry,” IEA, Paris, 2017. [Online]. Available: https://www.iea.org/reports/renewable-energy-for-industry

[2] S. A. Kalogirou, “Solar thermal collectors and applications,” *Prog. Energy Combust. Sci.*, vol. 30, no. 3, pp. 231–295, 2004, doi: 10.1016/j.pecs.2004.02.001.

[3] L. Kumar, M. Hasanuzzaman, and N. A. Rahim, “Global advancement of solar thermal energy technologies for industrial process heat and its future prospects: A review,” *Energy Convers. Manag.*, vol. 195, pp. 885–908, Sep. 2019, doi: 10.1016/j.enconman.2019.05.081.

[4] L. G. Rosa, “Solar Heat for Materials Processing: A Review on Recent Achievements and a Prospect on Future Trends,” *ChemEngineering*, vol. 3, no. 4, p. 83, Oct. 2019, doi: 10.3390/chemengineering3040083.

[5] WWF, “Industrial scale solar heat in South Africa,” WWF Netbank Green Trust, Cape Town, 2017.

[6] World Bank Group, “Global Solar Atlas 2.0,” Map and data download. Accessed: Feb. 11, 2021. [Online]. Available: https://globalsolaratlas.info/download/world

[7] E. C. Joubert, S. Hess, and J. L. Van Niekerk, “Large-scale solar water heating in South Africa: Status, barriers and recommendations,” *Renew. Energy*, vol. 97, pp. 809–822, Nov. 2016, doi: 10.1016/j.renene.2016.06.029.

[8] S. Kalogirou, “The potential of solar industrial process heat applications,” *Appl. Energy*, vol. 76, no. 4, pp. 337–361, Dec. 2003, doi: 10.1016/S0306-2619(02)00176-9.

[9] M. Azadi, S. A. Northey, S. H. Ali, and M. Edraki, “Transparency on greenhouse gas emissions from mining to enable climate change mitigation,” *Nat. Geosci.*, vol. 13, no. 2, pp. 100–104, Feb. 2020, doi: 10.1038/s41561-020-0531-3.

[10] T. Eglinton, J. Hinkley, A. Beath, and M. Dell’Amico, “Potential Applications of Concentrated Solar Thermal Technologies in the Australian Minerals Processing and Extractive Metallurgical Industry,” *JOM*, vol. 65, no. 12, pp. 1710–1720, Dec. 2013, doi: 10.1007/s11837-013-0707-z.

[11] “Zinc Statistics and Information.” Accessed: Feb. 16, 2021. [Online]. Available: https://www.usgs.gov/centers/nmic/zinc-statistics-and-information

[12] G. Kong and R. White, “Toward cleaner production of hot dip galvanizing industry in China,” *J. Clean. Prod.*, vol. 18, pp. 1092–1099, 2010, doi: 10.1016/j.jclepro.2010.03.006.

[13] S. Mohale *et al.*, “South African mineral industry 2013 - 2014,” Department of Mineral Resources - Republic of South Africa, Pretoria, ISBN: 978-0-621-43629-7, 2015.

[14] MCSA, “MCSA Facts and Figures 2017,” Mineral Council South Africa, Johannesburg, 2018.

[15] World Bank Group, “Solar resource maps of South Africa,” SOLARGIS. Accessed: Feb. 15, 2021. [Online]. Available: https://solargis.com/maps-and-gis-data/download/south-africa

[16] C. J. Voster, “Simplified geology and Zinc deposits,” Council of Geoscience. Accessed: Feb. 15, 2021. [Online]. Available: https://www.geoscience.org.za/images/Maps/zinc.gif

[17] E. Koepf, S. G. Advani, A. Steinfeld, and A. K. Prasad, “A novel beam-down, gravity-fed, solar thermochemical receiver/reactor for direct solid particle decomposition: Design, modeling, and experimentation,” *Int. J. Hydrog. Energy*, vol. 37, no. 22, pp. 16871–16887, Nov. 2012, doi: 10.1016/j.ijhydene.2012.08.086.

[18] E. Koepf, I. Alxneit, C. Wieckert, and A. Meier, “A review of high temperature solar driven reactor technology: 25years of experience in research and development at the Paul Scherrer Institute,” *Appl. Energy*, vol. 188, pp. 620–651, Feb. 2017, doi: 10.1016/j.apenergy.2016.11.088.

[19] M. Chambon, S. Abanades, and G. Flamant, “Thermal dissociation of compressed ZnO and SnO2 powders in a moving-front solar thermochemical reactor,” *AIChE J.*, vol. 57, no. 8, pp. 2264–2273, Aug. 2011, doi: 10.1002/aic.12432.

[20] A. Steinfeld, M. Brack, A. Meier, A. Weidenkaff, and D. Wuillemin, “A Solar Chemical Reactor for Co-production of Zinc and Synthesis Gas,” *Energy*, vol. 23, no. 10, p. 12, 1998.

[21] C. Wieckert *et al.*, “A 300 kW Solar Chemical Pilot Plant for the Carbothermic Production of Zinc,” *J. Sol. Energy Eng.*, vol. 129, p. 7, 2007.

[22] S. Moller and R. Palumbo, “The Development of a Solar Chemical Reactor for the Direct Thermal Dissociation of Zinc Oxide,” *J. Sol. Energy Eng.*, vol. 123, no. 2, pp. 83–90, May 2001, doi: 10.1115/1.1349717.

[23] C. Agrafiotis, M. Roeb, and C. Sattler, “A review on solar thermal syngas production via redox pair based water carbon dioxide splitting thermochemical cycles,” *Renew. Sustain. Energy Rev.*, vol. 42, pp. 254–285, 2015.

[24] K. K. Sahu and A. Agrawal, “Lead Zinc Extraction Processes,” in *Proceedings on Extraction of Nonferrous Metals and their Recycling*, Jamshedpur, 2008, pp. 57–70.

[25] J. P. van Dyk, “An Overview of the Zincor Process,” in *South African Institute of Mining and Metallurgy*, Johannesburg, South Africa: South African Institute of Mining and Metallurgy, Mar. 2006.

[26] N. A. Sithole, L. Hockaday, and P. J. A. Bezuidenhout, “Solar Energy for Greener Zinc processing in South Africa,” in *IMPC 2020 Congress Proceedings*, Cape Town, South Africa: The Southern African Institute of Mining and Metallurgy, Oct. 2020, pp. 3779–3791.

[27] M. Ram, M. Child, A. Aghahosseini, D. Bogdanov, and A. Poleva, “Comparing electricity production costs of renewables to fossil and nuclear power plants in G20 countries,” Lappeenranta University of Technology, Hamburg, 2017.

[28] SolAbility, “The cost of Fossil Energy Vs. Renewable Energy Cost (2014-2040),” Zürich, 2015. [Online]. Available: http://solability.com/

[29] C. Demirtaş and A. K. Özcan, “The experimental thermal analysis of aluminum metal melting with concentrated solar energy,” *Sol. Energy Mater. Sol. Cells*, vol. 222, 2021, doi: 10.1016/j.solmat.2020.110940.

[30] K. O. Akpeji, A. O. Olasoji, C. Gaunt, D. T. O. Oyedokun, K. O. Awodele, and K. A. Folly, “Economic impact of electricity supply interruptions in South Africa,” *SAIEE Afr. Res. J.*, vol. 111, no. 2, pp. 73–87, Jun. 2020, doi: 10.23919/SAIEE.2020.9099495.

[31] D. Fernández-González *et al.*, “Concentrated solar energy applications in materials science and metallurgy,” *Sol. Energy*, vol. 170, pp. 520–540, Aug. 2018, doi: 10.1016/j.solener.2018.05.065.

[32] M. R. Broadley, P. J. White, J. P. Hammond, I. Zelko, and A. Lux, “Zinc in plants,” *New Phytol.*, vol. 173, no. 4, pp. 677–702, Mar. 2007, doi: 10.1111/j.1469-8137.2007.01996.x.

[33] “zinc | Properties, Uses, & Facts,” Encyclopedia Britannica. Accessed: Mar. 08, 2021. [Online]. Available: https://www.britannica.com/science/zinc

[34] M. J. Assael, I. J. Armyra, J. Brillo, S. V. Stankus, J. Wu, and W. A. Wakeham, “Reference Data for the Density and Viscosity of Liquid Cadmium, Cobalt, Gallium, Indium, Mercury, Silicon, Thallium, and Zinc,” *J. Phys. Chem. Ref. Data*, vol. 41, no. 3, p. 033101, Sep. 2012, doi: 10.1063/1.4729873.

[35] T. Bergman, A. Lavine, F. Incropera, and D. Dewitt, *Fundamentals of Heat and Mass Transfer*, 7th ed. USA: Hohn Wiley & Sons, 2011.

[36] Agilent Technologies, “Material Expansion Coefficients,” Agilent Technologies, 2002. [Online]. Available: https://psec.uchicago.edu/thermal_coefficients/cte_metals_05517-90143.pdf

[37] D. Hahn and N. Ozisik, *Heat Conduction*, 3rd ed. Hoboken, New Jersey: John Wiley & Sons, INC., 2012.

[38] Y. S. Touloukian, R. W. Powell, C. Y. Ho, and P. G. Klemens, *Thermal Conductivity - Metallic elements and alloys*, vol. 1. in Thermophysical properties of matter, vol. 1. New York, Washington: Plenum Publishing Corporation, 1970.

[39] A. McKenzie, “A new process for the thermal refining of zinc: A case study of technology development at Mintek,” *J. South Afr. Inst. Min. Metall.*, pp. 315–322, 2004.

[40] S. Suman, Mohd. K. Khan, and M. Pathak, “Performance enhancement of solar collectors—A review,” *Renew. Sustain. Energy Rev.*, vol. 49, pp. 192–210, Sep. 2015, doi: 10.1016/j.rser.2015.04.087.

[41] H. Mousazadeh, A. Keyhani, A. Javadi, H. Mobli, K. Abrinia, and A. Sharifi, “A review of principle and sun-tracking methods for maximizing solar systems output,” *Renew. Sustain. Energy Rev.*, vol. 13, no. 8, pp. 1800–1818, Oct. 2009, doi: 10.1016/j.rser.2009.01.022.

[42] J. Coventry and C. Andraka, “Dish systems for CSP,” *Sol. Energy*, vol. 152, pp. 140–170, Aug. 2017, doi: 10.1016/j.solener.2017.02.056.

[43] P. Haueter, T. Seitz, and A. Steinfeld, “A New High-Flux Solar Furnace for High-Temperature Thermochemical Research,” *J. Sol. Energy Eng.*, vol. 121, no. 1, p. 4, 1999, doi: 10.1115/1.2888146.

[44] C. Sierra and A. J. Vázquez, “High solar energy concentration with a Fresnel lens,” *J. Mater. Sci.*, vol. 40, no. 6, pp. 1339–1343, Mar. 2005, doi: 10.1007/s10853-005-0562-6.

[45] D. Apelian, M. Paliwal, and D. C. Herrschaft, “Casting with Zinc Alloys,” *JOM*, vol. 33, no. 11, pp. 12–20, Nov. 1981, doi: 10.1007/BF03339527.

[46] Kirk and Othmer, *Encyclopedia of Chemical Technology*. John Wiley & Sons, INC., 2000.

[47] P. Haueter, S. Moeller, R. Palumbo, and A. Steinfeld, “The production of zinc by thermal dissociation of zinc oxide - solar chemical reactor design,” *Sol. Energy*, vol. 67, pp. 161–167, 1999.

[48] L. O. Schunk, P. Haeberling, S. Wepf, D. Wuillemin, A. Meier, and A. Steinfeld, “A Receiver-Reactor for the Solar Thermal Dissociation of Zinc Oxide,” *J. Sol. Energy Eng.*, vol. 130, no. 2, p. 021009, May 2008, doi: 10.1115/1.2840576.

[49] H. I. Villafán-Vidales, S. Abanades, M. Montiel-González, H. Romero-Paredes, C. A. Arancibia-Bulnes, and C. A. Estrada, “Transient heat transfer simulation of a 1kWth moving front solar thermochemical reactor for thermal dissociation of compressed ZnO,” *Chem. Eng. Res. Des.*, vol. 93, pp. 174–184, Jan. 2015, doi: 10.1016/j.cherd.2014.05.027.

[50] T. Osinga, U. Frommherz, A. Steinfeld, and C. Wieckert, “Experimental Investigation of the Solar Carbothermic Reduction of ZnO Using a Two-cavity Solar Reactor,” *J. Sol. Energy Eng.*, vol. 126, no. 1, pp. 633–637, Feb. 2004, doi: 10.1115/1.1639001.

[51] C. Wieckert, R. Palumbo, and U. Frommherz, “A two-cavity reactor for solar chemical processes: heat transfer model and application to carbothermic reduction of ZnO,” *Energy*, vol. 29, no. 5–6, pp. 771–787, Apr. 2004, doi: 10.1016/S0360-5442(03)00183-X.

[52] B. Schaffner, A. Meier, D. Wuillemin, W. Hoffelner, and A. Steinfeld, “Recycling of Hazardous Solid Waste Material Using High-Temperature Solar Process Heat. 2. Reactor Design and Experimentation,” *Environ. Sci. Technol.*, vol. 37, no. 1, pp. 165–170, Jan. 2003, doi: 10.1021/es020056o.

[53] C. Wieckert *et al.*, “The SOLZINC-project for up-scaling the solar chemical technology for producing zinc as a solar fuel,” p. 2, 2002.

[54] N. Tzouganatos, R. Matter, C. Wieckert, J. Antrekowitsch, M. Gamroth, and A. Steinfeld, “Thermal Recycling of Waelz Oxide Using Concentrated Solar Energy,” *JOM*, vol. 65, no. 12, pp. 1733–1743, Dec. 2013, doi: 10.1007/s11837-013-0778-x.

[55] K.-H. Funken, M. Roeb, P. Schwarzboezl, and H. Warnecke, “Aluminum Remelting using Directly Solar-Heated Rotary Kilns,” *J. Sol. Energy Eng.*, vol. 123, no. 2, pp. 117–124, May 2001, doi: 10.1115/1.1355242.

[56] M. N. Puttkamer, M. Roeb, S. Tescari, L. de Oliveira, and C. Sattler, “Solar Aluminum Recycling in a Directly Heated Rotary Kiln,” in *REWAS 2016: Towards Materials Resource Sustainability*, 2016, p. 6.

[57] S. O. Alexopoulos, J. Dersch, M. Roeb, and R. Pitz-Paal, “Simulation model for the transient process behaviour of solar aluminium recycling in a rotary kiln,” *Appl. Therm. Eng.*, vol. 78, pp. 387–396, Mar. 2015, doi: 10.1016/j.applthermaleng.2015.01.007.

[58] A. A. Abdurakhmanov, P. Yu. Akbarov, Zh. Z. Akhadov, M. A. Mamatkosimov, Yu. B. Sobirov, and U. F. Turaeva, “Creating melting furnaces based on the large solar furnace,” *Appl. Sol. Energy*, vol. 44, no. 4, pp. 284–287, Dec. 2008, doi: 10.3103/S0003701X08040129.

[59] C. K. Ho and B. D. Iverson, “Review of high-temperature central receiver designs for concentrating solar power,” *Renew. Sustain. Energy Rev.*, vol. 29, pp. 835–846, Jan. 2014, doi: 10.1016/j.rser.2013.08.099.

[60] L. C. Ngo, T. Bello-Ochende, and J. P. Meyer, “Three-dimensional analysis and numerical optimization of combined natural convection and radiation heat loss in solar cavity receiver with plate fins insert,” *Energy Convers. Manag.*, vol. 101, pp. 757–766, Sep. 2015, doi: 10.1016/j.enconman.2015.05.061.

[61] W. G. Le Roux, T. Bello-Ochende, and J. P. Meyer, “The efficiency of an open-cavity tubular solar receiver for a small-scale solar thermal Brayton cycle,” *Energy Convers. Manag.*, vol. 84, pp. 457–470, Aug. 2014, doi: 10.1016/j.enconman.2014.04.048.

[62] E. Bellos, E. Bousi, C. Tzivanidis, and S. Pavlovic, “Optical and thermal analysis of different cavity receiver designs for solar dish concentrators,” *Energy Convers. Manag. X*, vol. 2, p. 100013, Apr. 2019, doi: 10.1016/j.ecmx.2019.100013.

[63] A. M. Daabo, S. Mahmoud, and R. K. Al-Dadah, “The effect of receiver geometry on the optical performance of a small-scale solar cavity receiver for parabolic dish applications,” *Energy*, vol. 114, pp. 513–525, Nov. 2016, doi: 10.1016/j.energy.2016.08.025.

[64] Y. Shuai, X.-L. Xia, and H.-P. Tan, “Radiation performance of dish solar concentrator/cavity receiver systems,” *Sol. Energy*, vol. 82, no. 1, pp. 13–21, Jan. 2008, doi: 10.1016/j.solener.2007.06.005.

[65] Z. Si-Quan, L. Xin-Feng, D. Liu, and M. Qing-Song, “A numerical study on optical and thermodynamic characteristics of a spherical cavity receiver,” *Appl. Therm. Eng.*, vol. 149, pp. 11–21, Feb. 2019, doi: 10.1016/j.applthermaleng.2018.10.030.

[66] N. Sendhil Kumar and K. S. Reddy, “Comparison of receivers for solar dish collector system,” *Energy Convers. Manag.*, vol. 49, no. 4, pp. 812–819, Apr. 2008, doi: 10.1016/j.enconman.2007.07.026.

[67] S. Pavlovic, R. Loni, E. Bellos, D. Vasiljević, G. Najafi, and A. Kasaeian, “Comparative study of spiral and conical cavity receivers for a solar dish collector,” *Energy Convers. Manag.*, vol. 178, pp. 111–122, Dec. 2018, doi: 10.1016/j.enconman.2018.10.030.

[68] A. Kasaeian, A. Kouravand, M. A. V. Rad, S. Maniee, and F. Pourfayaz, “Cavity receivers in solar dish collectors: A geometric overview,” *Renew. Energy*, vol. 169, pp. 53–79, 2021, doi: https://doi.org/10.1016/j.renene.2020.12.106.

[69] T. Hahm, H. Schmidt, and B. Lebmann, “A cone concentrator for high-temperature solar cavity receivers,” *Sol. Energy*, vol. 65, no. 1, pp. 33–41, 1999, doi: 10.1016/S0038-092X(98)00119-4.

[70] K. S. Reddy and N. Sendhil Kumar, “An improved model for natural convection heat loss from modified cavity receiver of solar dish concentrator,” *Sol. Energy*, vol. 83, no. 10, pp. 1884–1892, Oct. 2009, doi: 10.1016/j.solener.2009.07.001.

[71] S.-Y. Wu, L. Xiao, Y. Cao, and Y.-R. Li, “Convection heat loss from cavity receiver in parabolic dish solar thermal power system: A review,” *Sol. Energy*, vol. 84, no. 8, pp. 1342–1355, Aug. 2010, doi: 10.1016/j.solener.2010.04.008.

[72] K. L. Lee, A. Chinnici, M. Jafarian, M. Arjomandi, B. Dally, and G. Nathan, “The influence of wind speed, aperture ratio and tilt angle on the heat losses from a finely controlled heated cavity for a solar receiver,” *Renew. Energy*, vol. 143, pp. 1544–1553, Dec. 2019, doi: 10.1016/j.renene.2019.05.015.

[73] S. Wu, C.-H. Cheng, Y.-J. Hsiao, R.-C. Juang, and W.-F. Wen, “Fe 2 O 3 films on stainless steel for solar absorbers,” *Renew. Sustain. Energy Rev.*, vol. 58, pp. 574–580, May 2016, doi: 10.1016/j.rser.2015.12.263.

[74] K. B. Watson, B. G. Cannon, M. Bosman, and H. Li, “Welding consumables for galvanising kettles,” *Aust. Weld. J.*, vol. 46, no. Fourth Quarter, pp. 33–38, 2001.

[75] S. G. Blakey and S. B. M. Beck, “The effect of combined radiation and convection on hot dip galvanizing kettle wear,” *Appl. Therm. Eng.*, vol. 24, no. 8–9, pp. 1301–1319, Jun. 2004, doi: 10.1016/j.applthermaleng.2003.11.025.

[76] G. Vourlias, N. Pistofidis, D. Chaliampalias, E. Pavlidou, and G. Stergioudis, “On the corrosion mechanism of zinc pack coatings deposited on low carbon steel: results of laboratory tests,” *Corros. Eng. Sci. Technol.*, vol. 42, no. 2, pp. 152–160, Jun. 2007, doi: 10.1179/174327807X159899.

[77] N. Pistofidis, G. Vourlias, G. Stergioudis, E. K. Polychroniadis, and D. Tsipas, “Hot-Dip Galvanized and Alternative Zinc Coatings,” *Corros Prot Process Manag Technol*, pp. 1–38, 2009.

[78] Z. Chongzhe *et al.*, “Design and Optimization of a High-Temperature Cavity Receiver for a Solar Energy Cascade Utilization System,” *Renew. Energy*, vol. 102, 2016, doi: 10.1016/j.renene.2016.11.044.

[79] A. Singh and S. K. Natarajan, “Comparative study of modified conical cavity receiver with other receivers for solar parabolic dish collector system,” *Res. Sq.*, 2021, doi: 10.21203/rs.3.rs-237950/v1.

[80] A. Kasaeian, A. Kouravand, M. A. Vaziri Rad, S. Maniee, and F. Pourfayaz, “Cavity receivers in solar dish collectors: A geometric overview,” *Renew. Energy*, vol. 169, pp. 53–79, May 2021, doi: 10.1016/j.renene.2020.12.106.

[81] T. Taumoefolau, S. Paitoonsurikarn, G. Hughes, and K. Lovegrove, “Experimental Investigation of Natural Convection Heat Loss From a Model Solar Concentrator Cavity Receiver,” *J. Sol. Energy Eng.*, vol. 126, no. 2, pp. 801–807, May 2004, doi: 10.1115/1.1687403.

[82] T. Yazdanipour, F. Shahraki, and D. M. Kalhori, “Experimental analysis of free convection heat loss in a bicylindrical cavity receiver,” *Therm. Sci. Eng. Prog.*, vol. 20, p. 100663, Dec. 2020, doi: 10.1016/j.tsep.2020.100663.

[83] E. Abbasi-Shavazi, J. F. Torres, G. Hughes, and J. Pye, “Experimental correlation of natural convection losses from a scale-model solar cavity receiver with non-isothermal surface temperature distribution,” *Sol. Energy*, vol. 198, pp. 355–375, Mar. 2020, doi: 10.1016/j.solener.2020.01.023.

[84] R. Y. Ma, “Wind effects on convective heat loss from a cavity receiver for a parabolic concentrating solar collector. Sandia Laboratory,” California State Polytechnic University, California, SAND92-7293, 1993.

[85] A. M. Clausing, “Convective Losses From Cavity Solar Receivers—Comparisons Between Analytical Predictions and Experimental Results,” *J. Sol. Energy Eng.*, vol. 105, no. 1, pp. 29–33, Feb. 1983, doi: 10.1115/1.3266342.

[86] J. A. Harris and T. G. Lenz, “Thermal performance of solar concentrator-cavity receiver systems,” *Sol. Energy*, vol. 34, no. 2, pp. 135–142, 1985, doi: 10.1016/0038-092x(85)90170-7.

[87] M. Prakash, S. B. Kedare, and J. K. Nayak, “Investigations on heat losses from a solar cavity receiver,” *Sol. Energy*, vol. 83, no. 2, pp. 157–170, Feb. 2009, doi: 10.1016/j.solener.2008.07.011.

[88] R. D. Jilte, S. B. Kedare, and J. K. Nayak, “Investigation on Convective Heat Losses from Solar Cavities under Wind Conditions,” *Energy Procedia*, vol. 57, pp. 437–446, 2014, doi: 10.1016/j.egypro.2014.10.197.

[89] M. Uzair, T. N. Anderson, and R. J. Nates, “Modeling of convective heat loss from a cavity receiver coupled to a dish concentrator,” *Sol. Energy*, vol. 176, pp. 496–505, Dec. 2018, doi: 10.1016/j.solener.2018.10.060.

[90] K. S. Reddy, G. Veershetty, and T. Srihari Vikram, “Effect of wind speed and direction on convective heat losses from solar parabolic dish modified cavity receiver,” *Sol. Energy*, vol. 131, pp. 183–198, Jun. 2016, doi: 10.1016/j.solener.2016.02.039.

[91] K. L. Lee, A. Chinnici, M. Jafarian, M. Arjomandi, B. Dally, and G. Nathan, “Experimental investigation of the effects of wind speed and yaw angle on heat losses from a heated cavity,” *Sol. Energy*, vol. 165, pp. 178–188, May 2018, doi: 10.1016/j.solener.2018.03.023.

[92] C. Roosendaal, J. K. Swanepoel, and W. G. Le Roux, “Performance analysis of a novel solar concentrator using lunar flux mapping techniques,” *Sol. Energy*, vol. 206, pp. 200–215, Aug. 2020, doi: 10.1016/j.solener.2020.05.050.

[93] J. K. Swanepoel, W. G. le Roux, A. S. Lexmond, and J. P. Meyer, “Helically coiled solar cavity receiver for micro-scale direct steam generation,” *Appl. Therm. Eng.*, vol. 185, p. 116427, Feb. 2021, doi: 10.1016/j.applthermaleng.2020.116427.

[94] Sundog, “EverBright | SundogSolarTech | Arvada,” SundogSolarTech. Accessed: Oct. 16, 2022. [Online]. Available: https://www.sundogsolartech.com

[95] J. K. Swanepoel, C. Roosendaal, and W. G. le Roux, “Photogrammetry analysis of a vacuum-membrane solar dish using elliptical television antennas,” presented at the SOLARPACES 2020: 26th International Conference on Concentrating

Solar Power and Chemical Energy Systems, Freiburg, Germany, 2022, p. 120021. doi: 10.1063/5.0087025.

[96] G. Zanganeh, A. Pedretti, S. Zavattoni, M. Barbato, and A. Steinfeld, “Packed-bed thermal storage for concentrated solar power – Pilot-scale demonstration and industrial-scale design,” *Sol. Energy*, vol. 86, no. 10, pp. 3084–3098, Oct. 2012, doi: 10.1016/j.solener.2012.07.019.

[97] R. C. Gee, *Development of an Abrasion-Resistant Antisoiling Coating for Front-Surface Reflectors - SunShot Incubator Program*. 2017.

[98] SANS 1431, “350WA - Weldable structural steel.” SANS, 2020. [Online]. Available: https://www.metaldata.info/reports/350WA.pdf

[99] H. Sadiq, M. B. Wong, J. Tashan, R. Al-Mahaidi, and X.-L. Zhao, “Determination of Steel Emissivity for the Temperature Prediction of Structural Steel Members in Fire,” *J. Mater. Civ. Eng.*, vol. 25, no. 2, pp. 167–173, Feb. 2013, doi: 10.1061/(ASCE)MT.1943-5533.0000607.

[100] S. Sarkar, M. Gopinath, S. S. Chakraborty, B. Syed, and A. K. Nath, “Analysis of temperature and surface hardening of low carbon thin steel sheets using Yb-fiber laser,” *Surf. Coat. Technol.*, vol. 302, pp. 344–358, Sep. 2016, doi: 10.1016/j.surfcoat.2016.06.045.

[101] Raspberry Pi Ltd, “Raspberry Pi,” Raspberry Pi. [Online]. Available: https://www.raspberrypi.com/

[102] Measurement Computing Corporation, “Thermocouple Measurement HAT for Raspberry Pi® from Measurement Computing,” MC Measurement Computing - MCC 134. [Online]. Available: https://www.mccdaq.com/DAQ-HAT/MCC-134.aspx

[103] “Welcome to Python.org,” Python.org. Accessed: Oct. 09, 2022. [Online]. Available: https://www.python.org/

[104] L. S. M. Castellanos, G. E. C. Caballero, V. R. M. Cobas, E. E. S. Lora, and A. M. M. Reyes, “Mathematical modeling of the geometrical sizing and thermal performance of a Dish/Stirling system for power generation,” *Renew. Energy*, vol. 107, pp. 23–35, Jul. 2017, doi: 10.1016/j.renene.2017.01.020.

[105] R. E. Hogan, “AEETES - A solar reflux receiver thermal performance numerical model,” *Sol. Energy*, vol. 52, no. 2, pp. 167–178, 1994, doi: doi:10.1016/0038-092x(94)90066-3.

[106] Anvils South Africa, “Technical Data Sheet - Ceramic Fibre Blanket.” Anvils South Africa, 2022. [Online]. Available: https://www.anvils.co.za/product/ceramic-fibre-blanket-insulation/

[107] S.-Y. Wu, F.-H. Guo, and L. Xiao, “Numerical investigation on combined natural convection and radiation heat losses in one side open cylindrical cavity with constant heat flux,” *Int. J. Heat Mass Transf.*, vol. 71, pp. 573–584, Apr. 2014, doi: 10.1016/j.ijheatmasstransfer.2013.12.064.

[108] M. J. Brooks *et al.*, “SAURAN: A new resource for solar radiometric data in Southern Africa,” *J. Energy South. Afr.*, vol. 26, no. 1, 2015, doi: 10.17159/2413-3051/2015/v26i1a2208.

[109] J. S. Armstrong and F. Collopy, “Error measures for generalizing about forecasting methods: Empirical comparisons,” *Int. J. Forecast.*, vol. 08, pp. 69–80, 1992.

[110] J. Schifo and J. Radia, “Theoretical/best practice energy use in metalcasting operations,” Advanced Technology Institute North Charleston, Washington, May 2004. doi: 10.2172/1216246.

[111] “Climate Transparency Report 2022 - South Africa,” Climate Transparency.org, Oct. 2022. [Online]. Available: https://www.climate-transparency.org/wp-content/uploads/2022/10/CT2022-South-Africa-Web.pdf

[112] “Mini-Melt® Furnaces | Small Capacity Induction Furnace,” Inductotherm Corp. [Online]. Available: https://www.inductotherm.com/products/mini-melt-furnaces/

[113] WorldData.info, “Sunrise and sunset in South Africa,” Worlddata.info. Accessed: Sep. 08, 2023. [Online]. Available: https://www.worlddata.info/africa/south-africa/sunset.php

APPENDIX A : EXPERIMENTAL PROCEDURE

The typical experimental procedure, as described in a step-by-step approach, is shown below:

1. Charge zinc feedstock into the zinc cavity, with thermocouples already secured in place.
2. Apply high-temperature sealant on the back flange and secure the blanking flange in place using twelve bolts. Also, fit two layers of insulating ceramic fibre blanket to the back blanking flange.
3. Fit the Raspberry Pi unit and battery back to the back of the receiver, on top of the two layers of insulation. The assembly is secured in place by having four of the flange bolts extend through the fibre blanket. Once secured in place, the thermocouples are connected to the Raspberry Pi, and all the cabling is secured to the receiver by high-temperature glass tape.
4. The Raspberry Pi is powered on, and a connection check between the device and the monitoring laptop is done to verify that temperature readings can be observed remotely.
5. The cable winch attached to the base of the solar dish is used to lower the receiver frame to ground level for easy access.
6. The receiver is then fitted to the receiver frame and secured in place by tightening the drive shaft in place.
7. The cable winch is used again to raise the assembly into place, and the linear actuator is connected to the assembly for solar tracking purposes.
8. The dish is then pointed towards the sun and aligned in both axes using the shadows cast by the structure as a reference. A vacuum is then drawn behind each reflective membrane to concentrate the incoming solar radiation into the cavity of the receiver.
9. The drive system is activated, and the cavity is rotated at approximately 30 revolutions per minute (RPM) – this signals the start of a test. Every minute the dish tracking is adjusted in both the elevation and azimuth axes using the pinhole tracker as a reference. At the same time, the temperature increase in the receiver is noted.

10. The temperature will steadily increase to 420ºC, the melting point of zinc, after which it will level out as the material undergoes the phase change. Once the temperature starts to rise again, it serves as an indication that the phase change is complete and that the entire batch of zinc has melted down.
11. The solar dish is swivelled out of alignment with the sun, and the cable winch is used again to lower the receiver to ground level. Once at ground level, the steel plug at the back of the receiver is opened, and the molten zinc is allowed to drain out of the receiver into a steel ladle.
12. Once all the zinc is drained from the receiver, the receiver is removed from the receiver frame and is allowed to cool down. The solar dish is then returned to its stow position to be used again later, and the vacuum behind the reflective membranes is released.
13. The Raspberry Pi and battery pack are removed from the receiver, and the data can now be retrieved from the device for analysis. The cast ingot is also removed from the steel ladle to be weighed and used for the mass balance.

APPENDIX B : THERMODYNAMIC MODEL – PYTHON CODE

B.1 Description

The code is started by defining functions to calculate the material and thermal properties of atmospheric air and zinc metal for any given temperature and atmospheric pressure. These functions are called up throughout the heat loss calculations.

Next, the design parameters for the parabolic dish and receiver are defined together with variables for the zinc batch size and the cut-off temperature. The cut-off temperature is used to define when a batch of zinc is assumed to be fully molten. This cut-off temperature can be any temperature, but as a first approximation, it is set to 20 °C above the melting temperature of zinc (420 °C), which should allow for some additional heating to aid in the tapping process. From there, the heat input is defined together with the three different heat loss mechanisms, as discussed in detail above, and these are used to calculate the total heat loss from the cavity receiver.

A section of code is then used to read the weather data stored in an Excel document and to present it in a useful format. The last step is to use the weather data as input variables for calculating the heat loss or heat gain for that given time step. Given that the temperature of the zinc body is assumed to be uniform and that zinc has a relatively high thermal conductivity, the zinc temperature is a function of time and treated as a lumped system. This process is iterated for the full duration of the weather data file. From this, the number of molten zinc batches produced for the given weather conditions are calculated. Together with actual weather conditions, 30-minute batch refill times are assumed. This is incorporated to simulate daily operations during which the receiver will have to be drained of molten zinc and refilled with a new batch. Under real-world conditions, this draining or tapping step will be done as described in the experimental method by tilting the receiver, which is ideal for casting applications. This batch-refill time will have to be adjusted to meet actual operations and will be determined by the time requirement based on the application to which it is applied. The data generated by this model can then be represented in useful graph format to evaluate the different heat loss mechanisms and investigate which environmental and

design variables have the largest impact on each. This can, in turn, be used to optimise the solar concentrator and receiver system for that specific site and its actual weather conditions.

B.2 General information

Author: PJA Bezuidenhout

Code purpose: A predictive analytical model was developed in the Python coding language to calculate the temperature of a zinc inventory in a dual cavity solar receiver using historical weather data as input. The code can be used to predict the throughput of a solar melting application for feasibility studies or for evaluating design considerations.

Latest revision: Revision 8

Date of latest revision: 25 November 2023

Creation date (Rev 0): August 2021

IDE used for development: Coding was done in Jupyter Notebook. Jupyter Notebook is an interactive, web-based environment that can be used as an integrated development environment (IDE) for the Python coding language. It allows the code to be executed in block form, providing instant feedback. This platform was selected given the limited coding experience with which the project was started, and Jupyter Notebook allowed for easier troubleshooting during the coding process. The code was executed in block form using various cells in Jupyter Notebook. Each heading describes a block of code.

IDE download link: https://jupyter.org/install

General comments:

- # is used for comments and to indicate code headings.
- All code is provided with actual indentation and syntax to allow code to be directly copied to a new Jupyter Notebook document. This should allow the code to execute without additional troubleshooting.

B.3 Import libraries

```
# Import Libraries

%matplotlib inline

import numpy

from matplotlib import pyplot

from scipy import constants # Note: For very large packages like SciPy, it's preferred to import only the pieces you need.

import pandas

from datetime import datetime

import csv
```

B.4 Define the thermophysical properties of air

```
## Thermophysical properties of air at Atmospheric pressure

def air_Cp(T, P):

    # This function calculates the heat capacity of dry air at a given temperature and pressure (in J/kg.K)

    return (1.053 - 0.0004*T + 8e-7*T**2 - 3e-10*T**3) *1000


def air_rho(T, P):

    # Density of air (in kg/m^3)

    return 4.4275 - 0.0156*T + 2e-5*T**2 - 8e-9*T**3


def air_k(T, P):

    # Thermal conductivity of air (in W/m.K)

    return (-1.2499 + 0.1085*T - 6e-5*T**2 + 2e-8*T**3) * 0.001


def air_mu(T, P):

    # Dynamic Viscosity of air (in kg/m.s)

    return (7.1327 + 0.6987*T - 0.0004*T**2 + 1e-7*T**3) * 1e-7


def air_beta(T, P):

    # Volumetric expansion coefficient of air (in 1/K)

    return 0.00132
```

```
def air_nu(T, P):
    # Kinematic Viscosity of air (in m^2/s)
    return air_mu(T, P) / air_rho(T, P)

def air_alpha(T, P):
    # Thermal diffusivity of air (in m^2/s)
    return air_k(T, P) / (air_rho(T, P) * air_Cp(T, P))

def air_Pr(T, P):
    # Prandtl number of air (-)
    return (air_mu(T, P) * air_Cp(T, P)) / air_k(T, P)
```

B.5 Define the thermophysical properties of zinc and steel

```
## Thermophysical properties of Steel

def steel_emmissivity (T):
    # Emmissivity of steel
    if T < 380 + 273:
        steel_em = 0.28
    elif (380 + 273) <= T < (520 +273):
        steel_em = 0.00293*(T-273) - 0.833  # Eq is for temp in C
    else:
        steel_em = 0.69
    return (steel_em)

def steel_solid_Cp():
    # Specific heat capacity of steel (J/kg.K)
    return 510.8

## Thermophysical properties of Zn
def zinc_solid_Cp(T):
```

```
    #This function calculates the heat capacity of solid Zinc at a given temperature (in
J/kg.K).
    return 249.28 + 0.6121*T - 0.0005*T**2


def zinc_liquid_Cp(T):
    # Heat capacity of molten zinc (in J/kg.K)
    # Gronvold and Stolen_2002_Heat capacity of Zn
    return 0.0004*T**2 - 0.7332*T + 823.01


def zinc_solid_rho(T):
    # Density of solid zinc (in kg/m3)
    return 6559 - 0.8849*(T -692.677)


def zinc_liquid_rho(T):
    # Density of molten zinc (in kg/m3)
    return zinc_solid_rho(T)


def zinc_solid_k(T):
    # Thermal conductivity of solid zinc (in W/mK)
    return 120.25 + 0.0069*T - 0.0001*T**2 + 8e-8*T**3


def zinc_liquid_k(T):
    # Thermal conductivity of molten zinc (in W/mK)
    return 9.3 + 0.058*T


def zinc_lambda():
    # Heat of fusion of zinc (in J/kg)
    return 112403


def zinc_Tmpt():
    # Melting point of zinc (in K)
    return 692.65
```

B.6 Define design parameters

```
# Design parameters

# Concentrator/ Dish parameters

mydish = {'Dish_diameter' : 1.6, # Dish diameter (m)

        'Dish_aperture_area' : 2.84, # Dish aperture area (m^2)

        'Dish_depth' : 0.145, # Dish depth (m)

        'Focal_length' : 1.098, # focal length (m)

        'Rim_angle' : 40, # rim angle (°), phi

        'Itercept_factor' : 1, # intercept factor, Gamma

        'Reflectivity' : 0.9, # reflectivity, rho_R

        'Shading_factor' : 1 # shading factor, f_s

       }


# Receiver properties

myreceiver = {'Cavity_absorptivity' : 0.52, # Absorptivity

            'Receiver_aperture_diameter' : 0.2, # Receiver aperture diameter (m)

            'A_ratio' : 0.0035, # Specified by le Roux et al._2014

            'Receiver_lip' : 0.0001, # Lip dimension (m)

            'Cavity_depth' : 0.2, # depth of cone (m)

            'Insulation_k' : 0.11, # Thermal conductivity of insulation blanket @ 1073 K
(W/m.K)

            'Insulation_thickness' : 0.05, # Insulation thickness (m)

            'Steel_receiver_weight' : 6.7, # Receiver shell weight (kg)

           }


# Batch properties

mybatch = {'m_Zn': 10, # Batch mass of zinc (kg)

         'Tmax': 750, # Cut-off zinc temperature at which batch is stopped (K)

         'hold_time': 1800 # Tapping and charging downtime in between batches (s) =
30 min

        }
```

B.7 Thermodynamic model set-up

```
# Thermodynamic model

# Solar input

def Q_in(mydish, DNI):

    # Input power supplied from the concentrator [in W]

    return
DNI*mydish['Dish_aperture_area']*mydish['Itercept_factor']*mydish['Shading_factor']*
mydish['Reflectivity']
```

B.8 Conduction heat losses

```
## Conduction losses

# Conduction heat losses from cavity (W)

def Q_cond(myreceiver, Tinf, T, windspeed):


    # Dimensions of cylindrical cavity

    Receiver_aperture_radius = myreceiver['Receiver_aperture_diameter']/2

    Receiver_aperture_area = constants.pi * (Receiver_aperture_radius**2) # Area or
receiver aperture

    Receiver_cavity_radius = Receiver_aperture_radius + myreceiver['Receiver_lip'] #
Radius of receiver cavity

    Receiver_cavity_diameter = Receiver_cavity_radius * 2

    Cavity_internal_area = ((2 * constants.pi * (Receiver_cavity_radius) *
myreceiver['Cavity_depth']) +

    (2 * constants.pi * (Receiver_cavity_radius**2))) # Surface area of entire
cylindrical cavity

    Cavity_internal_area_act = Cavity_internal_area - Receiver_aperture_area #
Subtract aperture from cavity surface area

    Cavity_volume = constants.pi * (Receiver_cavity_radius**2) *
myreceiver['Cavity_depth'] # Volume of cylindrical cavity


    # Dimensions for cylindrical container

    Cylindrical_container_diameter = (2 * Receiver_cavity_radius) + 0.06 + 0.006 # 30
mm gap all way round + 2x3 mm steel thickness

    Cylindrical_container_radius = Cylindrical_container_diameter/2

    Cylindrical_container_lenght = myreceiver['Cavity_depth'] + 0.03 # 30 mm gap at
back of cavity
```

```
    Cylindrical_container_area = ((2 * constants.pi * Cylindrical_container_radius *
Cylindrical_container_lenght) + (2 * constants.pi * (Cylindrical_container_radius**2)))

    Cylindrical_container_volume = constants.pi * (Cylindrical_container_radius**2) *
Cylindrical_container_lenght

    Zn_volume = Cylindrical_container_volume - Cavity_volume

    Insulation_outer_diameter = Cylindrical_container_diameter +
(2*myreceiver['Insulation_thickness']) # Add insulation thickness for either side

    Insulation_outer_radius = Insulation_outer_diameter/2

    Insulation_inner_radius = Cylindrical_container_diameter/2

    A_faceplate = (((constants.pi * (Cylindrical_container_radius**2)-(constants.pi *
(Receiver_aperture_radius**2))))) # Surface area of faceplate


    T_insulation_surface = 350 # Guess insulation surface value

    T_Zn = T # Set calculated Zn temperature equal to T_Zn for insulation inner
temperature


    while True: # While loop to calculate surface temperature

        # Reynolds number at insulation surface with atmospheric pressure as 1

        Re_D = (air_rho(T_insulation_surface,1) * windspeed *
Insulation_outer_diameter) / air_mu(T_insulation_surface,1)


        # Calculating constants for Nu_D_forc for different Re numbers

        if 0.4 < Re_D <= 4:

            C, m = 0.989, 0.330

        elif 4 < Re_D <= 40:

            C, m = 0.911, 0.385

        elif 40 < Re_D <= 4000:

            C, m = 0.683, 0.466

        elif 4000 < Re_D <= 40000:

            C, m = 0.193, 0.618

        elif 40000 < Re_D < 400000:

            C, m = 0.027, 0.805

        else:

            C, m = 0.01, 1
```

```
        # Nusselt number for forced convection over insulation
        Nu_D_forc = C * (Re_D**m) * (air_Pr(T_insulation_surface,1)**(1/3))

        # Granshof number
        Gr_L = ((constants.g * air_beta(T_insulation_surface,1) * (T_insulation_surface
- Tinf) * Cylindrical_container_lenght**3)) / ((air_nu(T_insulation_surface,1)**2))

        # Rayleigh number
        Ra_D = Gr_L * air_Pr(T_insulation_surface,1)

        # Nusselt number for natural convection at insulation
        Nu_D_nat = (0.6 + ((0.387 * Ra_D**(1/6))/((1 +
((0.559/air_Pr(T_insulation_surface,1))**(9/16)))**(8/27))))**2

        # Calculate combined Nusselt number
        Test = Gr_L/Re_D**2
        if Test < 0.1:
            Nu_D = Nu_D_forc
        elif 0.1 <= Test <= 10:
            Nu_D = (Nu_D_forc**4 + Nu_D_nat**4)**(1/4)
        elif Test > 10:
            Nu_D = Nu_D_nat
        else:
            raise ValueError('Nu_D is out of range!')

        # Convection heat coefficient at insulation surface [W/m^2.K]
        h_o = (Nu_D * air_k(T_insulation_surface,1))/Insulation_outer_diameter

        # Insulation resistance
        R_ins = ((numpy.log(Insulation_outer_radius/Insulation_inner_radius))/
                (2* constants.pi * Cylindrical_container_lenght *
myreceiver['Insulation_k']))
```

```
    # Convection resistance
    R_conv = 1/(2 * constants.pi * Cylindrical_container_lenght *
Insulation_outer_radius * h_o)

    # Sum of conduction resistances
    R_tot = R_ins + R_conv

    Q_cond_1 = (T_Zn - Tinf)/R_tot # Assume insulation inside temperature is
same as Zn temperature

    T_surf = ((Q_cond_1)/(1/(R_conv)))+ Tinf # Calculate surface temperature
using calculated thermal resistances

    # If statement to iteratively calculate correct surface temperature
    if abs(T_insulation_surface - T_surf) > 0.1:
        T_corrected_surface_temperature = abs(T_insulation_surface + T_surf)/2
        T_insulation_surface = T_corrected_surface_temperature
    else:
        break   # If small enough difference between guess and actual, break loop

  return ((T_Zn - Tinf)/R_tot)
```

B.9 Convection heat losses – Experiments 1 & 2 (with no faceplate insulation)

```
## Convection losses – Experiment 1 & 2
 # Convection heat losses from cavity (W)
def Q_conv(myreceiver, Tinf, Tcav, windspeed, tilt, yaw):

  # Dimensions of cylindrical cavity
  Receiver_aperture_radius = myreceiver['Receiver_aperture_diameter']/2
  Receiver_aperture_area = constants.pi * (Receiver_aperture_radius**2) # Area or
receiver aperture
  Receiver_cavity_radius = Receiver_aperture_radius + myreceiver['Receiver_lip'] #
Radius of receiver cavity
```

```
    Receiver_cavity_diameter = Receiver_cavity_radius*2

    Cavity_internal_area = ((2 * constants.pi * (Receiver_cavity_radius) *
myreceiver['Cavity_depth']) +

    (2 * constants.pi * (Receiver_cavity_radius**2))) # Surface area of entire
cylindrical cavity

    Cavity_internal_area_act = Cavity_internal_area - Receiver_aperture_area #
Subtract aperture from cavity surface area

    Cavity_volume = constants.pi * (Receiver_cavity_radius**2) *
myreceiver['Cavity_depth'] # Volume of cylindrical cavity

    Cylindrical_container_diameter = (2 * Receiver_cavity_radius) + 0.06 + 0.006 # 30
mm gap all way round + 2x3 mm steel thickness - Receiver OD

    Cylindrical_container_radius = Cylindrical_container_diameter/2

    A_faceplate = (((constants.pi * (Cylindrical_container_radius**2)-(constants.pi *
(Receiver_aperture_radius**2))))) # Surface area of faceplate

    C_faceplate = 2 * constants.pi * Cylindrical_container_radius # Circumferenace of
faceplate


    # Air properties calculated at mean temperature between wall and ambient
Reddy_2016

    T_conv = (Tcav + Tinf)/2

    T_prop = (11/16)*Tcav + (3/16)*Tinf #Stine and McDonald


    # Granshof number  # Using aperture diameter as characteristic length

    Gr_conv = ((constants.g * air_beta(T_conv,1) * (Tcav - Tinf) *
myreceiver['Receiver_aperture_diameter']**3)/(air_nu(T_conv,1)**2))


    # Granshof number  # Using aperture diameter as characteristic length  @ Stine
and McDonald

    Gr_conv_Stine = ((constants.g * air_beta(T_prop,1) * (Tcav - Tinf) *
myreceiver['Receiver_aperture_diameter']**3)/(air_nu(T_prop,1)**2))


    # Reynolds number at insulation surface

    Re_Receiver_aperture_diameter = ((air_rho(T_conv,1) * windspeed *
myreceiver['Receiver_aperture_diameter'])/air_mu(T_conv,1))


    # Reynolds number at insulation surface @ Stine and McDonald
```

```
    Re_Receiver_aperture_diameter_Stine = ((air_rho(T_prop,1) * windspeed *
myreceiver['Receiver_aperture_diameter'])/air_mu(T_prop,1))


    l_c = 1


    if windspeed < 1.5:


        if 0<= tilt <= 45:
            P = (numpy.cos(tilt* numpy.pi/180))**3.2
        else:
            P = 0.707 * (numpy.cos(tilt* numpy.pi/180))**2.2


        Nu_t_nat = 0.78 * P * (l_c**1.75) * (Gr_conv_Stine * air_Pr(T_prop,1))**0.25


        # Calculating constants for Nu_t for different wind directions Reddy_2016
        if -90 < yaw <= -30:
            p, q, r, s, t = 35.112, -0.548, -0.292, 0.18, -0.323
        elif -30 < yaw <= 30:
            p, q, r, s, t = 2.613, -0.545, 2.394, -0.089, -0.324
        elif 30 < yaw <= 90:
            p, q, r, s, t = 87.138, -0.220, -0.394, -0.049, -0.322
        else:
            raise ValueError('yaw is out of range!') # Raise error if value is not in the
range as specified by Reddy


        # Nusselt number for forced convection Reddy_2016
        Nu_t_forc = ((p*(1 + numpy.cos(tilt * numpy.pi/180))**q) * ((3 + numpy.sin(yaw *
numpy.pi/180) +
                numpy.sin(2*yaw * numpy.pi/180) + numpy.sin(3*yaw * numpy.pi/180))**r)
                *
((myreceiver['Receiver_aperture_diameter']/Receiver_cavity_diameter)**s)*
                (((Gr_conv/(Re_Receiver_aperture_diameter)**2))**t))
```

```
        # Internal convection heat transfer coefficient (W/m^2.K)
    h_t_conv = (Nu_t_forc + Nu_t_nat) * air_k(T_conv,1) /
myreceiver['Receiver_aperture_diameter']


  elif 1.5 <= windspeed <= 5:


    #Nusselt number for natural convection Wu_2014
    Nu_t_nat = (0.00106 * (Gr_conv**(0.149))* ((2 + numpy.cos(tilt *
numpy.pi/180))**7.228) *
            ((1 + steel_emmissivity(Tcav))**(-0.0849)) *

((myreceiver['Receiver_aperture_diameter']/Receiver_cavity_diameter)**1.466)) #
Emperical correlation by Wu_2014


    # Calculating constants for Nu_t for different wind directions Reddy_2016
    if -90 < yaw <= -30:
        p, q, r, s, t = 35.112, -0.548, -0.292, 0.18, -0.323
    elif -30 < yaw <= 30:
        p, q, r, s, t = 2.613, -0.545, 2.394, -0.089, -0.324
    elif 30 < yaw <= 90:
        p, q, r, s, t = 87.138, -0.220, -0.394, -0.049, -0.322
    else:
        raise ValueError('yaw is out of range!')


    # Nusselt number for forced convection Reddy_2016
    Nu_t_forc = ((p*(1 + numpy.cos(tilt * numpy.pi/180))**q) * ((3 + numpy.sin(yaw *
numpy.pi/180) +
          numpy.sin(2*yaw * numpy.pi/180) + numpy.sin(3*yaw * numpy.pi/180))**r)
          *
((myreceiver['Receiver_aperture_diameter']/Receiver_cavity_diameter)**s)*
          (((Gr_conv/(Re_Receiver_aperture_diameter)**2))**t))


    # Calculate combined Nusselt number
```

```
        Test_conv = Gr_conv/Re_Receiver_aperture_diameter**2

        if Test_conv < 0.1:
            Nu_t = Nu_t_forc
        elif 0.1 <= Test_conv <= 10:
            Nu_t = (Nu_t_forc**4 + Nu_t_nat**4)**(1/4)
        elif Test_conv > 10:
            Nu_t = Nu_t_nat
        else:
            raise ValueError('Nu_D is out of range!')

        # Internal convection heat transfer coefficient (W/m^2.K)
        h_t_conv = Nu_t * air_k(T_conv,1) / myreceiver['Receiver_aperture_diameter']

    else:
            # Calculating constants for Nu_t for different wind directions Reddy_2016
        if -90 < yaw <= -30:
            p, q, r, s, t = 35.112, -0.548, -0.292, 0.18, -0.323
        elif -30 < yaw <= 30:
            p, q, r, s, t = 2.613, -0.545, 2.394, -0.089, -0.324
        elif 30 < yaw <= 90:
            p, q, r, s, t = 87.138, -0.220, -0.394, -0.049, -0.322
        else:
            raise ValueError('yaw is out of range!')

        # Nusselt number for forced convection Reddy_2016
        Nu_t_forc = ((p*(1 + numpy.cos(tilt * numpy.pi/180))**q) * ((3 + numpy.sin(yaw *
numpy.pi/180) +
                numpy.sin(2*yaw * numpy.pi/180) + numpy.sin(3*yaw * numpy.pi/180))**r)
                *
((myreceiver['Receiver_aperture_diameter']/Receiver_cavity_diameter)**s)*
                (((Gr_conv/(Re_Receiver_aperture_diameter)**2))**t))
```

```
            # Internal convection heat transfer coefficient (W/m^2.K)
        h_t_conv = Nu_t_forc * air_k(T_conv,1) /
myreceiver['Receiver_aperture_diameter']


    #Face plate heat losses
    L_faceplate = A_faceplate/C_faceplate  # Characteristic length of faceplate (Eq
9.29 p609)


    if 0 <= (90 - tilt) < 60: # Calculate buoyancy for air at inclined faceplate - tilt angle
is calculated off the vertical plane
        g_faceplate = constants.g * numpy.cos (90 - tilt)
    else: # angle does not have an influence over 60 degrees
        g_faceplate = constants.g


    Re_L_faceplate = (air_rho(T_conv,1) * windspeed * L_faceplate) /
air_mu(T_conv,1) #Reynolds number at faceplate


    Gr_faceplate = ((g_faceplate * air_beta(T_conv,1) * (Tcav - Tinf) * L_faceplate**3)
/ (air_nu(T_conv,1)**2)) # Grashof number of faceplate
    Pr_faceplate = air_Pr(T_conv,1)


    Ra_faceplate = Gr_faceplate * Pr_faceplate # Rayleigh number at faceplate


    # Angle accounted for in Gr/g_faceplate
    Nu_L_free = 0.52 * Ra_faceplate**(1/5) # Eq 9.32 p 610 (10**4 <Ra< 10**9, Pr >
0.7)


    # Only consider parallel flow - buoyancy not the driving force - only consider
turbulent flow (fibre blanket around cavity causes turbulence)
    # Constant heat flux is assumed - Eq 7.49 p446
    Nu_L_forc = 0.68 * Re_L_faceplate**(1/2) * Pr_faceplate**(1/3)


     # Calculate combined Nusselt number
    Test_faceplate = Gr_faceplate/Re_L_faceplate**2
```

```
    if Test_faceplate < 0.1: # Only forced convection
        Nu_L = Nu_L_forc
    elif 0.1 <= Test_faceplate <= 10: # Combined free and forced convection
        Nu_L = (Nu_L_forc**4 + Nu_L_free**4)**(1/4)
    elif Test_faceplate > 10: # Only free convection
        Nu_L = Nu_L_free
    else:
        raise ValueError('Nu_faceplate is out of range!')


    h_faceplate = (Nu_L * air_k(T_conv,1))/L_faceplate # Calculated heat transfer
coefficient for faceplate


    return ((Cavity_internal_area_act * h_t_conv * (Tcav - Tinf))  + (A_faceplate *
h_faceplate * (Tcav - Tinf)))
```

B.10 Convection heat losses – Experiments 3 to 5 (with faceplate insulation)

```
## Convection losses – Experiment 3 - 5
  # Convection heat losses from cavity (W)
def Q_conv(myreceiver, Tinf, Tcav, windspeed, tilt, yaw):


    # Dimensions of cylindrical cavity
    Receiver_aperture_radius = myreceiver['Receiver_aperture_diameter']/2
    Receiver_aperture_area = constants.pi * (Receiver_aperture_radius**2) # Area or
receiver aperture
    Receiver_cavity_radius = Receiver_aperture_radius + myreceiver['Receiver_lip'] #
Radius of receiver cavity
    Receiver_cavity_diameter = Receiver_cavity_radius*2
    Cavity_internal_area = ((2 * constants.pi * (Receiver_cavity_radius) *
myreceiver['Cavity_depth']) +
    (2 * constants.pi * (Receiver_cavity_radius**2))) # Surface area of entire
cylindrical cavity
    Cavity_internal_area_act = Cavity_internal_area - Receiver_aperture_area #
Subtract aperture from cavity surface area
```

```
    Cavity_volume = constants.pi * (Receiver_cavity_radius**2) *
myreceiver['Cavity_depth'] # Volume of cylindrical cavity


    # Air properties calculated at mean temperature between wall and ambient
Reddy_2016

    T_conv = (Tcav + Tinf)/2

    T_prop = (11/16)*Tcav + (3/16)*Tinf #Stine and McDonald


        # Granshof number  # Using aperture diameter as characteristic length

    Gr_conv = ((constants.g * air_beta(T_conv,1) * (Tcav - Tinf) *
myreceiver['Receiver_aperture_diameter']**3)/(air_nu(T_conv,1)**2))


        # Granshof number  # Using aperture diameter as characteristic length  @ Stine
and McDonald

    Gr_conv_Stine = ((constants.g * air_beta(T_prop,1) * (Tcav - Tinf) *
myreceiver['Receiver_aperture_diameter']**3)/(air_nu(T_prop,1)**2))


    # Reynolds number at insulation surface

    Re_Receiver_aperture_diameter = ((air_rho(T_conv,1) * windspeed *
myreceiver['Receiver_aperture_diameter'])/air_mu(T_conv,1))


    # Reynolds number at insulation surface @ Stine and McDonald

    Re_Receiver_aperture_diameter_Stine = ((air_rho(T_prop,1) * windspeed *
myreceiver['Receiver_aperture_diameter'])/air_mu(T_prop,1))


    l_c = 1


    if windspeed < 1.5:


        if 0<= tilt <= 45:

            P = (numpy.cos(tilt* numpy.pi/180))**3.2

        else:

            P = 0.707 * (numpy.cos(tilt* numpy.pi/180))**2.2
```

```
        Nu_t_nat = 0.78 * P * (l_c**1.75) * (Gr_conv_Stine * air_Pr(T_prop,1))**0.25

        # Calculating constants for Nu_t for different wind directions Reddy_2016
        if -90 < yaw <= -30:
            p, q, r, s, t = 35.112, -0.548, -0.292, 0.18, -0.323
        elif -30 < yaw <= 30:
            p, q, r, s, t = 2.613, -0.545, 2.394, -0.089, -0.324
        elif 30 < yaw <= 90:
            p, q, r, s, t = 87.138, -0.220, -0.394, -0.049, -0.322
        else:
            raise ValueError('yaw is out of range!')

        # Nusselt number for forced convection Reddy_2016
        Nu_t_forc = ((p*(1 + numpy.cos(tilt * numpy.pi/180))**q) * ((3 + numpy.sin(yaw *
numpy.pi/180) +
                numpy.sin(2*yaw * numpy.pi/180) + numpy.sin(3*yaw * numpy.pi/180))**r)
                *
((myreceiver['Receiver_aperture_diameter']/Receiver_cavity_diameter)**s)*
                (((Gr_conv/(Re_Receiver_aperture_diameter)**2))**t))

            # Internal convection heat transfer coefficient (W/m^2.K)
        h_t_conv = (Nu_t_forc + Nu_t_nat) * air_k(T_conv,1) /
myreceiver['Receiver_aperture_diameter']

    elif 1.5 <= windspeed <= 5:
        #Nusselt number for natural convection Wu_2014
        Nu_t_nat = (0.00106 * (Gr_conv**(0.149))* ((2 + numpy.cos(tilt *
numpy.pi/180))**7.228) *
                ((1 + steel_emmissivity(Tcav))**(-0.0849)) *

((myreceiver['Receiver_aperture_diameter']/Receiver_cavity_diameter)**1.466)) #
Emperical correlation by Wu_2014

        # Calculating constants for Nu_t for different wind directions Reddy_2016
```

```
        if -90 < yaw <= -30:
            p, q, r, s, t = 35.112, -0.548, -0.292, 0.18, -0.323
        elif -30 < yaw <= 30:
            p, q, r, s, t = 2.613, -0.545, 2.394, -0.089, -0.324
        elif 30 < yaw <= 90:
            p, q, r, s, t = 87.138, -0.220, -0.394, -0.049, -0.322
        else:
            raise ValueError('yaw is out of range!')

        # Nusselt number for forced convection Reddy_2016
        Nu_t_forc = ((p*(1 + numpy.cos(tilt * numpy.pi/180))**q) * ((3 + numpy.sin(yaw *
numpy.pi/180) +
                numpy.sin(2*yaw * numpy.pi/180) + numpy.sin(3*yaw * numpy.pi/180))**r)
                *
((myreceiver['Receiver_aperture_diameter']/Receiver_cavity_diameter)**s)*
                (((Gr_conv/(Re_Receiver_aperture_diameter)**2))**t))

        # Calculate combined Nusselt number
        Test_conv = Gr_conv/Re_Receiver_aperture_diameter**2

        if Test_conv < 0.1:
            Nu_t = Nu_t_forc
        elif 0.1 <= Test_conv <= 10:
            Nu_t = (Nu_t_forc**4 + Nu_t_nat**4)**(1/4)
        elif Test_conv > 10:
            Nu_t = Nu_t_nat
        else:
            raise ValueError('Nu_D is out of range!')

        # Internal convection heat transfer coefficient (W/m^2.K)
        h_t_conv = Nu_t * air_k(T_conv,1) / myreceiver['Receiver_aperture_diameter']
    else:
```

```
    if 0 <= (90 - tilt) < 60: # Calculate buoyancy for air at inclined faceplate - tilt angle is calculated off the vertical plane
        g_cavity = constants.g * numpy.cos (90 - tilt)
    else: # angle does not have an influence over 60 degrees
        g_cavity = constants.g


    Pr_cavity = air_Pr(Tcav,1)


    Ra_cavity = Gr_conv * Pr_cavity # Rayleigh number


    # Angle accounted for in Gr/g_faceplate
    Nu_L_free = 0.52 * Ra_cavity**(1/5) # Eq 9.32 p 610 (10**4 <Ra< 10**9, Pr > 0.7)


    # Only consider parallel flow - buoyancy not the driving force - only consider turbulent flow (fibre blanket around cavity cause turbulence)
    # Constant heat flux is assumed - Eq 7.49 p446
    Nu_L_forc = 0.68 * Re_Receiver_aperture_diameter**(1/2) * Pr_cavity**(1/3)



     # Calculate combined Nusselt number
    Test_plate = Gr_conv/Re_Receiver_aperture_diameter**2


    if Test_plate < 0.1: # Only forced convection
        Nu_L = Nu_L_forc
    elif 0.1 <= Test_plate <= 10: # Combined free and forced convection
        Nu_L = (Nu_L_forc**4 + Nu_L_free**4)**(1/4)
    elif Test_plate > 10: # Only free convection
        Nu_L = Nu_L_free
    else:
        raise ValueError('Nu_faceplate is out of range!')


    h_t_conv = (Nu_L * air_k(T_conv,1))/Receiver_cavity_diameter
```

```
    return (Cavity_internal_area_act * h_t_conv * (Tcav - Tinf))
```

B.11 Radiation heat losses – Experiments 1 & 2 (with no faceplate insulation)

```
## Radiation losses Experiment 1 & 2

# Radiation heat losses from cavity (W)

def Q_rad(myreceiver, DNI, Tcav, Tinf):


    # Dimensions of cylindrical cavity

    Receiver_aperture_radius = myreceiver['Receiver_aperture_diameter']/2

    Receiver_aperture_area = constants.pi * (Receiver_aperture_radius**2) # Area or
receiver aperture

    Receiver_cavity_radius = Receiver_aperture_radius + myreceiver['Receiver_lip'] #
Radius of receiver cavity

    Receiver_cavity_diameter = Receiver_cavity_radius * 2

    Cavity_internal_area = ((2 * constants.pi * (Receiver_cavity_radius) *
myreceiver['Cavity_depth'])

    + (2 * constants.pi * (Receiver_cavity_radius**2))) # Surface area of entire
cylindrical cavity

    Cavity_internal_area_act = Cavity_internal_area - Receiver_aperture_area #
Subtract aperture from cavity surface area

    Cavity_volume = constants.pi * (Receiver_cavity_radius**2) *
myreceiver['Cavity_depth'] # Volume of cylindrical cavity

    Cylindrical_container_diameter = (2 * Receiver_cavity_radius) + 0.06 + 0.006 # 30
mm gap all way round + 2x3 mm steel thickness - Receiver OD

    Cylindrical_container_radius = Cylindrical_container_diameter/2

    A_faceplate = (((constants.pi * (Cylindrical_container_radius**2)-(constants.pi *
(Receiver_aperture_radius**2)))))


    # Effective emissivity

    Epsi_eff = (steel_emmissivity(Tcav) / (1 - (1 - steel_emmissivity(Tcav))

*(1 - (Receiver_aperture_area/Cavity_internal_area_act))))

    # Effective absorptance

    alpha_eff = (myreceiver['Cavity_absorptivity'] / (1 - (1 -
myreceiver['Cavity_absorptivity'])

 *(1 - (Receiver_aperture_area/Cavity_internal_area_act))))
```

```
    # Radiation losses due to emission [W]

    Q_rad_em = Epsi_eff * constants.sigma * Receiver_aperture_area * (Tcav**4 -
Tinf**4)


    Q_rad_em_surface = steel_emmissivity(Tcav) * constants.sigma * A_faceplate *
(Tcav**4 - Tinf**4) #Calculate emissivity from receiver faceplate

    # Radiation losses due to reflectivity [W]

    Q_rad_ref = (1-alpha_eff) * Q_in(mydish, DNI)


    return (Q_rad_em + Q_rad_ref + Q_rad_em_surface)
```

B.12 Radiation heat losses – Experiments 3 to 5 (with faceplate insulation)

```
## Radiation losses Experiment 3-5

# Radiation heat losses from cavity (W)

def Q_rad(myreceiver, DNI, Tcav, Tinf):


    # Dimensions of cylindrical cavity

    Receiver_aperture_radius = myreceiver['Receiver_aperture_diameter']/2

    Receiver_aperture_area = constants.pi * (Receiver_aperture_radius**2) # Area or
receiver aperture

    Receiver_cavity_radius = Receiver_aperture_radius + myreceiver['Receiver_lip'] #
Radius of receiver cavity

    Receiver_cavity_diameter = Receiver_cavity_radius * 2

    Cavity_internal_area = ((2 * constants.pi * (Receiver_cavity_radius) *
myreceiver['Cavity_depth'])

    + (2 * constants.pi * (Receiver_cavity_radius**2))) # Surface area of entire
cylindrical cavity

    Cavity_internal_area_act = Cavity_internal_area - Receiver_aperture_area #
Subtract aperture from cavity surface area

    Cavity_volume = constants.pi * (Receiver_cavity_radius**2) *
myreceiver['Cavity_depth'] # Volume of cylindrical cavity


    # Effective emissivity

    Epsi_eff = (steel_emmissivity(Tcav) / (1 - (1 - steel_emmissivity(Tcav))

*(1 - (Receiver_aperture_area/Cavity_internal_area_act))))
```

```
    # Effective absorptance
    alpha_eff = (myreceiver['Cavity_absorptivity'] / (1 - (1 -
myreceiver['Cavity_absorptivity'])
*(1 - (Receiver_aperture_area/Cavity_internal_area_act))))
    # Radiation losses due to emission [W]
    Q_rad_em = Epsi_eff * constants.sigma * Receiver_aperture_area * (Tcav**4 -
Tinf**4)
    # Radiation losses due to reflectivity [W]
    Q_rad_ref = (1-alpha_eff) * Q_in(mydish, DNI)

    return (Q_rad_em + Q_rad_ref)
```

B.13 Total heat balance calculation

```
## Total heat loss and net energy input
# Heat loss calculation
def Q_loss(myreceiver, DNI, Tinf, T, Tcav, windspeed, tilt, yaw):
    Q_cond_t = Q_cond(myreceiver, Tinf, T, windspeed)
    Q_conv_t = Q_conv(myreceiver, Tinf, Tcav, windspeed, tilt, yaw)
    Q_rad_t = Q_rad(myreceiver, DNI, Tcav, Tinf)

    return (Q_cond_t + Q_conv_t + Q_rad_t)

# Net heat calculation
def Q_net(mydish, myreceiver, DNI, Tinf, T, Tcav, windspeed, tilt, yaw):
    return ((Q_in(mydish, DNI) - Q_loss(myreceiver, DNI, Tinf, T, Tcav, windspeed,
tilt, yaw))*c)
```

B.14 Iterative heat balance calculation

```
# Iterative heatgain calculation
def iterate_heatgain(batchdict, T0, meltmass0, Qnet, dt):
    if T0 >= zinc_Tmpt():
        # We are at or over the melting point of zinc
        if meltmass0 >= batchdict['m_Zn']:
            # Everything is already molten, so liquid heating only
```

```
            T = T0 + Qnet * dt / ((batchdict['m_Zn']+myreceiver['Steel_receiver_weight']) *
((zinc_solid_Cp(T0)+steel_solid_Cp())/2))
            meltmass = meltmass0
        else:
            # The batch is still busy melting
            mm_tmp = meltmass0 + (Qnet * dt) / zinc_lambda() # Original melted + new
melted
            # Transition during timestep - liquid to additional heating
            if mm_tmp > batchdict['m_Zn']:
                # Melting goes to completion inside this time step - some liquid heating
also occurs
                Jmelt = (batchdict['m_Zn'] - meltmass0) * zinc_lambda() # Heat added to
molten material [J]
                Jheat = (Qnet * dt) - Jmelt # Additional heating [J]
                T = T0 + Jheat / (batchdict['m_Zn'] * zinc_liquid_Cp(T0)) # Temperature as
a result of liquid heating
                meltmass = batchdict['m_Zn']
            # No transition - only melting
            else:
                # Only melting happens in this time step
                T = T0
                meltmass = mm_tmp
    else:
        # The solid batch is still warming up
        T_tmp = T0 + (Qnet * dt) /
((batchdict['m_Zn']+myreceiver['Steel_receiver_weight']) *
((zinc_solid_Cp(T0)+steel_solid_Cp())/2))
        # Transition during timestep - solid to liquid
        if T_tmp > zinc_Tmpt():
            # The batch finishes warming up and starts melting inside this time step
            Jheat = batchdict['m_Zn'] * zinc_solid_Cp(T0) * (zinc_Tmpt() - T0)
            Jmelt = Qnet * dt - Jheat
            meltmass = meltmass0 + Jmelt / zinc_lambda()
            T = zinc_Tmpt()
```

```
        # No transition - only solid heating
        else:
            # Solid heating only
            meltmass = meltmass0
            T = T_tmp

    return (T, meltmass)
```

B.15 Import and read Excel weather file

```
# Excel data calculations

## Read data

# Read Excel file into dataframe

df = pandas.read_excel('Weather data_26072022.xlsx') # Specify the data file to read – define data file

# Deleting row 0 and 1 for not containing usefull values # Inplace - write over old df

df.drop([0,1],inplace=True)

df.rename(columns={'Temp_Avg':'T_C', 'Temp_Avg.1':'T_K', 'WS_Avg.1':'WS'},inplace=True) # Replace Temp_Avg duplicates with T_C and T_K


# Reset row to start at 0

df = df.reset_index(drop=True)

df.head()
```

B.16 Run total heat balance calculation with the weather data file as input

```
## Calculation

T_plt, meltmass_plt, DNI_plt, WindS_plt, Cond_plt, Conv_plt, Rad_plt, Total_loss_plt, Qin_plt, Qnet_plt, n_rec_plt = [, , , , , , , , , , ] #Set up Dynamic python list


Tcav = df['T_K'][0] + 1 # Setting initial cavity temp equal to atmospheric temp + 1 C


# Set initial value for heat losses to zero and initiate list -  Starting conditions

Cond_i,Conv_i, Rad_i,Total_loss_i, Qin_i, Qnet_i, n_rec_i = 0, 0, 0, 0, 1, 1, 0

Cond_plt.append(Cond_i)
```

```
Conv_plt.append(Conv_i)
Rad_plt.append(Rad_i)
Total_loss_plt.append(Total_loss_i)
Qin_plt.append(Qin_i)
Qnet_plt.append(Qnet_i)
n_rec_plt.append (n_rec_i)

# Convert time stamps to dateval objects
timestamps = [datetime.strptime(dateval, '%d/%m/%Y %H:%M:%S') for dateval in df['TmStamp']]
# Calculate dt in seconds for every time step in your data
dts = [(ts1-ts0).total_seconds() for ts0, ts1 in zip(timestamps[:-1], timestamps[1:])]
# Convert timestamps to time in hours-since-start, for easier plotting
times = [(tsval - timestamps[0]).total_seconds()/3600 for tsval in timestamps]

# Starting conditions
T, meltmass = df['T_K'][0], 0 # Initial temperature equal to atmospheric temperature and initial mass melt to 0
T_plt.append(T) # Add to list
meltmass_plt.append(meltmass)

DNI = df['DNI_Avg'][0] # Initial DNI value to first DNI from excel
DNI_plt.append(DNI) # Add to list

WindS = df['WS'][0] # Initial WS value to first WS from excel
WindS_plt.append(WindS) # Add to list

holding_yn, heldtime = False, 0

for DNI, Tinf, windspeed, tilt, yaw, dt in zip(df['DNI_Avg'][1:], df['T_K'][1:], df['WS'][1:], df['Calc_Tilt'][1:], df['Yaw'][1:], dts): # Read values from Excel sheet and set it equal to variables
    if holding_yn: # Holding period between batches
```

```
            heldtime += dt # Add timestep
            if heldtime > mybatch['hold_time']:
                # Hold period over, allow next batch to start
                holding_yn, heldtime = False, 0 # Start new loop and set heldtime to zero

        else:
            # Operating period of batch
            Qnet = Q_net(mydish, myreceiver, DNI, Tinf, T, Tcav, windspeed, tilt, yaw)
            T, meltmass = iterate_heatgain(mybatch, T, meltmass, Qnet, dt)

            Cond_i = Q_cond(myreceiver, Tinf, T,windspeed)
            Conv_i = Q_conv(myreceiver, Tinf, Tcav, windspeed, tilt, yaw)
            Rad_i = Q_rad(myreceiver, DNI, Tcav, Tinf)
            Total_loss_i = Q_loss(myreceiver, DNI, Tinf, T, Tcav, windspeed, tilt, yaw)
            Qin_i = Q_in(mydish, DNI)
            Qnet_i = Q_net(mydish, myreceiver, DNI, Tinf, T, Tcav, windspeed, tilt, yaw)
            n_rec_i = (Qnet_i / Qin_i)*100 #Efficiency

            if T > mybatch['Tmax']: # Reach overheating temperature
                # Reset to the next batch and start holding
                T, meltmass, Cond_i,Conv_i, Rad_i, Total_loss_i = Tinf, 0, 0, 0, 0, 0
                holding_yn = True

        Tcav = T  # Set cavity temperature equal to Zn temperature
    #Append all calculated data to the dynamic Python list to be used for the next
    iteration
        T_plt.append(T)
        meltmass_plt.append(meltmass)
        DNI_plt.append(DNI)
        WindS_plt.append(windspeed)

        Cond_plt.append(Cond_i)
```

```
Conv_plt.append(Conv_i)
Rad_plt.append(Rad_i)
Total_loss_plt.append (Total_loss_i)
Qin_plt.append(Qin_i)
Qnet_plt.append(Qnet_i)
n_rec_plt.append(n_rec_i)
```

B.17 Calculate efficiency

```
# Efficiency calculation
total = n_rec_plt # Efficiency list # Pull the efficiency from the dynamic list

Count = len(total) # Count items in list
Sum = sum(total) # Add efficiency list together
print(Sum/Count) # Print average efficiency of Experiment
```

B.18 Plot calculated results

```
## Plots
# Read Excel file containing experimental data into dataframe
Exp1 = pandas.read_excel('Exp 1_26072022.xlsx') # Read experimental data
temperature file.
#Exp1["Time_sec"] = pandas.to_datetime(Exp1["Time_sec"], format =
'%H:%M:%S.%f') # Format date stamp
Exp1data = Exp1[['Time_hours', 'Zinc_1_K',  'Zinc_2_K',  'Zinc_3_K',  'Zinc_back_K',
'Receiver_1_K',  'Receiver_2_K',  'Receiver_3_K',  'Receiver_back_K'  ]]
timeExp1 = Exp1['Time_hours']
Exp1.head()

# Plot Experimental and DNI
fig, ax1 = pyplot.subplots()

ax1.grid()
#Define plot line properties
ax1.plot(timeExp1, Exp1['Receiver_2_K'], 'b--', label = "TC2 (Receiver)", linewidth=2)
#Plot experimental results
ax1.plot(timeExp1, Exp1['Receiver_3_K'], 'y--', label = "TC3 (Receiver)", linewidth=2)
```

```
ax1.plot(timeExp1, Exp1['Receiver_back_K'], 'r--', label = "TC4 (Receiver)", linewidth=2)
ax1.plot(timeExp1, Exp1['Zinc_2_K'], 'b-', label = "TC6 (Zn)", linewidth=2)
ax1.plot(timeExp1, Exp1['Zinc_3_K'], 'y-', label = "TC7 (Zn)", linewidth=2)
ax1.plot(timeExp1, Exp1['Zinc_back_K'], 'r-', label = "TC8 (Zn)", linewidth=2)

#Define plot line properties for second y-axis
# twin object for two different y-axis on the sample plot
ax2=ax1.twinx()
ax2.set_ylabel('DNI [W/$m^{2}$]', fontname="arial", fontsize=12)  # Plot DNI values
ax2.set_ylim(0,1000) #Set second y-axis limits
ax2.plot(times, DNI_plt, 'c-.', label = 'DNI', linewidth=2)

ax1.set_xlim(0,2.25) #Set y-axis limits
ax1.set_ylim(250,800) #Set first y-axis limits
ax1.set_xlabel("Run time [h]", fontname="arial", fontsize=12)
ax1.set_ylabel ("Temperature [K]", fontname="arial", fontsize=12)
#ax1.set_title ("Experimental results_Exp 1", fontname="arial")
ax1.legend(bbox_to_anchor=(1.165, 0.92), fontsize=10, prop={'family': 'Arial'})
ax2.legend(bbox_to_anchor=(1.34, 1), fontsize=10, prop={'family': 'Arial'})

pyplot.show() #Print figure
fig.savefig('Results_Exp1.png', dpi=600,bbox_inches="tight")# Export plot

# Plot Experimental vs Predictive
fig, ax1 = pyplot.subplots()

# Define set of data to be plotted on first axis
ax1.grid()
#Define plot line properties
ax1.plot(times, T_plt, 'k+', label = "Prediction", linewidth=1) # Plot predicted zinc temperature
```

```
ax1.plot(timeExp1, Exp1['Receiver_2_K'], 'b--', label = "TC2 (Receiver)", linewidth=2) #Plot experimental temperatures
ax1.plot(timeExp1, Exp1['Receiver_3_K'], 'y--', label = "TC3 (Receiver)", linewidth=2)
ax1.plot(timeExp1, Exp1['Zinc_2_K'], 'b-', label = "TC6 (Zn)", linewidth=2)
ax1.plot(timeExp1, Exp1['Zinc_3_K'], 'y-', label = "TC7 (Zn)", linewidth=2)

# Define twin object for two different y-axis on the sample plot
ax2=ax1.twinx()
#Define plot line properties for second y-axis
ax2.set_ylabel('Wind Speed [m/s]', fontname="arial", fontsize=12)  # X-lable already defined
ax2.set_ylim(0,15)
ax2.plot(times, WindS_plt, 'g.', label = "Wind speed", linewidth=1) #Plot wind speed
#ax2.axhline(y = 5, color = 'm', linestyle = ':', linewidth=2)

ax1.set_xlim(0,2.25) #Set x-axis limits
ax1.set_ylim(250,800) #Set y-axis limits
ax1.set_xlabel("Run time [h]", fontname="arial", fontsize=12)
ax1.set_ylabel ("Temperature [K]", fontname="arial", fontsize=12)
#Define plot line properties for third y-axis
ax3 = ax1.twinx()
ax3.plot(times, DNI_plt, 'c-.', label = 'DNI', linewidth=2) #Plot DNI
ax3.spines['right'].set_position(('axes', 1.15))
ax3.set_ylabel ('DNI [W/$m^{2}$]', fontname="arial", fontsize=12)
ax3.set_ylim(0,1000)

ax1.legend(bbox_to_anchor=(1.612, 0.86), fontsize=10, prop={'family': 'Arial'})
ax2.legend(bbox_to_anchor=(1.57, 0.93), fontsize=10, prop={'family': 'Arial'})
ax3.legend(bbox_to_anchor=(1.47, 1), fontsize=10, prop={'family': 'Arial'})

pyplot.show() #Print plot
fig.savefig('Prediction and WS_Exp1.png', dpi=600,bbox_inches="tight") # Export figure and set properties
```

```
#Plot Heat losses
fig, ax1 = pyplot.subplots()

ax1.grid()
# Plot calculated heat loss values
ax1.plot(times, Cond_plt, 'm-', label = "Conduction heat loss", linewidth=2 )
ax1.plot(times, Conv_plt, 'g-',  label = "Convection heat loss", linewidth=2 )
ax1.plot(times, Rad_plt, 'y-', label = "Radiation heat loss", linewidth=2 )
ax1.plot(times, Total_loss_plt, 'r-',  label = "Total heat loss", linewidth=2 )
ax1.plot(times, Qin_plt, 'b:',  label = "Total heat input", linewidth=2 )

#Set-up second axis to plot efficiency
ax2=ax1.twinx()
ax2.set_ylabel('Receiver efficiency [%]', fontname="arial", fontsize=12)  # we already handled the x-label with ax[0]
ax2.set_ylim(-100,100) # Define second y-axis limits
ax2.plot(times, n_rec_plt, 'kx', label = "Efficiency", linewidth=1) # Plot efficiency

ax1.set_xlabel("Run time [h]", fontname="arial", fontsize=12)
ax1.set_xlim(0,2.2)
ax1.set_ylim(0,4000)
ax1.set_ylabel ("Heat loss/input [W]", fontname="arial", fontsize=12)
#ax1.set_title (" Heat balance_Exp 1 ", fontname="arial")
#ax1.tight_layout(rect=[0, 0, 1.0, 0.8])
ax1.legend(bbox_to_anchor=(1.152, 0.65), fontsize=10, prop={'family': 'Arial'})
ax2.legend(bbox_to_anchor=(1.4, 0.68), fontsize=10, prop={'family': 'Arial'})

fig.savefig('Heat loss_Exp1.png', dpi=600,bbox_inches="tight") # Export plot
```

APPENDIX C : WEATHER DATA PREPARATION METHOD

In order to make use of the SAURAN historic weather data, this data first needed to be prepared to be used as input in the Python model. Wind directions had to be corrected or grouped to fit the evaluation classifications discussed in the convection heat loss section. To avoid unnecessary run time of the model and to ensure uniformity when comparing results, daily files were cropped to only include data from 07:00 (morning) to 17:00 (afternoon), which corresponds with the shortest day in Pretoria, South Africa [113]. This conservative approach was selected as it ensured that DNI readings would be available, no matter the time of year the weather file was selected from, and it also corresponded with the typical working hours in South Africa. This avoided having to run the model for non-daylight hours and creating unusable data.

The weather file data was evaluated for any non-values or unrealistic values and corrected where necessary. This was done by replacing the unrealistic or corrupted value with the average of the adjacent values, which is seen as a safe assumption given that the data is taken in one-minute intervals.

Because the conduction and convection heat loss model is dependent on the wind speed, a wind speed of 0 m/s can cause undefined errors in the thermodynamic model. Therefore, all wind speeds of 0 m/s were corrected to 0.001 m/s to rectify this calculation issue without a significant impact on the validity of the model.

The azimuth angle of the SOLYS solar tracker at the University of Pretoria is recorded from 0° (North) to 180° and then from -180° to 0°. To be useful for the required wind yaw angle calculation, 360° was added to all negative azimuth angle readings, resulting in a corrected angle range of 0° to 360°.

The next and final weather data adjustment was to calculate the wind yaw direction relative to the receiver aperture orientation. A visual representation of wind direction classification relative to the receiver, as per Reddy et al. [90], is shown in Figure C-1. A side-on wind is classified as any wind relative to the receiver side that falls within 30° to -30°, a back-on wind is grouped under -30° to -90°, and then head-on winds as any wind relative to the receiver within 30° to 90° [90]. A method, as shown in Figure C -2, was employed to calculate the wind direction relative to the receiver side.

Firstly, 90° was subtracted from the azimuth angle to get the relative side-on direction (shown in green). Then, from there, the wind direction (shown in blue) was subtracted to calculate the wind direction relative to the side of the receiver ($x°$). The result was used to classify the wind yaw angle relative to the receiver into the three different groups, as mentioned. This classification can then finally be used, together with the wind speed, to calculate the convection losses from the cavity, as discussed in detail in the Analytical model section. Because symmetry about the receiver's central axis was assumed, the result from the opposite side of the receiver was inversed to achieve the same outcome.

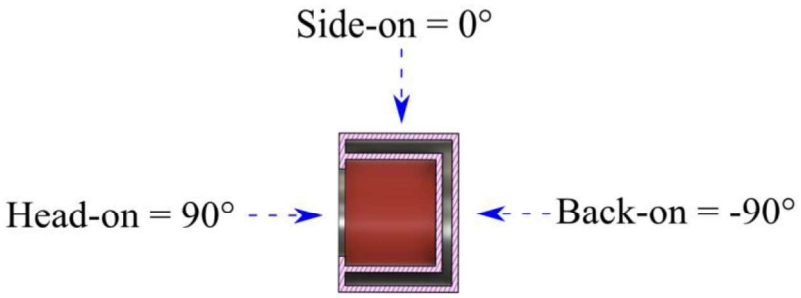

Figure C-1. Wind direction classification relative to receiver orientation (receiver shown in plan view).

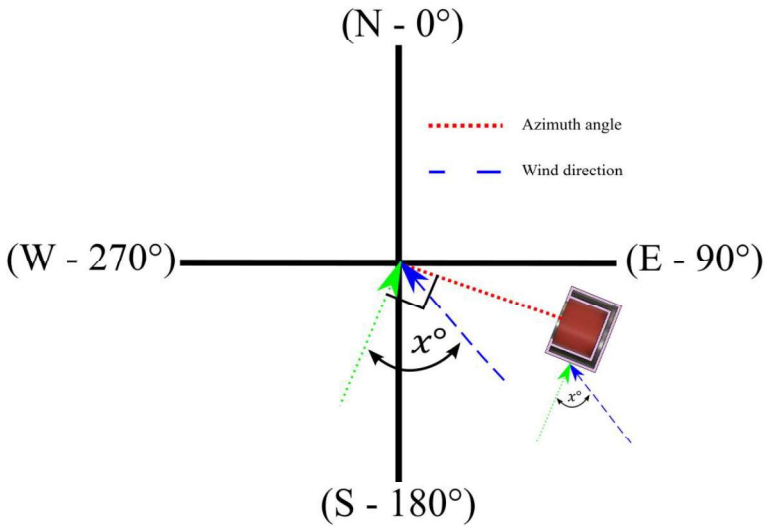

Figure C-2. Wind Yaw angle calculations (receiver shown in plan view).

APPENDIX D : EXPERIMENTAL DATA

Table D-1. Comparison between the different experimental test runs (with minimum and maximum recorded values). Wind speeds of up to 8.39 m/s have been demonstrated for this receiver design. The analytical model will become unstable when the Rayleigh number exceeds 10^{12} (the convection model becomes invalid) which is dependent on both the receiver design and environmental conditions. No limitations on DNI inputs have been found and ambient temperatures below freezing point will require additional validation. Zinc mass and the heat transfer in between particles require further investigation, as the model considers perfect contact between the zinc inventory and receiver sidewall. A heat transfer efficiency constant has been proposed to account for voids but has only been done for as low as 50% volume fill.

		Parameter													
		Zinc mass (m)	**Volume fill**	**Average DNI *(I)***	**Average Temp. (T_∞)**	**Average wind speed (V_{wind})**	**Average receiver tilt angle (θ)**	**Average wind direction relative to the receive aperture (φ)**	**Heat transfer efficiency constant *(c)***	**Average wind direction classification**	**Faceplate insulation**	**Feedstock shape inside cavity**	**Date**	**Time of day**	**Duration**
		kg	***%***	***W/m²***	***°C***	***m/s***	***deg***	***deg***		***(-30° > head on > 30°)*** [90]	***YES/NO***	***Based on the previous experiment***			***Minutes***
Experiment no.	***1***	10	47.62	688.57	18.55	2.01	56.28	50.81	0.5	Side-on-wind	NO	New charge with no previous melt	26/07 /2022	13:37 - 15:25	109
	2	10	47.62	792.61	16.78	2.68	45.41	50.23	0.4	Side-on-wind	NO	Charge from Exp 1.	04/08 /2022	10:12 - 13:00	169
	3	16.96	80.76	909.98	14.2	2.14	44.75	11.51	1	Head-on-wind	YES	Good contact with sidewall due to molten material from Exp 2.	16/08 /2022	09:32 - 12:25	174
	4	14.53	69.19	908.39	12.03	5.26	45.91	61.83	0.8	Side-on-wind	YES	Most of the zinc was drained during Exp 3, so new charge material was added. Some molten material left over from Exp 3 results in better contact between Zn and thermocouples.	21/08 /2022	09:11 - 11:53	163
	5	10	47.62	835.67	23.65	0.95	45.23	-38.68	0.6	Side-on-wind	YES	New receiver and charge with no previous melt.	05/09 /2022	08:36 - 11:30	175
Min		10	47.62	475	9.02	0.001	32.09	-89.63	0.4	-	-	-	-	-	109
Max		16.96	80.76	936	28.34	8.36	60.61	81.54	1	-	-	-	-	-	175